C

Internal Report
DESY F35D-96-18
November 1996

A Measurement of the Total Photon-Proton Cross Section with the ZEUS Detector at HERA

by

C. Sampson

Internal Report
DESY F35D-96-18
November 1996

A Measurement of the Total Photon–Proton Cross Section with the ZEUS Detector at HERA

by

Cortney Sampson

A thesis submitted in conformity with the requirements
for the degree of Doctor of Philosophy
Graduate Department of Physics
University of Toronto

A Measurement of the Total Photon–Proton Cross Section with the ZEUS Detector at HERA

by

Cortney Sampson

A thesis submitted in conformity with the requirements
for the degree of Doctor of Philosophy
Graduate Department of Physics
University of Toronto

Abstract

The measurement of the total photon–proton (γp) cross section ($\sigma^{tot}_{\gamma p}$) by the ZEUS detector using the electron–proton (ep) collisions of the HERA collider is presented. The almost real photons are emitted by the electron beam and are tagged by detecting the scattered electron. The hadronic system of the interaction products is measured in the main ZEUS detector. The effect of background on the measured sample is examined and the background events are statistically removed from the sample. A correction is determined for the inefficiency of triggering on photoproduction events. The γp cross section is measured for three values of the γp centre of mass energy, $W_{\gamma p}$, giving $\sigma^{tot}_{\gamma p} = 181 \pm 4$ (stat.) $^{+12}_{-14}$ (syst.) μb, $\sigma^{tot}_{\gamma p} = 195 \pm 5$ (stat.) $^{+15}_{-17}$ (syst.) μb, and $\sigma^{tot}_{\gamma p} = 199 \pm 6$ (stat.) $^{+17}_{-20}$ (syst.) μb for $W_{\gamma p} = 181$ GeV, 206 GeV, and 229 GeV respectively.

1 Introduction 1

2 Photoproduction at HERA 3
2.1 Electron-proton interaction 3
2.2 Kinematics 4
2.3 Photoproduction 7
2.3.1 Vector meson dominance 8
2.3.1.1 Elastic diffraction 8
2.3.1.2 Diffractive scattering 10
2.3.1.3 Non-diffractive scattering 10
2.3.1.4 VMD summary 11
2.3.2 Parton level processes 11
2.4 Parameterizing the total photoproduction cross section 12
2.4.1 Regge theory parameterizations 13
2.4.2 Minijet parameterizations 13
2.4.3 Schuler & Sjöstrand parameterization 14
2.5 Measuring the total photoproduction cross section 14
2.5.1 Relating ep and γp cross sections 14
2.5.2 Measuring the γp cross section using the EPA 16
2.5.3 Radiative Corrections 16
2.6 Bremsstrahlung 17

3 The experimental setup 19
3.1 The electron-proton collider HERA 19
3.2 The ZEUS detector 22
3.3 The calorimeter 23
3.3.1 Calorimetry 23
3.3.2 Physical description 24
3.4 The central tracking detector 26
3.5 The luminosity monitor 26
3.6 The C5 29
3.7 The vetowall 29
3.8 Central data acquisition 29
3.8.1 First level trigger 31
3.8.2 Second level trigger 31
3.8.3 Event builder 32
3.8.4 Third level trigger 32
3.8.4.1 Hardware 32
3.8.4.2 Control software 35
3.8.4.3 Filter software 36

4 Event Selection and Background Subtraction 39
4.1 Online selection 40
4.1.1 First level trigger 40
4.1.2 Second level trigger 41
4.1.3 Third level trigger 42
4.2 Offline selection 44
4.2.1 Duplicate events 47
4.3 Background subtraction 47
4.3.1 Electron gas background 48
4.3.2 Proton gas background 50
4.3.3 Coincidence background 50
4.4 Run selection 56
4.4.1 Vertex shift cut 56
4.4.2 Run luminosity cut 56
4.4.3 Horizontal beam tilt cut 56
4.4.4 Final data sample 57
4.5 Events per Luminosity 59

5 Calorimeter Acceptance 62
5.1 Event Generation 62
5.1.1 Diffractive processes 62
5.1.2 Non-diffractive processes 63
5.2 Hadronic System 64
5.2.1 Dead material 67
5.2.2 Calorimeter acceptance 68
5.3 M_X dependence 69
5.4 Calorimeter acceptance for $2\varepsilon = 2.6$ 73
5.5 Calorimeter acceptance for diffractive and non-diffractive subsamples 75
5.5.1 Calorimeter acceptance for $E_{FCAL} < 1$ GeV 76
5.5.2 Calorimeter acceptance for $E_{FCAL} > 1$ GeV 78
5.6 Final acceptance and conclusions 79
5.7 Trigger efficiency and event loss 80

6 Luminosity monitor 84
6.1 Luminosity measurement 84
6.1.1 Bremsstrahlung event rate 84
6.1.2 Observed bremsstrahlung cross section 85
6.1.3 Summary of luminosity measurement 86
6.1.4 Calibration of photon detector 86
6.1.5 Calibration of electron detector 88
6.2 Monte Carlo Generation 88
6.2.1 Calibration of Monte Carlo 91
6.3 Comparisons of Monte Carlo and data 92
6.3.1 Exchanged photon energy 93
6.3.2 Beam tilts 93
6.3.3 Interaction vertex position 94
6.3.4 Acceptance of electrons 98
6.4 Radiative events 101

6.4.1 Bremsstrahlung overlay events 102

7 Total photoproduction cross section **104**
7.1 $\sigma_{\gamma p}$ from the Monte Carlo 104
7.1.1 Monte Carlo input 105
7.1.2 Reweighting Monte Carlo input to determine $\sigma_{\gamma p}$ 106
7.2 Final values for $\sigma_{\gamma p}$ 107
7.3 Physics conclusions 110
7.4 Summary 111

A Example run summary **113**

B Glossary **118**

References **121**

List of Figures

Figure 2-1 The basic diagram for electron-proton interactions 3
Figure 2-2 Photoproduction event topology at ZEUS 6
Figure 2-3 Photon–proton interactions of VMD 9
Figure 2-4 Direct processes 11
Figure 2-5 Resolved processes 12
Figure 2-6 Higher order corrections 17
Figure 2-7 Radiated photon energy 18
Figure 3-1 The HERA accelerator 19
Figure 3-2 The HERA injection system 21
Figure 3-3 Cross section of the ZEUS detector along the beam axis 22
Figure 3-4 Layout of an FCAL module 25
Figure 3-5 Layout of a CTD octant 27
Figure 3-6 Layout of the luminosity monitor 28
Figure 3-7 Schematic of the ZEUS CDAQ 30
Figure 3-8 Schematic of the TLT hardware 33
Figure 3-9 Overview of TLT control software 35
Figure 3-10 Overview of TLT filter software 37
Figure 4-1 Integrated luminosity collected by ZEUS 39
Figure 4-2 RCAL triggering layout 41
Figure 4-3 Calorimeter timing 42
Figure 4-4 Effect of prescales on calorimeter distributions 46
Figure 4-5 Electron and proton bunch structure 48
Figure 4-6 Egas background subtraction on z-vertex position of diffractive-like events 50
Figure 4-7 LUMI bremsstrahlung spectrum 52
Figure 4-8 LUMI energy spectrum for run 7200 53
Figure 4-9 Effect of coincidence background subtraction 53
Figure 4-10 Probability spectra of run 7200 for untagged bremsstrahlung events 54
Figure 4-11 LUMI electron and photon spectra after background subtraction 55
Figure 4-12 Average vertex position as a function of run number 57
Figure 4-13 Average run position on face of LUMI photon calorimeter 58
Figure 4-14 Number of events per luminosity for $W_{\gamma p}$ bins 60
Figure 5-1 Monte Carlo fits to data for four different calorimeter distributions 67
Figure 5-2 Diffractive generation characteristics 71
Figure 5-3 χ^2 minimization of diffractive ϵ dependence 72
Figure 5-4 Acceptance as a function of ϵ 72
Figure 5-5 Trigger threshold behavior 81
Figure 5-6 Event losses due to online trigger effects 82

Figure 6-1 Photon detector calibration 87
Figure 6-2 Changes to electron simulation 89
Figure 6-3 Simulation of high energy electrons 90
Figure 6-4 Calibration distributions 92
Figure 6-5 Calibration ratio 93
Figure 6-6 Photon impact positions 94
Figure 6-7 Electron acceptance as a function of the vertex position 95
Figure 6-8 LUMI electron comparison distributions 96
Figure 6-9 Reweighting of Monte Carlo vertex position 96
Figure 6-10 χ^2 minimization curves for LUMI distributions 97
Figure 6-11 Spectra comparison in the LUMI electron calorimeter 98
Figure 6-12 Scattered electron dependence on y and Q^2 100
Figure 6-13 Measured photon spectrum from radiative Monte Carlo 103
Figure 7-1 Total photon-proton cross section as a function of center of mass energy 108

List of Tables

Table 3-1 Operating parameters of the HERA collider 20
Table 4-1 Check of event prescale 46
Table 4-2 Electron energy ranges for $W_{\gamma p}$ bins 47
Table 4-3 Average electron and proton currents 49
Table 4-4 Effect of run cuts on data sample 58
Table 4-5 Effect of background subtraction on $W_{\gamma p}$ bins 59
Table 4-6 Events per luminosity for $W_{\gamma p}$ bins 61
Table 5-1 Diffractive generators 63
Table 5-2 Non-diffractive generators 63
Table 5-3 Monte Carlo subprocess acceptances 65
Table 5-4 Acceptances and fitted cross sections for calorimeter distributions 69
Table 5-5 Acceptance and fitted cross sections assuming $2\varepsilon = 2.6$ 73
Table 5-6 Acceptances and fitted cross sections assuming 7.0% elastic contribution 74
Table 5-7 Summary of systematic errors 75
Table 5-8 Diffractive and non-diffractive data events 76
Table 5-9 Monte Carlo acceptances and relative fractions for $E_{FCAL} < 1$ GeV 76
Table 5-10 Acceptances for the diffractive subsample 77
Table 5-11 Summary of systematic errors for the diffractive subsample 77
Table 5-12 Monte Carlo acceptances and relative fractions for $E_{FCAL} > 1$ GeV 78
Table 5-13 Acceptances for the non-diffractive subsample 79
Table 5-14 Summary of systematic errors for the non-diffractive subsample 79
Table 5-15 Total acceptance from diffractive and non-diffractive subsamples 80
Table 5-16 Final calorimeter acceptance and uncertainty 80
Table 5-17 Effects of increased trigger thresholds 83
Table 6-1 Electron acceptance for $W_{\gamma p}$ bins 99
Table 6-2 Correction for bremsstrahlung overlays 102
Table 6-3 Event loss due to photon energy cuts 103
Table 7-1 Corrections to cross section using ALLM parameterization 105
Table 7-2 Corrections to cross section using ALLM reweighted by 0.74 107
Table 7-3 Corrections to cross section using DL reweighted by 0.84 109
Table 7-4 Final γp cross section 109
Table 7-5 Corrections to γp cross section 109

1 Introduction

What are the basic building blocks of all matter, and how do these constituents interact? Looking for the answer to this question is the basis of particle physics. The present notion that all matter consists of leptons and quarks and the interactions between these constituents are mediated by gauge bosons is known as the "Standard Model" of particle physics. One of the basic tools of the particle physicist to examine these constituents is the collision of two particles at high energy.

In 1992, a new type of collider became operational at the Deutsches Elektronen SYnchrotron (DESY) accelerator complex in Hamburg, Germany. HERA, the world's first electron-proton (ep) collider, provided ep collisions with a center of mass energy, $\sqrt{s}$, an order of magnitude larger than had previously been attained in fixed target experiments. A fraction of the ep collisions occur via the exchange of an almost real photon. The interaction of the low virtuality photon with the proton can be used to examine photon-proton (γp) interactions. Fixed target experiments have shown that in collision with protons up to $\sqrt{s} \sim 20$ GeV, the photon behaves in a manner similar to hadrons. Until the completion of the HERA accelerator, the behavior of photons in γp collisions above 20 GeV center of mass energy had been unexplored.

The energy dependence of hadron-hadron (hh) interactions has been measured experimentally to decrease with energy up to $\sqrt{s} \sim 10$ GeV, and then to rise slowly. This energy dependence can be parametrized using Regge theory or minijet models based upon fits to the copious amounts of hh interaction data. At the highest fixed target energies, the γp cross section was also observed to follow this behavior. However, in addition to this hadron-like behavior, at the high $\sqrt{s}$ attainable at the HERA collider, photon interactions may also have a large component coming from parton processes. The models describing γp interactions and their predictions for the total cross section at HERA energies are discussed in Chapter 2.

Two large detectors, ZEUS and H1, have been built to study the ep interactions at HERA. A description of HERA and the components of the ZEUS detector used in this analysis is given in Chapter 3. The electrons and protons collide at the center of the detector, and the products from the ep interactions are measured in the hermetic ZEUS detector. The events used to study γp processes must first be separated from the other physics processes and any background processes with similar signals in the detector. This is the focus of Chapter 4.

In this analysis, the main calorimeter of the ZEUS experiment is used to measure the energy distributions of the hadronic system from the γp interactions in which the scattered electron is detected in the electron calorimeter of the luminosity monitor. These distributions are necessary to determine the cross sections for the various hadronic-like subprocesses used to describe γp interactions. From the subprocess cross sections, a correction for the detection efficiency of the main calorimeter is determined in Chapter 5. The scattered electron is used as a tag of the virtual exchanged photon. The energy of the photon is determined from the measured electron energy. The cross section is determined for photons with average energies of 10 GeV, 13 GeV and 16 GeV colliding with protons of 820 GeV. These photon energies correspond to scattered electron energies, $E_{e'}$, in the ranges 9.2 GeV $< E_{e'} <$ 18.2 GeV as discussed in Chapter 6. The ep cross section is obtained by counting the total number of ep events in each scattered electron energy bin and correcting this for the main calorimeter detection efficiency. An iterative comparison of the ep events from the data and a Monte Carlo model allows the determination of the γp cross section which in turn is used as an input for further Monte Carlo generation. The final results are given in Chapter 7.

2 Photoproduction at HERA

At HERA, measurement of photon-proton (γp) interactions is possible by studying the electron-proton (ep) collisions. The electroweak interaction between a colliding electron and proton is dominated by the interaction of a photon from the electron with the proton. This chapter will review the theory of γp interactions at high energy, and the relationship between the γp and the ep cross sections.

2.1 Electron-proton interaction

In the Standard Model [1] (SM) of elementary particle physics, the interaction between two particles occurs through the exchange of a *gauge boson*, as is illustrated in Figure 2-1 for a first order ep interaction. The boson, q, is exchanged between the incoming electron, e, and the incoming proton, p, producing the outgoing lepton, e', and the hadronic system, M_X.

According to the SM, there are two families of elementary, point-like particles. The members of the lepton family can exist as free particles and interact electromagnetically and weakly, while the quark family, which can also interact strongly, are confined in hadrons by the strong color field. For ep collisions, as illustrated in Figure 2-1, the interaction is either electromagnetic or

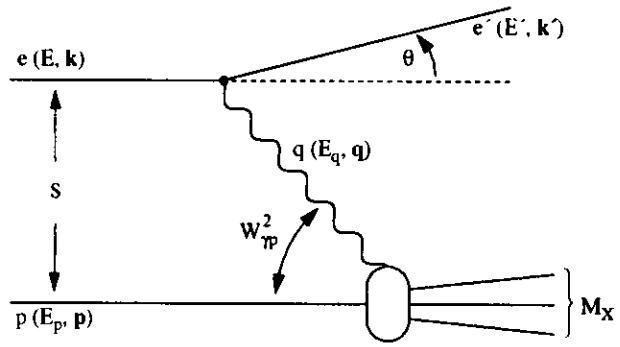

Figure 2-1 The basic diagram for electron-proton interactions

weak, thus the scattered lepton can be either an electron or an electron neutrino. In Figure 2-1, an electromagnetic interaction with a scattered electron, e', is shown.

According to electroweak theory [2], which combines electromagnetic and weak forces into one unified theory, the exchanged boson can be a photon (γ), a neutral weak vector boson (Z^0), or a charged weak vector boson ($W^{\pm}$). The total ep cross section, σ_{ep}, contains a propagator factor, G^2, for the gauge boson of the form

$$G(m) \propto 1/(q^2 - m^2). \tag{2-1}$$

Therefore, while the exchange of the massive[1] weak gauge bosons is allowed, virtual photon exchange is the dominant interaction for low q^2 ep interactions ($-q^2 << 1\ \mathrm{GeV}^2$) at ZEUS,

$$ep \rightarrow e' + \gamma^* p. \tag{2-2}$$

The events of Eqn. (2-2) can be further classified into deep inelastic scattering (DIS) events involving a highly virtual photon ($-q^2 = \vec{q}^2 - E_q^2 \gtrsim 1\ \mathrm{GeV}^2$), and photoproduction events with an almost real photon exchanged. DIS events are generally characterized at ZEUS by the electron being observed in the main calorimeter, while the slightly scattered electron of photoproduction escapes down the beampipe and has a possibility of being observed in the electron detector of the luminosity monitor (LUMIE)[2].

2.2 Kinematics

A full description of an ep interaction requires knowledge of the incoming and outgoing particles. Knowing the four momenta of the initial electron and proton and the identity of the scattered lepton, which for ep scattering of almost real photons is predominantly an electron, only two independent variables are needed to define the interaction of Figure 2-1. In the laboratory frame, it is often convenient to use the scattered electron energy, E' and the scattered electron polar angle, θ when the electron is observed in the main calorimeter. For photoproduction events, ZEUS does not have a measurement of θ, thus other variables are required to define the cross section.

It is common to define the cross section in terms of the Lorentz-invariant variables

$$Q^2 = -q^2 = -(e - e')^2, \tag{2-3}$$

$$y = p \cdot q / p \cdot e, \tag{2-4}$$

$$x = Q^2/(2p \cdot q). \tag{2-5}$$

1. The current masses for the weak gauge bosons are m_{Z^0} = 91.187 GeV and $m_{W^{\pm}}$ = 80.22 GeV [3].
2. See Section 3.5 for a description of the luminosity monitor detectors.

The square of the four momentum transfer to the proton, Q^2, defines the virtuality of the exchanged photon. When viewed from the rest frame of the proton, y defines the fraction of energy lost by the electron in the interaction. If viewed from a frame where the proton has infinite momentum, the variable x defines the fraction of the proton momentum participating in the interaction. The above three variables are related through the reduced centre of mass energy squared,

$$\tilde{s} = 2e \cdot p \cong 4EE_p, \tag{2-6}$$

by the relation

$$Q^2 = xy\tilde{s}. \tag{2-7}$$

To an excellent approximation, $\tilde{s}$ is equivalent to the ep center of mass energy squared,

$$s = (e+p)^2 = m_e^2 + m_p^2 + 2e \cdot p \cong \tilde{s}, \tag{2-8}$$

where $\sqrt{s}$, the centre of mass energy of the ep interaction, defines the maximum energy available to any process in the collision. Also of interest is the center of mass energy of the γp system,

$$W_{\gamma p}^2 = (q+p)^2. \tag{2-9}$$

The boson propagator term, G^2, gives the ep cross section a Q^2 dependence $\sigma_{ep} \propto Q^{-4}$. Therefore the majority of ep interactions will occur at low Q^2 via the exchange of an almost real photon ($Q^2 \approx 0$ GeV^2). Expanding Eqn. (2-3) gives

$$Q^2 = -m_e^2 - m_{e'}^2 + 2EE' - 2kk'\cos\theta, \tag{2-10}$$

where all variables are defined in Figure 2-1. Here, Q^2 is smallest when $\cos\theta = 1$ which gives $\theta = 0$. The minimum possible Q^2 is then

$$Q_{min}^2 = -m_e^2 - m_{e'}^2 + 2EE' - 2kk' \approx -m_e^2 - m_{e'}^2 + 2EE'\left(1 - 1 + \frac{m_e^2}{2E^2} + \frac{m_{e'}^2}{2E'^2}\right). \tag{2-11}$$

Also expanding y from Eqn. (2-4) for $\theta = 0$ gives

$$y \approx 1 - \frac{E'}{E}\cos^2\frac{\theta}{2} = 1 - \frac{E'}{E} \text{ for } \theta = 0. \tag{2-12}$$

Using Eqn. (2-12) and $m_e^2 \cong m_{e'}^2$ gives

$$Q_{min}^2 \approx \frac{m_e^2 y^2}{1-y}. \tag{2-13}$$

Q_{min}^2 defines the minimum four momentum transferred by the photon as allowed by energy and momentum conservation. Q^2 can now be expressed in terms of Q_{min}^2 by

$$Q^2 \approx Q_{min}^2 + 4EE'\sin^2\frac{\theta}{2}. \tag{2-14}$$

As was discussed in Section 2.1, the slightly scattered electron escapes undetected through the beampipe as illustrated in Figure 2-2. This Figure depicts a typical photoproduction event where the initial electron, which enters from the left, interacts with a proton entering from the right, colliding in the center of the ZEUS detector (see Chapter 3 for a description of the ZEUS detector). The slightly scattered electron escapes down the beampipe and can be detected in LUMIE. A photon calorimeter (LUMIG) also exists to detect photons from background events, such as bremsstrahlung interactions (see Section 2.6), or from higher order effects such as real photon emission from the electron (see Section 2.5.3). The low Q^2 events in which the electron is detected by LUMIE are know as *tagged* photoproduction events. The events in which the scattered electron escapes detection entirely are known as *untagged* events. The tagged events allow the calculation of the kinematic variables y and Q_{min}^2 using the scattered electron energy, E'. Although the electron scattering angle cannot be measured directly, the acceptance of LUMIE limits the angle with which the scattered electron may be detected (see Section 6.3.4), thus effectively limiting the Q^2 range.

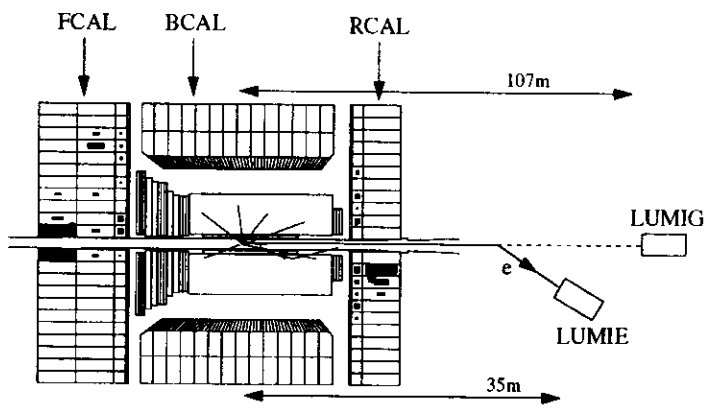

Figure 2-2 Photoproduction event topology at ZEUS
A typical photoproduction event where the initial electron enters from the left, the initial proton from the right. The electron from a low Q^2 event can exit through the beampipe and deposit energy in LUMIE. Photons from background processes (i.e., bremsstrahlung) and higher order effects (i.e., initial and final state radiation) continue straight and may be detected by LUMIG.

2.3 Photoproduction

The current understanding of photon interactions is of a photon that can fluctuate between a *bare* photon state and virtual hadronic states, where the small hadronic component may undergo conventional hadronic interactions [4]. The probability for the photon to interact as a hadron depends on the photon coupling to a quark-antiquark pair, thus is of order $\sqrt{\alpha}$. In this view, the photon can interact via its hadronic component provided that the fluctuation time is larger than the interaction time, $t_f > t_{int}$ [5]. For the virtual photons of *ep* interactions

$$t_f \approx \frac{2E_q}{Q^2 + m_V^2} \approx \frac{2E_q}{m_V^2} \tag{2-15}$$

for the small virtualities of tagged photoproduction ($Q^2 < 0.02$ GeV^2 from Section 6.3.4) at ZEUS. This behavior is similar to that of real photon scattering. Here, m_V is the mass of the vector meson fluctuation of the photon (see Section 2.3.1), typically the ρ mass (770 MeV). The fluctuation time is calculated in the rest frame of the proton, resulting in a fluctuation time of $t_f \approx 10^4$ fm/c for the case of a 12 GeV photon incident on an 820 GeV proton. The interaction time is of the order of the proton radius,

$$t_{int} \approx r_p, \tag{2-16}$$

resulting in $t_{int} \approx 0.8$ fm/c much smaller than t_f.

All the possible photon interactions must be considered for a complete description of γ*p scattering to obtain the final γ*p cross section. Even with the small fraction of hadronic states, of order $\sqrt{\alpha}$, the large majority of observable photon interactions are expected to happen through the hadronic component due to the much larger *hN* cross section [6]. The vector meson dominance (VMD) model successfully describes this component of γ*p interactions. A similar interaction, which has been omitted until this point, is the photon coupling to a lepton pair, or pair production. The cross section for pair production is far larger than for $q\bar{q}$ production; however, to first order, the produced lepton pair would not undergo strong interactions, and this component can be neglected and will not appear further in this analysis [6]. A second category of events, known as anomalous events, arises when the photon is resolved into a high mass, perturbative quark-antiquark ($q\bar{q}$) pair, one of which interacts with the proton. A third category of events where the bare photon interacts with a parton from the proton, the so called direct events, must also be considered. The total photoproduction cross section is given from the sum [7] of the three mentioned contributions:

$$\sigma_{tot}^{\gamma^* p}(W, Q^2) = \sigma_{VMD}^{\gamma^* p}(W, Q^2) + \sigma_{direct}^{\gamma^* p}(W, Q^2) + \sigma_{anomalous}^{\gamma^* p}(W, Q^2). \tag{2-17}$$

The total cross section for different models is determined by assuming different cross sections for the individual pieces of Eqn. (2-17).

2.3.1 Vector meson dominance

As stated above, the premise of VMD is that the photon can fluctuate into a hadronic state which can undergo hadronic interactions. The hypothesis of VMD is that the photon hadronic state is composed solely of three vector meson states with the same quantum numbers as the photon ($J^{PC} = 1^{--}$), namely the ρ,ω, and φ mesons. VMD also asserts that the bare component of the photon cannot interact with hadrons. VMD is found to account for only 80% of the experimental cross section [4]. The remainder is sometimes accounted for by the addition of heavier mass states. This is known as generalized vector meson dominance (GVMD).

The VMD prediction for the transverse and longitudinal components of the total cross section [8][9] is

$$\sigma_T^{\gamma^* p}(W, Q^2) = \sum_{V = \rho, \omega, \phi} \frac{e^2}{f_V^2} \left(\frac{m_V^2}{m_V^2 + Q^2} \right)^2 \sigma_T^{Vp}(W)$$

$$\sigma_L^{\gamma^* p}(W, Q^2) = \xi \frac{Q^2}{m_V^2} \sigma_T^{\gamma^* p}(W, Q^2) \tag{2-18}$$

at a centre of mass energy W and photon virtuality Q^2. The coupling of the vector meson to the photon is given by f_V which is determined from e^+e^- annihilation [4]. The variable ξ, which is a constant of $O(1)$, is introduced since the longitudinal and transverse polarized vector mesons may not have the same cross sections. For the low Q^2 tagged photoproduction at ZEUS, the contribution from the longitudinal component of the VMD cross section is assumed to be negligible and is ignored (see Section 2.5.3).

The hadron–like interactions of the photon are thus described in terms of Vp scattering. However, a description using Vp scattering is not very useful unless it can be measured directly. The vector mesons are too short lived to create a beam for scattering directly. However, the additive quark rule states that the valence quarks determine the behavior of hadron-hadron collisions [6], hence $\sigma_{tot}^{\rho^0 p} \approx \sigma_{tot}^{\omega p} \approx \frac{1}{2}(\sigma_{tot}^{\pi^+ p} + \sigma_{tot}^{\pi^- p})$ and $\sigma_{tot}^{\phi p} \approx \sigma_{tot}^{K^+ p} + \sigma_{tot}^{K^- p} - \frac{1}{2}(\sigma_{tot}^{\pi^- p} + \sigma_{tot}^{\pi^+ p})$. The different classes of hadronic scattering, such as elastic, diffractive and non-diffractive events, carry over to Vp scattering and are described in more detail below.

2.3.1.1 Elastic diffraction

Elastic scattering refers to the process

$$\gamma^* p \rightarrow Vp \tag{2-19}$$

as shown in Figure 2-3a. The partial differential cross section, $d\sigma/dt$, from elastic proton-proton (pp) scattering was observed to display characteristics reminiscent of diffraction of light by a circular aperture [10]. Here, t is the square of the four momentum transfer between the hadronic systems. From optics, the intensity of scattered light with wave number k at an angle θ beyond a circular aperture of radius R with respect to the intensity at $\theta = 0$ is given by

$$\frac{I}{I_0} = 1 - \frac{R^2}{4}(k\theta)^2. \tag{2-20}$$

In direct analogy, the partial cross section for elastic pp scattering with respect to zero angle scattering from fits to data is given by

$$\frac{d\sigma/dt}{(d\sigma/dt)_{t=0}} \propto e^{b_{el}t} \approx 1 - b_{el}(p\theta)^2. \tag{2-21}$$

Equating Eqn. (2-20) and Eqn. (2-21) gives

$$b_{el} = \frac{R^2}{4}. \tag{2-22}$$

As in optics, the slope of the elastic scattering is related to the size of the scattering object [10].

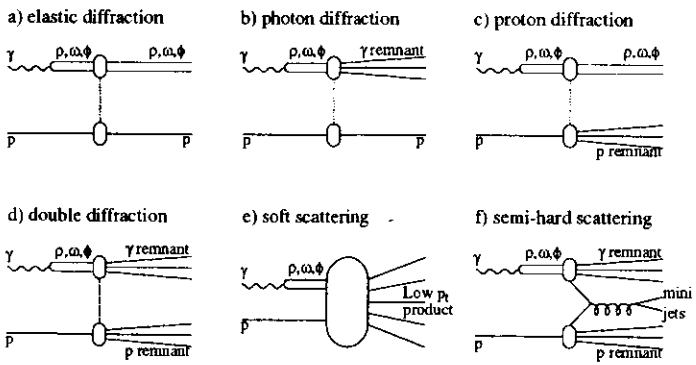

Figure 2-3 Photon–proton interactions of VMD
The incoming photon, γ, first transforms into a vector meson, ρ,ω,φ, before interacting with the proton, p. The various processes of hadron interactions are shown. a) shows elastic scattering where the proton and the vector meson both remain intact. b), c) and d) show diffractive scattering where one or both of the proton and vector meson diffracts into a higher mass state. e) and f) show non-diffractive soft and hard processes.

Two separate derivations in [11] estimate the contribution to the total cross section due to elastic scattering processes to be $O(10\%)$ at HERA energies. The comparisons utilize the relation between the elastic and total cross section from the optical theorem [6],

$$\left.\frac{d\sigma}{dt}\right|_{t=0} = \frac{\sigma_{tot}^2}{16\pi}. \tag{2-23}$$

The estimates will be used for comparison with the results of Chapter 5.

2.3.1.2 Diffractive scattering

In inelastic diffractive processes, one or both of the incoming particles diffract into a higher mass state as shown in Figure 2-3b,c,d. They are classified according to the diffracted particle as follows [12]:

$$\text{proton diffraction: } \gamma^* p \to VX_p, \tag{2-24}$$

$$\text{photon diffraction: } \gamma^* p \to X_V p, \tag{2-25}$$

$$\text{double diffraction: } \gamma^* p \to X_V X_p. \tag{2-26}$$

The double differential cross section for hadron dissociation, $hp \to Xp$, is known to vary exponentially in t and to have an M_X^{-2} dependence [13],

$$\frac{d^2\sigma}{dtdM_X^2} \propto \frac{e^{b_{in}t}}{(M_X^2)^{\varepsilon}}, \tag{2-27}$$

where M_X is the mass of the diffracted state. A further ε dependence on M_X is added in view of the CDF results [14] which show an $M_X^{-2.2}$ dependence. The inelastic slope, b_{in}, is measured to be about one half of the elastic slope (see Section 2.3.1.1 above) and appears to be independent of M_X for $M_X > 4$ GeV (photon diffraction) [13] or $M_X > 5$ GeV (proton diffraction) [10].

2.3.1.3 Non-diffractive scattering

Non-diffractive hadron-hadron scattering can be further subdivided into soft and semi-hard interactions. The soft events, shown in Figure 2-3e, are characterized by small p_T and are not in the diffractive classifications above. The internal energy scale of the events is too small for perturbative calculations, so they must be modelled on parameterizations based on previous experimental measurements [12].

The vector mesons, like all hadrons, are made up of valence quarks, and a sea of virtual gluons and $q\bar{q}$ pairs. Each of the sea partons carries only a small fraction of the total momentum of the hadron. The pointlike constituents of the proton and the vector meson can interact directly as

shown in Figure 2-3f. The small Q^2 of photoproduction implies that the virtual photon probes the low x region of the proton from Eqn. (2-5), thus this type of interaction is dominated by the sea partons from each hadron and only a small fraction of the total center of mass energy is involved. The products of the interaction hadronize into minijets, so named because of the small momentum fraction carried by each interacting constituent. This semi-hard contribution is usually combined with the anomalous component into a resolved photon component (see Section 2.3.2 below).

2.3.1.4 VMD summary

The resulting VMD contribution to the total cross section can be expressed as a combination of all the individual hadronic processes,

$$\sigma^{\gamma p}_{VMD} = \sigma^{\gamma^* p}_{elas} + \sigma^{\gamma^* p}_{pdif} + \sigma^{\gamma^* p}_{\gamma dif} + \sigma^{\gamma^* p}_{ddif} + \sigma^{\gamma^* p}_{ndif} \qquad (2\text{-}28)$$

where *elas* refers to the elastic interactions described in Section 2.3.1.1, *pdif*, *γdif* and *ddif* refer to proton diffractive, photon diffractive and double diffractive processes respectively, described in Section 2.3.1.2, and *ndif* refers to the non-diffractive processes of Section 2.3.1.3.

2.3.2 Parton level processes

In parton level processes, the photon interacts with a parton from the proton. Parton level processes are further subdivided into direct processes and anomalous processes.

In direct processes, the photon directly couples to a charged parton from the proton as shown in Figure 2-4. With the full energy of the photon involved in the interaction, the direct mechanism is the dominant process for the highest p_T jets in photoproduction and is characterized by the absence of a photon remnant.

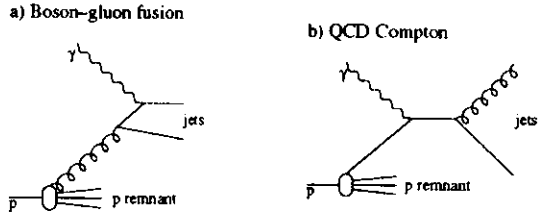

Figure 2-4 Direct processes
The photon directly interacts with a parton in the proton. In boson-gluon fusion, a), the photon combines with a gluon producing a quark-antiquark pair. In QCD Compton, b), the photon couples to a quark from the proton.

Although the basic assumption of VMD is that the bare photon does not interact with the proton, experimental evidence exists that shows direct interactions do in fact occur. In comparing γp interactions to πp and Kp interactions, the OMEGA Photon Collaboration observed an excess of charged particles at high p_T [15], which is attributed to direct interactions. An unambiguous signal for direct events has also been observed by ZEUS [16] and H1 [17] in the photoproduction of di-jet events.

In anomalous processes, the photon splits into a $q\bar{q}$ pair, one of which interacts with a parton from the proton as shown in Figure 2-5. This closely resembles the VMD hard non-diffractive scattering described in Section 2.3.1.3 and shown in Figure 2-3f. The two processes differ by the parton distribution function describing the photon. The anomalous photon is described by a $q\bar{q}$ pair which share the momentum and energy of the photon whereas the VMD photon is described by a vector meson parton distribution. Since only the $q\bar{q}$ pair share the momentum of the photon, the anomalous parton distribution is much harder than the vector meson parton distribution. Therefore, the high p_T jet events with a photon remnant are dominantly from the anomalous contribution and not the VMD component.

Since the anomalous and hard VMD component are so similar, the usual convention is to combine the two into one resolved contribution. This is accomplished by creating a single photon structure function, similar to the proton structure function, which is a combination of the two individual components, defined as

$$F_2^{\gamma} = F_2^{VMD} + F_2^{anomalous}. \qquad (2\text{-}29)$$

2.4 Parameterizing the total photoproduction cross section

In Section 2.3, the various pieces making up the total cross section were described. Different theoretical predictions are obtained by applying different weights to the components of Eqn. (2-17) and Eqn. (2-28). Three classifications of predictions are described below.

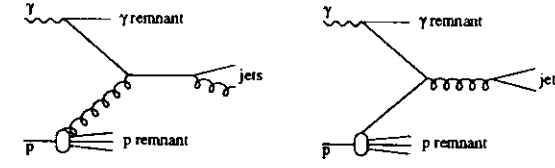

Figure 2-5 Resolved processes
The photon splits into a quark-antiquark pair, one of which subsequently interacts with a parton from the proton.

2.4.1 Regge theory parameterizations

The Regge theory parameterizations are based on the VMD photon and Regge phenomenology [18]. In Regge theory, the interaction of two particles is mediated by the exchange of an effective particle called the reggeon. The predicted behavior from reggeon exchange is a cross section falling as a power of the γp center of mass energy. A review [3] of the cross section dependencies for different hadronic interactions shows that hadronic cross sections do fall off at low energy, and then begin to rise again. This rising behavior is attributed to the exchange of the pomeron, an effective particle with the quantum numbers of the vacuum.

The total cross section in Regge theory can be expressed as

$$\sigma_{tot}^{\gamma p} = \sigma_{\mathcal{P}}^{0} \cdot s^{\alpha_{\mathcal{P}}-1} + \sigma_{\mathcal{R}}^{0} \cdot s^{\alpha_{\mathcal{R}}-1}, \qquad (2\text{-}30)$$

where s is the square of the γp center of mass energy (in GeV^2), the first term is attributed to pomeron exchange and the second term to reggeon exchange [19]. $\alpha_{\mathcal{P}}$ and $\alpha_{\mathcal{R}}$ denote the pomeron and reggeon angular momentum respectively, determined when the square of the incoming and outgoing proton four momentum difference, $t = 0$. $\sigma_{\mathcal{P}}^{0}$ and $\sigma_{\mathcal{R}}^{0}$ represent the coupling of the pomeron and reggeon to a specific particle. The determined powers, $\alpha_{\mathcal{P}}$ and $\alpha_{\mathcal{R}}$, are universal, whereas the couplings $\sigma_{\mathcal{P}}^{0}$ and $\sigma_{\mathcal{R}}^{0}$ are dependent upon the process.

Donnachie and Landshoff (DL) [19] have performed a fit to existing data to determine the powers and couplings of Eqn. (2-30) for different reactions. The effective powers were fit using pp and $p\bar{p}$ data, resulting in $\alpha_{\mathcal{P}} - 1 = 0.0808$ and $\alpha_{\mathcal{R}} - 1 = -0.4525$. Fits to γp data resulted in couplings of $\sigma_{\mathcal{P}}^{0} = 67.7\ \mu\mathrm{b}$ and $\sigma_{\mathcal{R}}^{0} = 129\ \mu\mathrm{b}$.

Using the same method as [19] above, the CDF collaboration have determined another parameterization (DL2) with the inclusion of new measurements at $\sqrt{s} = 546$ and 1800 GeV [20]. This prediction differs in the pomeron angular momentum, which is measured to be $\alpha_{\mathcal{P}} - 1 = 0.112$. The new fit results in $\alpha_{\mathcal{R}} - 1 = -0.402$, $\sigma_{\mathcal{P}}^{0} = 54.9\ \mu\mathrm{b}$ and $\sigma_{\mathcal{R}}^{0} = 139\ \mu\mathrm{b}$ for photoproduction.

The basis of the Abramowicz, Levin, Levy, Maor (ALLM) [21] prediction is the smooth description of data through the whole range of possible Q^2 values, from $Q^2 = 0$ to the highest measured values. The low Q^2 photoproduction region is described by Eqn. (2-30) with $\alpha_{\mathcal{P}} - 1 \approx 0.045$ and $\alpha_{\mathcal{R}} - 1 \approx -0.6$.

2.4.2 Minijet parameterizations

The total cross section for minijet parameterizations can be expressed as

$$\sigma_{tot}^{\gamma p} = \sigma_{soft} + \sigma_{jet}, \qquad (2\text{-}31)$$

where σ_{soft} arises from non-perturbative VMD interactions which are constant with energy above the low energy region, and σ_{jet} from hard perturbative jet processes which increase rapidly with energy. Thus the rise of the total cross section is attributed solely to the hard jet processes. The one important input to the calculation of the minijet cross section is the p_t cutoff, p_T^{min}, below which perturbative calculations cannot be used. The value of p_T^{min} used has a large effect on the calculated cross section at high energies. The rapid rise of the cross section is usually attributed to the small x behavior of the gluon density functions used. At higher centre of mass energies, smaller values of x are sampled. Thus the behavior of the cross section depends on the structure function used, and the value of p_T^{min}. Direct interactions are also assumed to contribute a small amount to the total cross section. The minijet approach in general predicts a faster rise to the cross section than other approaches, and the different models should be resolvable at HERA energies.

2.4.3 Schuler & Sjöstrand parameterization

The model of Schuler and Sjöstrand [6] attempts to smoothly describe the cross section from soft to hard processes. The basic assumption is that photon interactions fall into three categories: bare, vector meson and perturbative $q\bar{q}$. The distinction between the categories is made by two p_t cutoff scales. The first cutoff scale, $p_0 \approx m_\phi/2 \approx 0.5$ GeV, is applied to the $\gamma \rightarrow q\bar{q}$ vertex. If the common p_t of the $q\bar{q}$ is less than p_0 then a vector meson wave function is used. This is the same as VMD from Section 2.3.1. Direct and anomalous events are then characterized by $p_t > p_0$. A second p_t cutoff, $p_{\perp min}$, defines the minimum p_t of hard parton-parton interaction in hadronic events. This is directly applicable to the hard non-diffractive interactions of VMD. $p_{\perp min}$ is assumed to be energy dependent, and of the order of 1.3 GeV at HERA energies [22]. Events above $p_{\perp min}$ are assumed to undergo a hard interaction and be perturbatively calculable. Below $p_{\perp min}$, the events are described by a minimum bias phenomenology. A corresponding $p_{\perp min}$ cutoff is also necessary to describe anomalous events, but here, the cutoff is found to be slightly higher, approximately 2.2 GeV. Variations on the value of p_0 and $p_{\perp min}$ change the predictions for the total cross section.

2.5 Measuring the total photoproduction cross section

In the preceding sections, the various processes and parameterizations of real photoproduction interactions have been reviewed. At HERA, however, the almost real photon originates from the scattered electron beam. Although this is the dominant interaction, what is measured is the total ep cross section, which also includes the electron-photon vertex (see Figure 2-1). To measure the γp cross section, the ep cross section must be related to the γp cross section.

2.5.1 Relating ep and γp cross sections

A detailed derivation of the relation between the γp and the ep cross sections is given in [12]. In summary, the total ep cross section can be written in the form

$$\frac{d^2\sigma_{ep}(y,Q^2)}{dydQ^2} = \frac{\alpha}{2\pi}\frac{1}{Q^2}\left(\left(\frac{1+(1-y^2)^2}{y} - 2\frac{(1-y)}{y}\frac{Q^2_{min}}{Q^2}\right)\sigma_T(y,Q^2) + 2\frac{(1-y)}{y}\sigma_L(y,Q^2)\right), \quad (2\text{-}32)$$

where σ_T and σ_L are the $\gamma^* p$ transverse and longitudinal components of the cross section respectively, and Q^2_{min} is given by Eqn. (2-13).

The two components of the cross section for the virtual photon can be compared for VMD by taking the ratio from Eqn. (2-18),

$$\sigma_L/\sigma_T \sim Q^2/m_V^2. \quad (2\text{-}33)$$

As long as the virtuality of the photon is kept small compared to the characteristic scale of the interaction (i.e., $Q^2 << m_V^2 \sim 1\ \mathrm{GeV}^2$ in this case), the longitudinal component of the virtual photon cross section is small. Also, from Eqn. (2-18), the Q^2 dependence of σ_T is very small for $Q^2 << m_V^2$, which means that the uncertainties in the extrapolation $Q^2 \to 0$ for real photons are also small. For the direct and anomalous components, the characteristic scale is defined by the QCD mass scale, $\Lambda_{QCD} \sim 0.2$ GeV, thus the longitudinal component becomes negligible for $Q^2 << \Lambda^2_{QCD}$. As long as Q^2 is much smaller than the characteristic scale, be it the vector meson mass or Λ_{QCD}, the virtual photon is very similar to a real photon. Numerical estimates for the tagged photoproduction at ZEUS in [9] also show that the effect of σ_L should be negligible. The approach taken in this paper is the Taylor expansion of σ_L and σ_T as a power series in Q^2. The first derivatives of σ_L and σ_T are then evaluated and shown to give a negligible correction. The ability to ignore the non-zero mass and longitudinal polarization is known as the equivalent photon approximation (EPA) for ep scattering [12].

Using the above results, Eqn. (2-32) reduces to

$$\frac{d^2\sigma_{ep}(y,Q^2)}{dydQ^2} = \frac{\alpha}{2\pi}\frac{1}{Q^2}\left(\frac{1+(1-y^2)^2}{y} - 2\frac{(1-y)}{y}\frac{Q^2_{min}}{Q^2}\right)\sigma^{\gamma p}_{tot}(y), \quad (2\text{-}34)$$

where $\sigma^{\gamma p}_{tot}$ is the total γp cross section for real photons, and is thus independent of Q^2. Integrating over Q^2, with Q^2_{max} given by geometric acceptances and the constraint that Q^2_{max} is much smaller than the characteristic scale, gives

$$\frac{d\sigma_{ep}(y)}{dy} = \frac{\alpha}{2\pi}\left(\frac{1+(1-y^2)^2}{y}\ln\frac{Q^2_{max}}{Q^2_{min}} - 2\frac{(1-y)}{y}\left(1-\frac{Q^2_{min}}{Q^2_{max}}\right)\right)\sigma^{\gamma p}_{tot}(y). \quad (2\text{-}35)$$

The y dependent term in parenthesis can be thought of as the flux of photons accompanying the electron, and can be expressed as $f_\gamma(y)$ giving

$$\frac{d\sigma_{ep}(y)}{dy} = f_\gamma(y)\,\sigma^{\gamma p}_{tot}(y). \quad (2\text{-}36)$$

2.5.2 Measuring the γp cross section using the EPA

In principle, the total ep cross section is obtained by counting the number of interactions in a given region of phase space per unit of total luminosity. Eqn. (2-36) can then be used, with the calculated flux, f_γ, to arrive at the total γp cross section for a given y. In practice, this is far too simple a view as detector effects play an important role in the total events counted. Allowances must be made for the acceptance of events in each of the detector components required in the event trigger (see Section 5.6 and Section 6.3.4),

$$\sigma^{\gamma p}_{tot}(y) = \frac{1}{f_\gamma(y)}\frac{N(y)}{\mathcal{L}}\frac{1}{A(y)}, \quad (2\text{-}37)$$

where $N(y)$ is the total number of events for the ep interactions, $\mathcal{L}$ is the integrated luminosity, and $A(y)$ is the acceptance for the events in the detector.

The event topology for tagged photoproduction is shown in Figure 2-2. A combined signal in the rear calorimeter (RCAL) and in LUMIE is required to trigger an event (see Section 4.1). Thus the acceptance may be expressed as

$$A \equiv A_{LUMIE*RCAL}. \quad (2\text{-}38)$$

As was shown in Section 2.5.1, the Q^2 dependence of the final hadronic system is negligible. Combined with the small electron scattering angle required by the acceptance of LUMIE, $Q^2 < 0.02\ \mathrm{GeV}^2$ (see Section 6.3.4), this leads to a γ^* which essentially travels in the same direction as the electron beam. The γ^* cannot significantly boost the hadronic system away from the beam axis, hence for a given photon energy, the final hadronic system is independent of the scattered electron. This implies uncorrelated acceptances for LUMIE and RCAL, thus

$$A_{LUMIE*RCAL} = A_{LUMIE}A_{RCAL}. \quad (2\text{-}39)$$

In practice, the cross section measurement is performed over a range of y (or equivalently, $W \sim 2\sqrt{yEE_p}$). Eqn. (2-39) can be used as long as the y dependence of A_{RCAL} is small over the range of values used, as it is for the three bins used in this analysis (see Section 5.6).

2.5.3 Radiative Corrections

Radiative corrections describe the effect of higher order QED diagrams at the electron vertex on the measured total cross section. Figure 2-6 shows several examples of higher order processes that must be taken into account. There are two methods that can be used to account for the effect of these radiative corrections on the measured value:

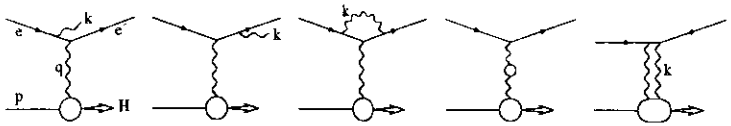

Figure 2-6 Higher order corrections
The processes of higher order corrections involve initial state radiation, final state radiation, vertex corrections, photon vacuum polarization, and two photon exchange.

- the measured cross section can be determined assuming only lowest order (Born approximation) terms, and the effect of higher order terms can be assessed afterwards and the measured value corrected;
- a Monte Carlo with full radiative corrections can be used when determining the cross section.

This analysis will use the latter method in determining the total cross section.

The higher order terms depicted in Figure 2-6 all modify the electron-photon vertex when the cross section is calculated. Instead of the neat and compact form of Eqn. (2-36), a much more complicated relation between the γp and ep cross sections results. In addition, the initial and final state radiation terms also change the kinematic variables measured in the detector. Since a real radiated photon is emitted from the electron line, both the exchanged photon and the real photon share the energy loss of the scattered electron. Since the electron scatters at basically zero angle and the photon is collinear with the electron, no distinction is made between initial and final state radiation. The resulting measured electron energy, E', depends on both the exchanged and radiated photon, hence the calculation of the kinematic variables y, W, Q^2_{min} is incorrect. The net result is a migration from bins of lower W into bins of higher W. The radiated and exchanged photons share the available energy, with one of the photons tending to take most of the energy as shown in Figure 2-7 using the HERACLES4.2 [23] event Monte Carlo. A cut on the exchanged photon energy, as required by the RCAL trigger (see Section 6.4) greatly reduces the effects from the radiative events. The migrations of the kinematic variables must be properly accounted for when determining the final cross section.

2.6 Bremsstrahlung

Another radiative process, know as the bremsstrahlung interaction,

$$ep \rightarrow e'p\gamma, \tag{2-40}$$

describes the emission of real photons from an electron in the presence of a relativistic proton. First calculated in 1934 by Bethe and Heitler [24], the total cross section for the bremsstrahlung of a relativistic electron ($E >> m_e$) on a proton producing a photon with an energy, E_q, is given by

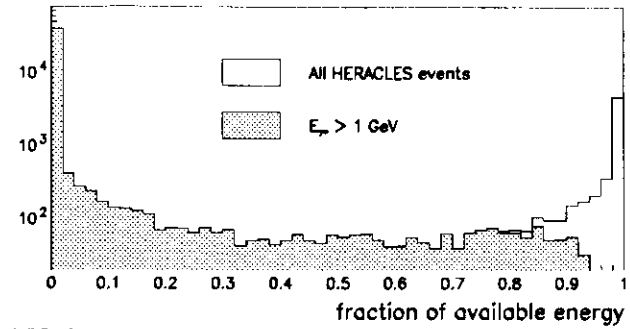

Figure 2-7 Radiated photon energy
The fraction of energy (E_γ+E_{γ^*}) carried by the radiated photon for the HERACLES4.2 event generator is shown. Imposing an energy cut on the exchanged photon greatly reduces the radiative contamination.

$$\frac{d\sigma}{dE_q} = 4\alpha r_e^2 \frac{E'}{EE_q}\left(\frac{E}{E'} + \frac{E'}{E} - \frac{2}{3}\right)\left(\ln\frac{4E_pEE'}{m_pm_eE_q} - \frac{1}{2}\right) \tag{2-41}$$

which is accurate to better than 1%. Here, E, and E' are the initial and scattered electron energy respectively, m_e and m_p are the masses of the electron and proton respectively, α is the fine structure constant ($\approx$1/137) and r_e is the classical radius of the electron. To an excellent approximation, the photon energy can be expressed as $E_q = E - E'$ as very little energy is exchanged between the electron and the proton.

The final state electron and photon from the interaction emerge at very small angles with respect to the initial electron direction. The angular distribution of the photon follows the distribution [25]

$$\frac{d\sigma}{d\theta_\gamma} \propto \frac{\theta_\gamma}{((m_e/E)^2 + \theta_\gamma^2)^2}, \tag{2-42}$$

where θ_γ is the angle between the scattered photon and the initial electron direction. The distribution peaks at $m_e/\sqrt{3}E$ which, for an initial electron energy of 26.7 GeV, corresponds to $\theta_\gamma \approx 0.011$ mrad.

3 The experimental setup

3.1 The electron-proton collider HERA

The Hadron-Electron Ring Anlage (HERA) is the world's first electron-proton colliding beam facility, located at the Deutches Elektronen SYnchrotron (DESY) in Hamburg, Germany. The accelerator, shown in Figure 3-1, consists of two independent rings, one to house the electrons (or positrons) and one to house the protons, 6.34 km in circumference and located 10 – 25 m underground. The accelerator is designed to collide 30 GeV electrons on 820 GeV protons at four experimental halls located around the ring producing interactions at a center of mass energy, $\sqrt{s}$ = 314 GeV.

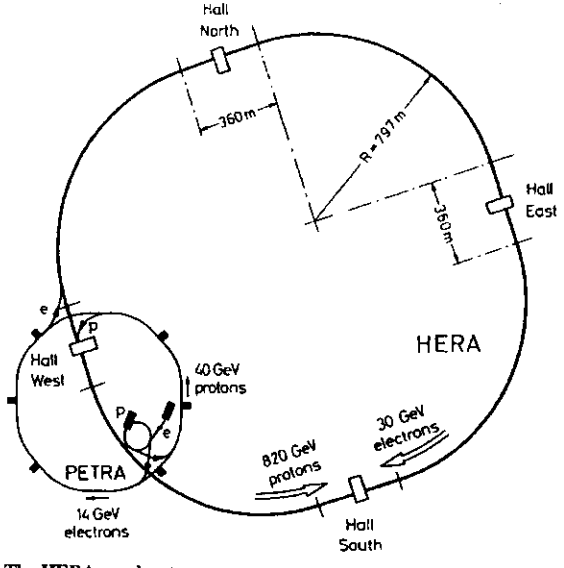

Figure 3-1 The HERA accelerator
Protons and electrons are accelerated in opposite directions and brought into collision at the four experimental halls located around the ring. The ZEUS detector is located in the South hall, and the H1 detector is in the North collision hall.

Two separate rings are required to accelerate the electrons and protons. The proton ring, which lies above the electron ring, is made up of superconducting magnets which guide the beam to each of the four colliding halls. The proton beam energy is limited by the magnetic field attainable by the dipole bending magnets located around the ring. The electron beam, which is steered through the ring with conventional magnets, has its attainable energy limited by the radio frequency (RF) power needed to replace the energy lost by the electrons due to synchrotron radiation. This is not a consideration for the proton beam since the energy loss from synchrotron radiation goes as m^{-4} and the losses for the much more massive proton are small.

As was mentioned, HERA collides 30 GeV electrons and 820 GeV protons, grouped in 220 bunches spaced equally around the ring. This spacing corresponds to consecutive bunches separated by 28.8 m and crossing every 96 ns, or with a frequency of 10.4 MHz. In 1993, the accelerator did not reach its design parameters, achieving an electron energy of 26.67 GeV and colliding 84 bunches, with an additional 6 proton pilot bunches and 10 electron pilot bunches. The pilot bunches are unpaired electron and proton bunches with no colliding partner. They are used to study background processes and to subtract these backgrounds in the colliding bunches. A summary of the beam parameters is shown in Table 3-1.

HERA parameter	proton beam		electron beam	
	design	1993 run	design	1993 run
Tunnel circumference (m)	6336			
Nominal energy (GeV)	820		30	26.7
Center of mass energy (GeV)	314 (296 for 1993)			
Number of bunches	210	90	210	94
Bunch crossing angle (mrad)	0			
Bunch distance	28.8 m (96 ns)			
Circulating current (mA)	160	11	58	8
Beam size x (mm)	0.32		0.3	
Beam size y (mm)	0.1		0.04	
Beam size z (mm)	110		7.8	
Angular beam spread x (mrad)	0.03		0.13	
Angular beam spread y (mrad)	0.10		0.10	

Table 3-1 Operating parameters of the HERA collider

In order to achieve the beam structure mentioned, the older accelerators at DESY have been modified to function as the injection system for the HERA ring as shown in Figure 3-2. Protons begin as H^- ions in the 50 MeV H^- LINAC. The electrons are stripped off by passing the protons through a thin aluminum foil, and the protons then move into the DESY III synchrotron and are accelerated to 7.5 GeV. The protons are then moved into the PETRA II ring and accelerated to 40 GeV before being transferred to HERA and accelerated to 820 GeV.

The electrons originate from a high voltage cathode and are accelerated to 500 MeV in the LINAC II before being accumulated into a bunch in the PIA storage ring. The bunches are then transferred into the DESY II synchrotron and are accelerated to 7 GeV before being transferred to PETRA II. This procedure is repeated until PETRA II is filled, then the electrons are accelerated to 14 GeV and are transferred to HERA where they are accelerated to 30 GeV (26.7 GeV for the 1993 running period).

The luminosity is an important parameter for any storage ring collider since it is the total number of expected interactions per unit time and per unit of cross section. The rate of observed events is then defined as $R = \mathcal{L}\sigma$. In terms of the beam parameters, the luminosity is defined as

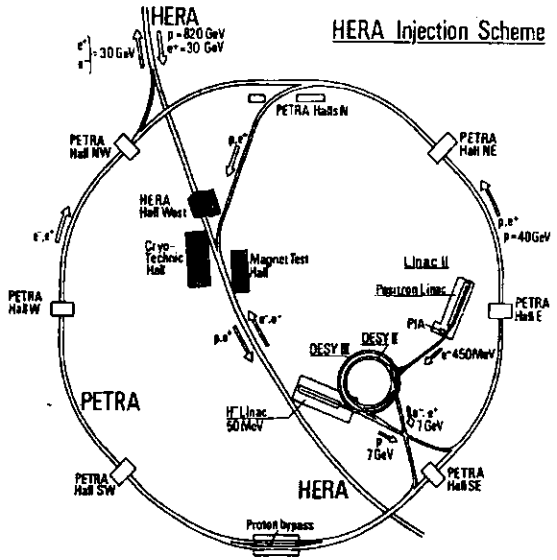

Figure 3-2 The HERA injection system

$$\mathcal{L} = \frac{f k N_e N_p}{2\pi \sqrt{\sigma_{x_e}^2 + \sigma_{x_p}^2}\sqrt{\sigma_{y_e}^2 + \sigma_{y_p}^2}}, \tag{3-1}$$

where f is the rotational frequency of HERA, f = 47.3 kHz, k is the number of colliding bunches, N_e and N_p are the number of electrons and protons in each bunch respectively, and σ_{i}^{j} is the rms transverse size of the beam of particles j in coordinate i. The highest average luminosity at HERA obtained during the 1993 run period was 1.5×10^{30} cm^{-2}s^{-1}, which is an order of magnitude below the design value. The total integrated luminosity collected over the 1993 run (luminosity integrated over time) reached 1 pb^{-1}.

3.2 The ZEUS detector

The ZEUS experiment was one of the two multi-purpose detectors operating at HERA during the 1993 run. A complete description of all the components of the ZEUS detector can be found in [26]. A general description of the detector as well as a more detailed description of the components used for this analysis is presented here.

An illustration of the ZEUS detector is shown in Figure 3-3. In the ZEUS coordinate sys-

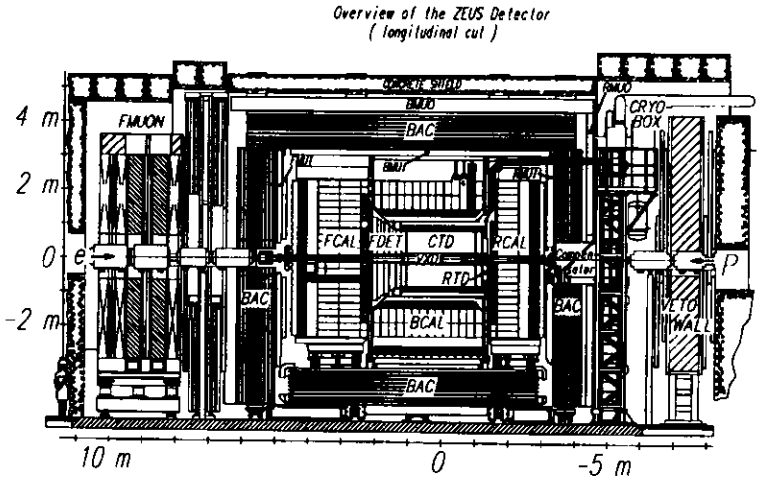

Figure 3-3 Cross section of the ZEUS detector along the beam axis
The cross section of the ZEUS detector parallel to the beam axis (z) is shown. The various components of the detector (see text) are labelled. The ZEUS coordinate system is as follows: +z follows the direction of the proton beam (from right to left), +y is in the upward direction, and +x points toward the center of the HERA ring, which is out of the page in the illustration.

tem, the z axis lies along the beam direction, with positive values in the direction of the proton (left in Figure 3-3). The positive y axis points up, and the positive x axis points towards the center of the accelerator, which is out of the page. Immediately surrounding the interaction point are inner tracking detectors comprised of a vertex detector (VXD), the central tracking detector (CTD), and planar drift chambers (FTD and RTD). Surrounding the CTD is a superconducting solenoid providing a 1.43 T axial magnetic field for measurement of charged particle momentum. A hermetic calorimeter comprised of forward (FCAL), barrel (BCAL), and rear (RCAL) sections is used to measure the energy of charged and neutral particles. An iron return yoke surrounds the calorimeter. The return yoke is also instrumented with limited streamer tubes to act as a backing calorimeter (BAC) to measure energy leaking from the main calorimeter. The iron yoke is also used for muon momentum determination. The yoke is magnetized to bend the path of muons passing through. Limited streamer tubes mounted on each side of the yoke in the barrel (BMUI, BMUO) and rear (RMUI, RMUO) are used to measure the momentum of muons. In the forward direction, limited streamer tubes mounted inside the yoke (FMUI) and drift chambers as well a streamer tubes located outside the yoke (FMUON) measure the momentum of muons in the toroidal magnetic field.

3.3 The calorimeter

3.3.1 Calorimetry

The objective of a calorimeter is to measure the total energy of particles. There are two general types of calorimeters to do this. The first type, known as homogeneous calorimeters, are made from materials which both absorb the energy of the particles and also produce a detectable signal which can be measured. A sampling calorimeter, on the other hand, uses a different material for the absorber and the sensitive volumes, hence the signal is collected from only part of the detector volume. One way this can be accomplished is by using alternating layers of absorber material to convert incoming particles into secondary particles (showering) and active material which detects the ionization energy of the secondary particles giving a visible (light) signal. The visible energy is then related to the total energy through a constant known as the sampling fraction, which is the fraction of visible energy over total energy and can be determined from test beams.

Calorimeters can also further be divided into two classes according to the type of particles observed. Electromagnetic calorimeters are used for observing electrons, positrons and photons. Electrons and positrons mainly lose energy by radiating photons through the bremsstrahlung process. Photons lose energy through pair production, the conversion of the photon into an electron--positron pair. These processes dominate down to energies of the order 10 MeV, below which scattering and ionization become the dominant processes for energy dissipation. The creation of many electromagnetic particles by an initial high energy electron or photon is known as an electromagnetic shower. The containment depth of an electromagnetic shower is expressed in units of a

parameter known as the radiation length (X_0), which is defined as the average distance in a material for the energy of an incident electron to fall to $1/e \approx 63\%$ of its energy,

$$X_0 \approx 180 \frac{A}{Z^2} \quad (\frac{g}{cm^2}), \tag{3-2}$$

where A is the atomic weight and Z is the atomic number. When expressed in units of X_0, the shower containment depth is found to be independent of material [27]. With the highest expected electromagnetic energies at HERA, 98% of the electron energy is contained within 25 X_0. The lateral spread of electromagnetic showers is contained at the 95% level within two Molière radii,

$$2\rho_m \approx 7 \frac{A}{Z} \quad (\frac{g}{cm^2}). \tag{3-3}$$

Hadronic calorimeters are designed for the more varied interactions of the hadrons, which includes the processes of the strong interaction. The interaction of the hadron in the material of the calorimeter can produce a variety of secondary particles including other hadrons, electrons, photons, muons and neutrinos. The secondary particles further interact according to type producing a hadronic shower with an obvious electromagnetic shower component from the electrons, photons and π^0s which decay to two photons. Hadronic showers suffer energy losses through the creation of minimum ionizing particles which exit the calorimeter after leaving only a small fraction of their total energy, through neutrinos escaping without depositing any energy, and through binding energy losses. Hadronic shower dimensions are typically given in units of interaction lengths,

$$\lambda \approx 35 \frac{A^{1/3}}{\rho}, \tag{3-4}$$

where ρ is the density of the calorimeter material. Approximately 95% of a hadronic shower is contained within a depth varying logarithmically with the energy and scaling with λ (~8λ for 800 GeV hadrons), and transversely within a radius of 1 λ.

3.3.2 Physical description

The ZEUS detector is of the sampling type described above. It uses stainless steel clad depleted uranium plates as the absorber material and plastic scintillator for the active material. The calorimeter was designed to be almost hermetic with 99.6% solid angle coverage with the missing 0.4% coming from the two beam pipe holes. It was also designed to be compensating, which means that the response to electromagnetic showers is the same as the response to hadronic showers, $e/h = 1$.

Mechanically, the calorimeter is divided into three components called the forward, barrel and rear calorimeters (F/B/RCAL respectively) covering polar angles of 2.2°–39.9°, 36.7°–129.1°

and 128.1°–176.5° respectively. Each of the calorimeter components is made up of modules, with 23 modules of various length in FCAL and RCAL, and 32 wedge shaped modules arranged in a cyclinder in BCAL with the cylinder axis along the beam direction. The modules are further divided into 20 x 20 cm^2 readout towers as illustrated in Figure 3-4 for an FCAL module. Each tower is sectioned longitudinally into an ~1λ electromagnetic (EMC) section and ~3λ hadronic (HAC) sections each with separate readout. The electromagnetic section is further divided into cells, with four 5 x 20 cm^2 EMC cells in each FCAL and BCAL tower, and due to the lower particle density only two 10 x 20 cm^2 EMC cells in each RCAL tower. Each cell is read out by two photomultiplier tubes, one on each side. Each HAC section is a single HAC cell read out by two photomultiplier tubes, with two HAC sections (HAC1, HAC2) in the FCAL and BCAL and a single HAC section in the RCAL.

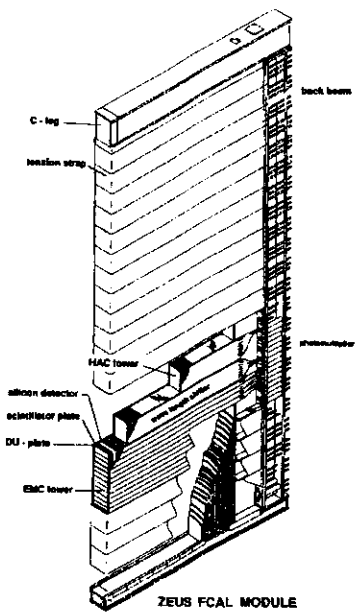

Figure 3-4 Layout of an FCAL module
Each module consisting of alternating layers of depleted uranium and plastic scintillator is partitioned into 20 x 20 cm^2 towers containing an EMC section and HAC sections. The light from the scintillator tiles is absorbed and re-emitted by the wavelength shifter along each of the sides, and is transported to photomultiplier tubes mounted at the base of each module.

The construction of one of the FCAL modules is shown in Figure 3-4. Each module is constructed from alternating layers of 3.3 mm thick depleted uranium plates clad in stainless steel, and 2.6 mm thick SCSN38 plastic scintillator for the active material. The stainless steel cladding around the depleted uranium plates reduces the noise from the natural radioactivity of the uranium to a level that can be used for calibration, and yet does not contribute significantly to a real signal. Wavelength shifters mounted along the sides of the modules absorb the light coming from the scintillator tiles and convert it to light with a longer wavelength. This light propagates along the wavelength shifters into light guides near the base of the module which directs the light into the photomultiplier tubes. Each cell of the tower has a wavelength shifter and photomultiplier tube mounted on each side.

The energy resolution of the calorimeter was measured in test beams to be $\sim 18\%/\sqrt{E}$ for electrons and $35\%/\sqrt{E}$ for hadrons, where E is expressed in GeV. The response was found to be linear within ±2% and to have a better than 1% uniformity between modules [28]. The calibration of the calorimeter and electronics is monitored constantly using the natural radioactivity of the uranium (UNO), charge injection into the electronics, laser light injection into the photomultiplier tubes, and ^{60}Co source scans of the modules.

3.4 The central tracking detector

The central tracking detector (CTD) is a cylindrical drift chamber surrounding the vertex detector and inside the main calorimeter described above. The CTD has a 16.2 cm inner radius, an 82.4 cm outer radius and measures 240 cm in total length. Charged track position and energy loss, dE/dx, are measured in nine concentric superlayers, consisting of cells containing 8 sense wires each. One octant of the CTD is shown in Figure 3-5. Three of the superlayers (1, 3 and 5) are instrumented with z by timing readout. The superlayers are also divided into axial (parallel to the length of the chamber) and stereo (at an angle of approximately of ±5°) layers to provide polar angle information.

The momentum of a charged particle is measured using the curvature of its path in the 1.4 T magnetic field provided by the thin, superconducting solenoid surrounding the CTD. The momentum resolution is given as a function of the transverse momentum (momentum orthogonal to the beam axis) by $\Delta p_T/p_T = 0.005p_T + 0.016$, and the hit position resolution is ~250 μm. The reconstructed tracks are projected back to the interaction point resulting in a vertex z position resolution of ~2 cm. The energy loss in the CTD, dE/dx, is used to perform particle identification.

3.5 The luminosity monitor

The luminosity monitor was designed, as the name suggests, to monitor the HERA luminosity by measuring the bremsstrahlung process of Section 2.6. The bremsstrahlung interaction is

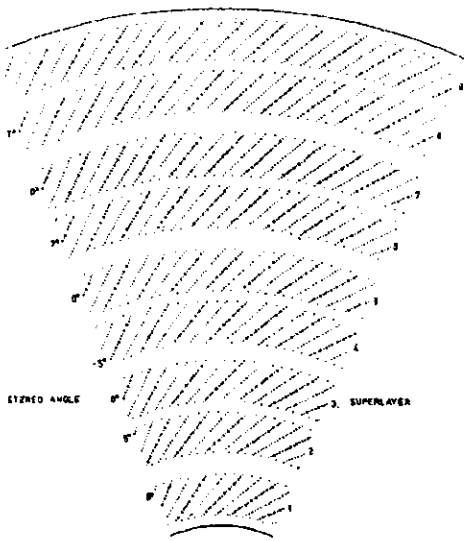

Figure 3-5 Layout of a CTD octant
The CTD is divided into nine superlayers, containing cells with 8 sense wires each. The stereo angles which allow for polar angle determination are also shown.

characterized by the emission of a low angle photon and a low angle electron. To detect these products, the luminosity monitor consists of two electromagnetic calorimeters, one positioned to measure the photon (LUMIG) and one to measure the electron (LUMIE). Both calorimeters are of the sampling variety, made of a lead-scintillator sandwich using 5.7 mm thick Pb absorber plates interleaved with 2.8 mm thick SCSN38 scintillator tiles for the active layers. LUMIG used plates and tiles with a transverse dimension 180 mm x 180 mm and has a total depth of 22 radiation lengths (X_0). The transverse dimensions for LUMIE are 250 mm x 250 mm and it is 24 X_0 deep. A position detector consisting of two orthogonal layers of scintillating fingers one cm wide and read out by silicon diodes is installed at 7 X_0 in each calorimeter, giving a spatial resolution of ~2 mm. Wavelength shifters are attached to opposite sides of the calorimeters (left and right for the electron detector, top and bottom for the photon detector). The light from the wavelength shifters is transported to the photomultiplier tubes through light guides. The energy resolution of both calorimeters was measured to be $18\%/\sqrt{E}$, with E in GeV, and with a 1% uniformity in the fiducial volume as well as a better than 1% response linearity [29]. Both calorimeters are mounted on movable tables so that they can be positioned away from the beam during injection and electron beam tests.

The arrangement of the two detectors in the HERA tunnel is shown in Figure 3-6. Photons originating from the IP under small angles ($\theta_\gamma \leq 0.5$ mrad) exit the proton beam pipe through a 0.1 X_0 window at $z = -92.5$ m. Protons undergo a vertical bend from dipole magnets placed at $z = -70$ m separating the photons from the proton beam line. After exiting the beam pipe, the photons pass through a 1 X_0 carbon absorber at $z = -103$ m and a 1 X_0 Pb absorber placed directly in front of LUMIG to minimize the effects of synchrotron radiation. The face of LUMIG is positioned at $z = -107$ m.

The acceptance of the electron detector is limited to electrons emerging from the IP with $\theta_{e'} \leq 6$ mrad and within an energy range of $0.2 \leq E_{e'}/E_e \leq 0.9$. Dipole magnets positioned at $z = -20$ m bend the electrons into the electron beam pipe. The lower energy scattered electrons are bent into a smaller orbit than the electron beam, and exit the electron beam pipe at $z = -27.3$ m. The scattered electrons then enter LUMIE positioned at $z = -35$ m. While the electron detector was not used for the luminosity measurement in 1993, it was very useful for tagging the low angle scattered

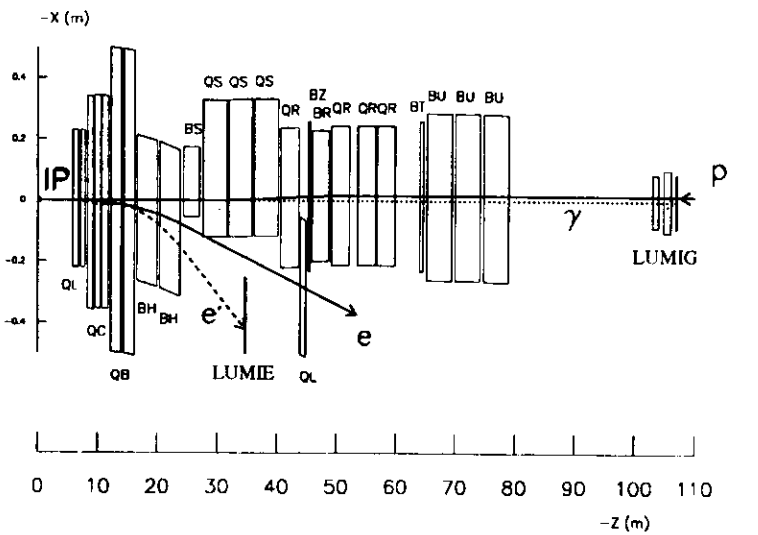

Figure 3-6 Layout of the luminosity monitor
The HERA beam tunnel in the electron direction (-z) including dipole magnets at ~20 m for bending the electrons into the electron beam pipe, and at ~50 m for moving the proton beam into head on collisions with the electrons. An electron calorimeter, LUMIE, is located at ~35 m for detecting scattered electrons. A photon detector, LUMIG, is placed at ~107 m in the proton direction to detect the scattered photons from bremsstrahlung interactions.

electrons from photoproduction events. The acceptance of LUMIE limited the kinematic range of the measured photoproduction scattered electrons to $0.1 \le y \le 0.8$ and $Q^2_{min} \le Q^2 \le 0.2$ GeV^2.

3.6 The C5

The C5 veto counter is made up of two pairs of U-shaped scintillator counters located at $z = -315$ cm surrounding the beam pipe. Each pair of scintillators is separated by 3 mm of lead. Each scintillator is read out by a photomultiplier tube. Additional lead sheets are placed in front of and behind C5 to protect the counters from synchrotron radiation. The counters are used to form a coincidence of energetic particles passing through the counters and the lead sheets. The C5 counters are used to measure the rate and time of interactions from the passing electron and proton beams, providing information on the bunch structure of the beams and the background rate.

3.7 The vetowall

The vetowall (VW) is designed to veto events coming from upstream interactions. It consists of an iron wall made up of iron bricks centered at $z = -727$ cm. The VW measures 800 cm in width, 900 cm in height, 87 cm in thickness and is positioned perpendicular to the beam axis. The beam pipe passes through an 80 cm x 80 cm hole near the center. The majority of particles that enter do not pass completely through the VW. Those that do continue into the central ZEUS detector.

Two planes of scintillator strips cover each side of the VW. Each scintillator counter measures 260 cm in length, 33 cm in width and 2 cm in thickness. A total of 48 counters cover each side of the VW. Each strip is read out by a light guide and two photomultiplier tubes, one at each end. A VW trigger occurs when there is a coincidence between corresponding counters on either side of the iron wall.

3.8 Central data acquisition

With the very small crossing time of 96 ns between bunches and the large estimated background rate of ~50 kHz at design luminosity, a three level trigger system with pipelined readout was necessary at ZEUS. The task of the trigger system was to reduce the total rate to ~5 Hz which could be written to mass storage tape. The majority of interactions come from background processes such as the interaction of the proton beam with the residual gas molecules in the beam pipe. Each level of trigger has more time to analyze each event and implement cuts designed to reduce these background processes. A layout of the ZEUS trigger system is shown in Figure 3-7. Each of the three trigger levels is discussed in more detail.

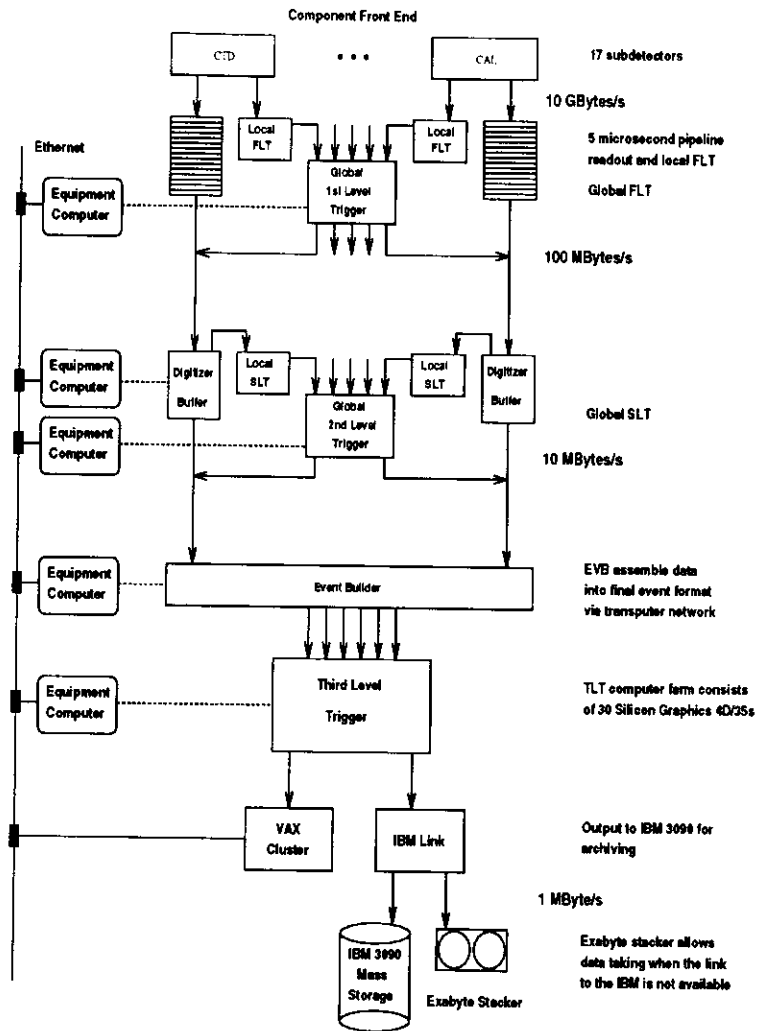

Figure 3-7 Schematic of the ZEUS CDAQ
Figure courtesy of Frank Chlebana [30].

3.8.1 First level trigger

The individual components involved in the First Level Trigger (FLT) cannot read out their electronics, make a local decision, and pass that decision to the Global First Level Trigger (GFLT) in the 96 ns between bunch crossings. This is due to the computation time needed to make a local trigger decision, and the time necessary for certain components to read out the signals (e.g., due to slow drift speeds in tracking chambers, hits may not be recorded for several crossings). For this reason, the event readout is stored in a FIFO[1] or pipeline which allows several events to be stored until a trigger decision can be reached. The GFLT requires that all local FLT components must evaluate their component data and send all results to the GFLT within 26 clock cycles[2]. The GFLT uses all the component data to arrive at a GFLT decision within another 20 clock cycles, giving a total of 46 clock cycles for a GFLT decision. The component pipelines store data for 58 clock cycles to allow for signal propagation delays.

Once a decision to accept an event is made, the GFLT signals all components. The components then read out the event from the pipeline, digitize any analog signals and write the events out to the component Second Level Trigger (SLT) buffers. During the digitizing of the analog signals, the component readout systems are inactive, resulting in deadtime. The FLT was designed to reduce the rate of events to the SLT to ~1 kHz.

This analysis makes use of certain Calorimeter First Level Trigger (CFLT) energy sums as well as the electron luminosity monitor energy sum (see Section 4.1.1). The CFLT quantities of interest are the REMC and the REMCTH energy sums. The REMC energy sum comprises the total energy in the RCAL EMC section of all cells, excluding the cells immediately surrounding the beam pipe, above an energy threshold of 464 MeV. The REMCTH trigger differed from the REMC trigger in that it also included the cells immediately surrounding the beam pipe and had a different cell threshold requirement.

3.8.2 Second level trigger

Events accepted by the FLT are passed to the component memory buffers of the Second Level Trigger (SLT). The job of the SLT is to reduce the data rate from the ~1 kHz input to 100 Hz output. This rate gives the SLT several milliseconds of processing time for each event. The component, or local, SLTs are based on a network of programmable transputers. With ~1 ms of processing time, much more complex algorithms may be implemented on the transputers to identify and eliminate background events such as spark rejection, cosmic muon rejection, and timing cuts. The processors can also perform iterative tasks such as CTD track segment identification and calorimeter cluster identification. The results of the local SLTs are combined in the Global Second

1. First In, First Out memory
2. One clock cycle is equivalent to one bunch crossing, or 96 ns.

Level Trigger (GSLT) which makes the final event decision. Once a decision to accept an event has been made, the event must be collected in a single memory location for access by the Third Level Trigger (TLT). All components pass their data to the Event Builder (EVB) for assembly of the full event.

3.8.3 Event builder

The Event Builder (EVB) collects all the component data after the SLT accepts an event and assembles the event in a single memory location accessible by the TLT. The EVB is also responsible for formatting the event in the ADAMO [32] structure that is used in the offline environment. Each component is read out by a two transputer (2TP) module connected to the EVB. The assembled event is made accessible to the TLT in one of six memory buffers in shared VMEbus crates. A 64x64 crossbar switch allows data from any component to be read out to any of the shared TLT memory buffers.

3.8.4 Third level trigger

The Third Level Trigger (TLT) is responsible for reducing the input rate from 100 Hz to ~5 Hz which is then output for offline analysis. Events are read from each of the six EVB VME crates by a branch of five analysis processors, giving a total of 30 processors for the 6 branches. The TLT utilizes the Silicon Graphics (SGI) 4D/35S 36 MHz RISC[1] based computers for analysis. This gives the TLT a total processing power of over 1000 MIPS[2]. Each branch is managed by an SGI 4D/25S RISC based computer which controls input and output functions as well as communication with the entire TLT system. Events accepted by the TLT are written out via an optical link to an IBM mainframe computer for mass storage, and a smaller sample of events is written to a central VAX for data quality monitoring.

3.8.4.1 Hardware

The hardware layout employed at the TLT is shown in Figure 3-8. As was mentioned, the EVB assembles the full events and writes them in ADAMO [32] structure to one of the 6 shared 512 kbyte triple-ported memory (TPM) buffers on the 2TP[3] modules [33] in the EVB VMEbus crates. A Fermilab Branchbus [34] is used to connect the EVB VME crates to the TLT system. Branchbus VMEbus Interface (BVI) cards [35] provide access to the VMEbus, hence the stored events, from devices on the Branchbus. Communication between analysis processors and manager processors is via an Ethernet segment.

1. Reduced Instruction Set Computer.
2. Million Instructions Per Second.
3. The 2TP is a two transputer module containing two INMOS T800 transputers connected via private ports to the TPM. The TPM has a third port connected to the VMEbus.

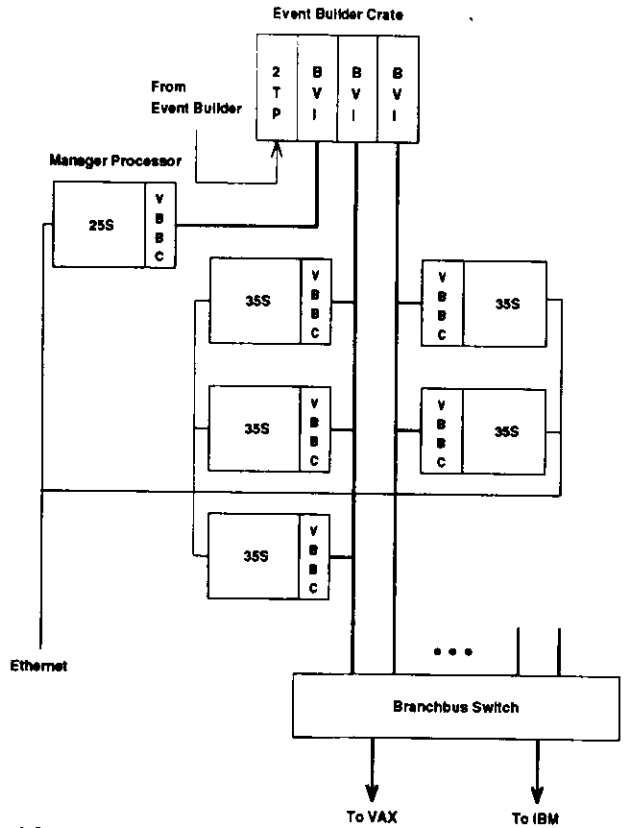

Figure 3-8 Schematic of the TLT hardware
The hardware associated with each branch of the TLT is shown. Included are Ethernet communication connections, as well as the Branchbus hardware and connections to the EVB VME crates and the analysis and manager processors. Each branch outputs events to the IBM and VAX through the Bus Switch.
Figure courtesy of Frédéric Bénard [31].

The TPM memory buffers are organized as logical ring buffers. The EVB writes events to the memory beginning at the lowest address. The first two words of the event are reserved for the event size and the status. The TLT begins reading from the buffer as soon as a full event is in place. When the EVB reaches the end of the buffer, it begins writing at the start, as the TLT has already read out the events at the beginning. Several words of memory in the buffer are reserved as status

words for communication between the EVB and the TLT. The words are used as pointers to the events in the memory, and are updated by the EVB when a new event is written to the memory, and by the TLT manager processors when an event has been read out from the memory. The analysis processors never change these status words.

Each EVB VME crate has a branch of processors for readout and analysis as well as a manager processor to monitor and update the communication status words. Each branch is split into two Branchbus segments which provide connections to the processors through a separate BVI. Each manager also has its own BVI for accessing the TPM. The manager processors continually monitor the status words in the EVB memory buffer. After the status has been updated by the EVB indicating a full event in memory, the manager processor selects one of the analysis processors to read out and analyze the event. Over the Ethernet, the manager processor gives the analysis processor the event location in the TPM to read out. The analysis processor may then retrieve the event and perform the TLT analysis (see Section 3.8.4.3 below).

The individual analysis processors initiate the transfer of the events from the TPM over the Branchbus with a VMEbus Branchbus Controller (VBBC) module [36] which is connected to the VME adaptor slot of the SGI processors. The event is read out of the TPM over the VMEbus and gets put onto the Branchbus by the BVI modules. The Branchbus is capable of transferring a sustained rate of 20 Mbytes/sec. However, the rate is limited by the output speed of the TPM onto the VMEbus (8 Mbytes/sec). Thus the maximum sustained rate out of the TPM onto the Branchbus is 8 Mbytes/sec. The VBBC reads the event from the Branchbus into the locked RAM of the 4D/35S analysis processor. Due to the nature of the programmed input/output (PIO) used by the VBBC to access the RAM of the analysis processor, the event rate is limited to 2.5 Mbytes/sec at this stage. This bottleneck is alleviated by the use of the two segment Branchbus design. While one of the analysis processor BVIs writes data stored in its 64 longword FIFO to the VBBC, the other BVI may access the TPM and the second segment can also transfer data. This allows for a potential 5 Mbytes/sec bandwidth per EVB crate, giving a total of 30 Mbytes/sec for all 6 crates.

Upon completion of event analysis, the analyzer processors must write out any good events for mass storage and for data monitoring. The TLT uses a Branchbus Switch (BS) [37] for writing to either the IBM mass storage tape facility or to a VAX for data monitoring. The BS consists of a 16 port crossbar backplane which permits up to 8 concurrent data paths, with each data path running at a maximum rate of 20 Mbytes/sec. Each Branchbus segment (two for each EVB crate) has a separate connection to the BS. The Branchbus is connected to the BS through Bus Switch Interface Boards (BSIB), and the BSIBs are given round robin arbitration for requests of data paths. Thus any analysis processor may request a data path through the BS to output an event to either the IBM or VAX.

As was mentioned above, the bottleneck for the event transfer was the rate of transfer from the VBBC into the main memory of the analysis processors using PIO. SGI in conjunction with the University of Toronto developed a VME extender (VDEXT) board [38] which was positioned in the VME adaptor slot of the analysis processors. The VBBC cards then plugged into the VDEXT card in this slot. The VDEXT could read data from the VBBC and write direct into the memory of the processor through direct memory access (DMA). This had the potential of increasing the transfer rate to the limiting factor of the TPM memory. However, cooling problems and data corruption prevented the use of the VDEXT in all but one branch. Upgrading the full system to use the VDEXT cards was deemed to be not worth the time and effort and development was stopped.

3.8.4.2 Control software

The TLT control software is based on the Cooperative Process Software (CPS) developed at Fermilab [39]. The operation of the TLT is divided between several running processes. The processes can all be run on the same computer for development work, or they can be run on different computers for online processing. An overview of the processes used is shown in Figure 3-9. The main control process, Control_TLT, is run on the TLT console in the ZEUS experiment hall, a 4D/35G dedicated to controlling and displaying TLT statistics. Control_TLT is responsible for communication with the ZEUS Run Control (RC) system which coordinates all the components of the experiment. It also gathers statistics from each branch and displays this information graphically.

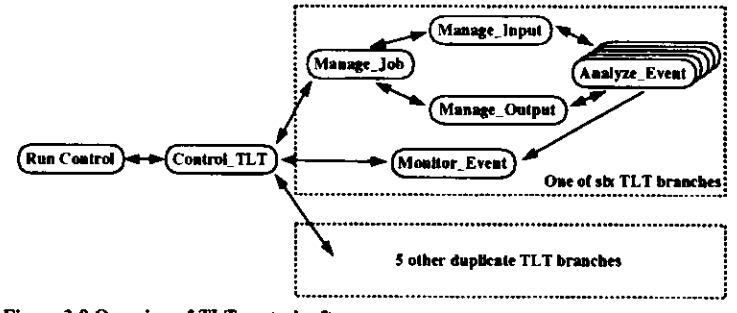

Figure 3-9 Overview of TLT control software
One branch of the TLT control software is shown. Communication with RC is managed by Control_TLT running on the TLT equipment computer. A copy of each manager process runs on each branch, as well as several copies of the analysis code, Analyze_Event. System performance data is collected by Monitor_Event and passed back to the TLT console.

Each of the TLT branches has the managing processes Manage_Job, Manage_Input, and Manage_Output running as well as Monitor_Event, the statistics and histogram gathering process. These processes all run on the manager computer, usually an SGI 4D/25S (see Figure 3-8). Each branch also has several copies of the analysis code, Analyze_Event, with one copy running on each of the analysis computers.

Manage_Job is responsible for allocating the hardware resources for the branch, as well as communicating with Control_TLT. It starts a copy of Analyze_Event on each of the processors attached to the branch. Analyze_Event is then responsible for applying all TLT rejection cuts and physics filters (see Section 3.8.4.3) to the event and either rejecting the event as coming from background, or writing out the event for further offline analysis. In order to be given an event for analysis, Analyze_Event sends a signal to Manage_Input that it is ready for an event, and is then placed in the Manage_Input wait queue. Manage_Input polls the TPM memory buffer in the EVB VME crate (see Section 3.8.4.1) via the BB. When an event is found, the address of the event is given to the first processor in the queue, which then fetches the event from the TPM memory, freeing the memory for further events from the EVB. Analyze_Event communicates with Monitor_Event, passing information about all events read in, the trigger decisions, physics filter decisions, and final trigger decision, including histograms of specific component values (e.g., total calorimeter energy). If Analyze_Event then makes a decision to accept the event, it places the event on the output queue by signalling Manage_Output. Manage_Output controls the output queues to the IBM and VAX and directs each processor when and where to write an event out.

3.8.4.3 Filter software

A two stage filter algorithm was designed and implemented for the 1993 run period as shown in Figure 3-10. Events coming into the TLT were first passed through a series of background rejection cuts to eliminate obvious background events. Physics filters were then applied to the remaining events with the aim of saving good physics events. In principle, all events which are not identified as background would be kept for further study. In practice, this would result in far too large an output rate from the TLT, hence specific events with a recognized signal were selected by the physics filters to reduce the rate of events out of the TLT to a manageable level. A log of the trigger performance was printed for each run, including the results of the TLT cuts and physics filters. An example from run 7430 is shown in Appendix A.

Events entering the TLT were sequentially subjected to background rejection cuts as shown in Figure 3-10. Any event which failed a rejection cut was immediately discarded, and no further processing was done on that event. Events were rejected on the basis of calorimeter sparks, calorimeter timing consistent with background events and inconsistent with physics events, and cosmic muons (see [40]). Further, a vertex requirement was flagged but not used for rejection. The vertex

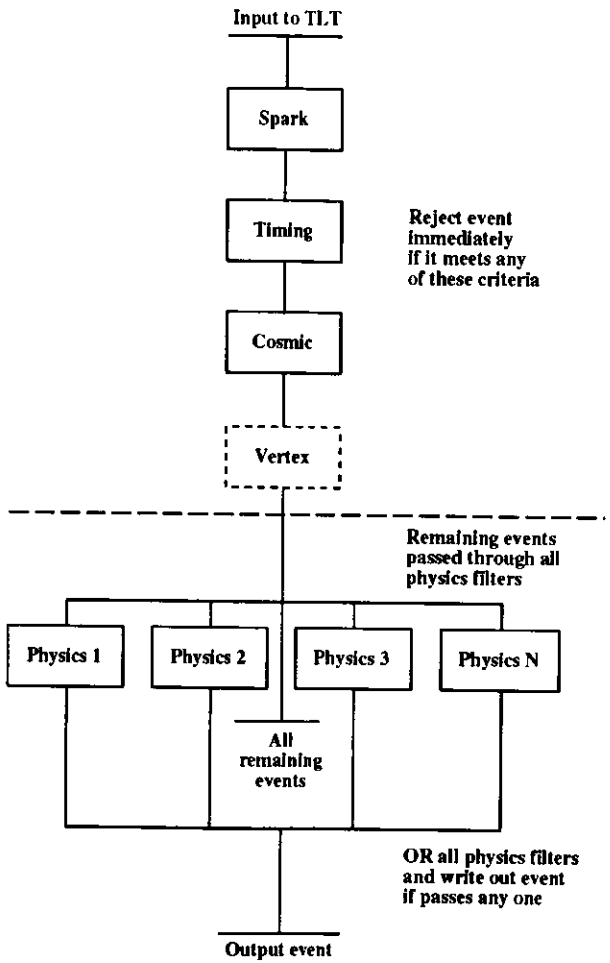

Figure 3-10 Overview of TLT filter software

reconstruction was based on the VCTRAK [41] reconstruction package. Events with a reconstructed vertex outside a preset region were flagged as coming from background. The events were flagged so that further study could be done and the cut implemented to reject events.

Any event which survived all the rejection cuts mentioned above was then passed through a series of filters, designed by the various physics groups at ZEUS, in order to select the desired physics signals. The various physics filters were designed to detect physics events of a given type by looking for a signal in the detector based on studies with Monte Carlo generated events. The filters could be very simple (i.e. $E_t > 10$ GeV) or very complicated, involving signals in several of the ZEUS detector components, including reconstructed tracks. A number of words was allocated in the output event for recording the results of the physics filters. If an event passed a given filter, the bit associated with that filter was set on (set to 1). In this way, easy offline selection of the events could be accomplished by checking for a specific bit in the trigger words. Events selected by the physics filters were also subjected to prescales to limit the output rate from the TLT. A second bit was allocated for each filter and turned on when an event first passed the filter itself, then also passed the prescale. Any events selected by a physics filter and surviving the prescale were written out to the IBM tape archive.

Events still remain which were not rejected by the background cuts, nor accepted by the physics filters. A small, random sample of these events was kept to study the type of events which remained, and the rest were discarded.

This two stage processing algorithm offers several advantages. First, events which are clearly background are eliminated immediately and no further processing time is wasted running, for example, the time consuming tracking package. Only events which pass the quick background cuts have the more time consuming algorithms run for selection of good physics. Also, specific types of physics can be selected and saved using the filters and the filter prescales. Filters can be easily changed or added as needed to search for a specific physics signal. The modular design of the filters also allows the search for several different physics signals. Events are passed through all filters, hence any given event may be tagged by several of the different filters.

4 Event Selection and Background Subtraction

The events used in this analysis were taken from August through November 1993. The integrated luminosity for this running period is shown in Figure 4-1 as a function of the ZEUS run number. A total of 383 nb^{-1} was collected by ZEUS during this time, excluding runs with detector component difficulties. Only 243 nb^{-1} are considered as good runs to be used for this analysis. Runs are rejected throughout the run period on the basis of total luminosity, beam tilt, and vertex shift (see Section 4.4).

The data processing for this analysis is divided into two separate parts – the online selection of events by the three levels of triggers, and the offline reduction of the event sample by further background subtraction and run selection.

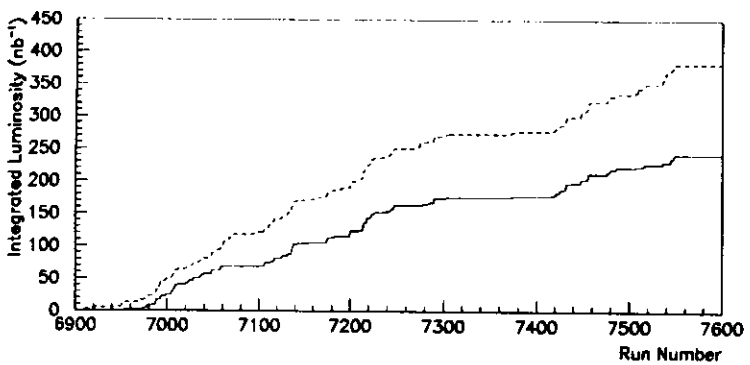

Figure 4-1 Integrated luminosity collected by ZEUS
The total integrated luminosity collected by ZEUS is shown as a function of the ZEUS run number. The dashed line shows all runs after run 6900, and the solid line represents only the runs used in this analysis.

4.1 Online selection

As described in Section 3.8, the online data acquisition system at ZEUS is divided into three levels of trigger selection. The events that pass the selection cuts at each of the trigger levels are then transferred and stored on an IBM mainframe computer. The aim of the online selection is to reduce the amount of data collected to a manageable size, while eliminating as many background events as possible.

In order to identify the soft photoproduction events, only the identification of the scattered electron by the LUMI electron detector is needed. This, however, suffers from high background due to bremsstrahlung events where the photon is not detected. In order to minimize this background, a tag of the hadronic system in the main calorimeter is also required.

4.1.1 First level trigger

Two separate first level trigger (*FLT*) trigger criteria are used to select the events for the photoproduction sample. Both of the triggers have a common requirement of a minimum of 5 GeV energy deposited in the LUMI electron detector, and both require that some energy be deposited in the rear (RCAL) EMC section of the main calorimeter. For triggering purposes the RCAL is divided into *trigger towers* of 20x20 cm^2, each tower consisting of two 10x20 cm^2 EMC cells, each cell is read out by two photomultiplier tubes [42],[43]. The trigger towers are summed over *trigger regions* (defined by the thick lines of Figure 4-2). If the trigger energy in a trigger region exceeds the set threshold value, the event is accepted. The two triggers used differ in the amount and location of energy required to trigger the RCAL as follows:

- The REMC trigger (TRemc) is a high resolution (8 bits of storage for the energy) trigger on the EMC energy of each tower, excluding the towers around the beampipe as shown in Figure 4-2 by the lighter grey region. The trigger is quantized with a resolution of 196 MeV, a starting energy of 464 MeV and a maximum energy of 50 GeV. The threshold for each trigger region is set at 464 MeV, the same as the lowest threshold for each individual trigger tower, thus a single trigger tower can trigger the event.
- The REMC threshold trigger (TRemcTh) is a low resolution (3 bits of storage for the energy) trigger with a logarithmic energy scaling which also includes the towers surrounding the beampipe. With only seven different values allowed by the 3 bit storage, the energy resolution is quite low and quantized in logarithmic steps (0 GeV, 0.625 GeV, 1.25 GeV, 2.5 GeV, 5.0 GeV, 10.0 GeV, 20.0 GeV, overflow). The threshold for the trigger regions is set at 1.25 GeV, requiring at least one tower of 1.25 GeV or above, or two or more towers of 0.625 GeV or above. The higher threshold (compared to the TRemc trigger) is required because of the amount of energy deposited in the inner ring of the RCAL by the background processes discussed later.

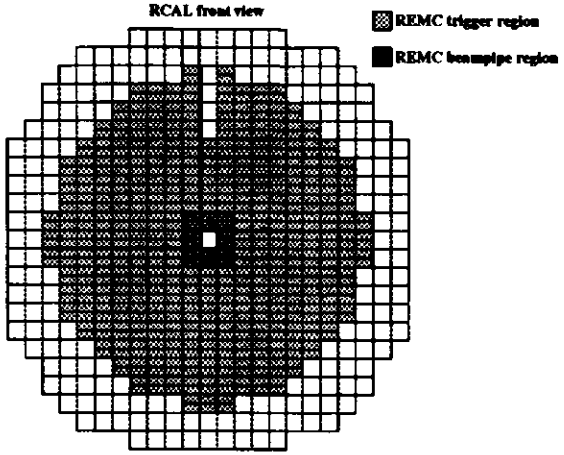

Figure 4-2 RCAL triggering layout
For triggering, the RCAL is segmented into 20x20 cm^2 trigger towers each containing two 10x20 cm^2 EMC cells. The trigger bits of all towers of a trigger region (thick solid lines) are summed, and the trigger regions are then summed and compared to the trigger threshold. The REMC beampipe region is only used for TRemcTh triggers.

4.1.2 Second level trigger

The second level trigger (SLT) rejected events from the first level trigger on the basis of timing criteria. All timing sums are made from the arrival time of energy deposits into the calorimeter photomultiplier tubes. The calorimeter allows very high precision (<1 ns) measurement of the arrival time of particles with energy ≈ 1 GeV [44]. By definition, particles from nominal interactions arrive at the face of each calorimeter at time t=0 ns from the interaction point. Provided that a large enough sum of energy is deposited, the SLT rejected events based on timing with a cut of $|T_{RCAL}| < 8$ns and $|T_{FCAL}| < 8$ns. This cut rejected all events which are more than 8 ns out of time with the arrival of particles into the photomultiplier tubes from the interaction point.

The SLT also rejected events based on the identification of calorimeter sparks, a discharge across the window of a photomultiplier tube. A spark will simulate a large energy deposit in the photomultiplier tube, and may cause the triggering of an event. The SLT spark algorithm was limited to identifying sparks in the BCAL section of the calorimeter, and thus did not affect the trigger for soft photoproduction events.

4.1.3 Third level trigger

As described in Section 3.8.4.3, the third level trigger (TLT) algorithms are divided into veto cuts and saving filters. Events are first rejected on the basis of calorimeter timing, muon rejection and spark identification. Various physics filters are then applied to save any remaining events.

Similar to the SLT spark algorithm, the TLT rejects events on the basis that a photomultiplier tube spark triggered the event rather than a real energy deposit. The TLT does not, however, limit its spark algorithm to the BCAL section of the calorimeter (although this is where the majority of spark events do in fact originate). The TLT spark rejection is based on the asymmetry, I_{cell}, and the total energy in the two photomultiplier tubes of the cell,

$$I_{cell} \equiv \left|\frac{L-R}{L+R}\right| > 0.9,\ E_{cell} \geq 1.5\ \text{GeV}, \tag{4-1}$$

where L, R are the energies from the left and right photomultiplier tube respectively. The event is labelled a spark if the energy remaining in the F/B/RCAL after the removal of the spark cell is less than 2.0 GeV (i.e., if after the removal of a spark candidate in the RCAL, the total RCAL energy is below 2.0 GeV, then the event is labelled as a spark and vetoed).

The TLT also employs two separate timing cuts: the *Straub* timing cut, so named for its originator, as well as the timing cut from the 1992 running period (hereafter known as the *old* timing cut). As shown in Figure 4-3a, for an *ep* interaction, the products travel from the interaction point and deposit energy in the F/RCAL at a time t≈0 ns by definition. If, on the other hand, the calorimeter is triggered by a background event (the background processes will be discussed in more detail in Section 4.3), remnants from the interaction may strike the calorimeter early by the

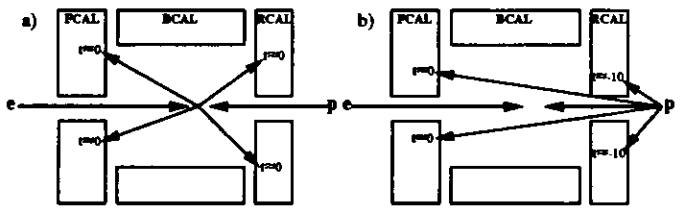

Figure 4-3 Calorimeter timing
The calorimeter timing for an ep interaction is shown in a). The e and p beams collide at the interaction point and the remnants arrive in the calorimeter at time t≈0 ns. A background interaction, as shown in b) may deposit energy in the calorimeter early, and may thus be rejected.

amount of time it would take to travel from the calorimeter to the interaction point and back as illustrated in Figure 4-3b. These events may be cut by an RCAL timing requirement, or the time difference between RCAL and FCAL.

The old timing cut, which is applied first, uses only the photomultiplier tubes from the cells around the F/RCAL beampipe[1] that have at least 1 GeV of energy deposited. If more than two such cells exist around the F/RCAL beampipe, then the average time of these cells is used. An event is classified as an *ep* event if $|T_{FCAL} - T_{RCAL}| \leq 4.5$ns and $|T_{RCAL}| \leq 4.5$ns. The event is classified as background if $|T_{FCAL} - T_{RCAL} - 10.5| \leq 4.5$ns and $|T_{RCAL} + 10.5| \leq 4.5$ns. If the event falls into neither the *ep* or background classifications, it is classified as unknown timing. Only events that are classified as background are rejected.

Any event which is not rejected by the old timing cut is then subjected to the Straub timing cut. For Straub timing, the energy weighted time average from all photomultiplier tubes in each calorimeter (F/B/RCAL) above a 200 MeV energy threshold and with a cell energy imbalance of less than 0.7 is calculated. An event is rejected if

$$|T_{RCAL}| > \max(8, 3\sigma_R) \text{ ns AND } T_{RCAL} \text{ well measured}, \tag{4-2}$$

OR

$$|T_{FCAL}| > \max(8, 3\sigma_F) \text{ ns AND } T_{FCAL} \text{ well measured}, \tag{4-3}$$

OR

$$|T_{FCAL} - T_{RCAL}| > \max(8, 3\sqrt{\sigma_F^2 + \sigma_R^2}) \text{ ns AND } T_{RCAL}, T_{FCAL} \text{ well measured}, \tag{4-4}$$

where σ_R, σ_F are the errors for the R/FCAL average times respectively defined below, and *well measured* means:

- Number of RCAL photomultiplier tubes must be greater than one, and the total RCAL energy from these photomultiplier tubes must be greater than 1 GeV.
- Number of FCAL photomultiplier tubes must be greater than one, and the total FCAL energy from these photomultiplier tubes must be greater than 2 GeV.

σ, the timing error for each photomultiplier tube, is calculated as follows:

$$\sigma = A_{ctyp} + \frac{B_{ctyp}}{E_{ctyp}^{PMT}}, \tag{4-5}$$

where the constants for each calorimeter section can be defined differently (*ctyp* can be FCAL HAC, FCAL EMC, etc.). The errors for the F/RCAL, σ_F and σ_R, are defined as

1. The inner ring of RCAL, shown as the dark grey region of Figure 4-2, or the inner two rings of FCAL

$$\sigma_{F/R} = \sqrt{\frac{1}{\sum_{F/RCAL} 1/\sigma}}. \tag{4-6}$$

Muon rejection at the TLT is done by a program called mutrig [40]. To summarize, mutrig identifies and eliminates cosmic and halo muons according to the following criteria:

- The calorimeter hits are consistent with a minimum ionizing particle.
- The calorimeter cell time - cell position correlation is consistent with a muon, i.e. the times from the struck calorimeter cells must be consistent with that of a particle traversing straight through the detector.
- The total transit time through the detector must correspond to that of a muon travelling straight through.
- Rough track reconstruction of the hits through the detector shows a straight line trajectory.
- 60% of all the calorimeter cells, as well as 60% of the total calorimeter energy above threshold, must belong to the possible muon track.
- For a halo muon, the outer vetowall must be hit.

The events passing the spark, timing and cosmic muon veto cuts described above also have to be saved by one of the physics filters in order to be written out to permanent storage. There are several triggers for soft photoproduction events, but only one is used for this analysis. It requires a coincidence of a minimum 5 GeV energy in the LUMI electron calorimeter, and a minimum 0.7 GeV of total energy in the RCAL.

4.2 Offline selection

All events that are accepted by TLT filters and that pass the TLT prescales (see Section 3.8.4.3) are then written to tape on an IBM mainframe computer. Over 10^6 events were written to tape for the 1993 run period, corresponding to about 600 nb^{-1} of integrated luminosity. These events are then read, processed, and written back to tape. This processing stage involves calibration of detectors as well as the identification of tracks in the CTD, condensates in the calorimeter and cosmic muon events. The resulting tapes of data are known as RDSTs (reduced data selection tapes).

During RDST processing, the soft photoproduction events are passed through a series of filters and flagged accordingly by *reconstruction bits*. These reconstruction bits allow fast and easy identification of different classes of soft photoproduction events at later stages of reconstruction and analysis. The following bits are used for this analysis:

- Nominal bit — this bit is set for all the LUMI tagged photoproduction events.
- Nominal, prescaled by 8 bit — this bit is identical to the nominal bit above, but only every eighth event is flagged, regardless of any other flags that may have been set.

- $\eta_{max} < 2$ bit — this bit is set if the event has the nominal bit set (see above) and the η_{max}[1] of the calorimeter condensates passes the cut.
- $P_z < 15$ GeV bit — this bit is set if the event has the nominal bit set and the total longitudinal momentum in the detector is less than 15 GeV.
- $E_t > 15$ GeV bit — this bit is set if the event has the nominal bit set and the total transverse energy in the detector is greater than 15 GeV.

A second processing is then applied to the RDST data. The aim of this pass of processing is the creation of data samples small enough that they can be stored on disk for fast access. To accomplish this, the RDST sample has to be reduced in size due to the limited amounts of disk space. The overall data reduction is accomplished as follows:

- All events from runs before run 6900 are rejected. Beam conditions were unstable before run 6900 (see Section 4.4.1).
- All events with the nominal prescaled by eight bit set are accepted.
- All events with either the $\eta_{max} < 2$ bit, the $P_z < 15$ GeV bit, or the $E_t > 15$ GeV bit set are accepted (these events will hereafter be known as *golden tag* events).

The resulting data set, all stored on disk, is known as miniDSTs. This is the data set used for this analysis, with a total integrated luminosity as shown in Figure 4-1 by the dashed curve. To compensate for the prescale applied to only part of the data sample, all data events are assigned a weight

$$w_{lumi} = \begin{cases} 1 & \text{if golden tag} \\ 8 & \text{otherwise} \end{cases} . \qquad (4\text{-}7)$$

The effect of the prescales on the shape of various calorimeter distributions is shown in Figure 4-4.

A check of the prescale itself can be done using the golden tag events. As mentioned above, all soft photoproduction events are also subjected to the nominal prescaled by eight tag as well, regardless of any other tags. Therefore, for each of the golden tagged samples, an eighth of the events should also have a prescale tag as well. As can be seen from Table 4-1 , within statistical errors, the ratio of total events to prescale tagged events for each of the golden tag samples is consistent with a prescale of eight, so the value of the prescale will be taken to be exact, and no error due to the prescale will be added to the event count uncertainty. The overall statistical error of the final data sample will of course be larger due to the lost statistics from prescaling the events.

1. η_{max} is the largest value of pseudorapidity of any calorimeter condensate with energy greater than 400 MeV, where pseudorapidity is defined as $-\ln(\tan(\theta/2))$.

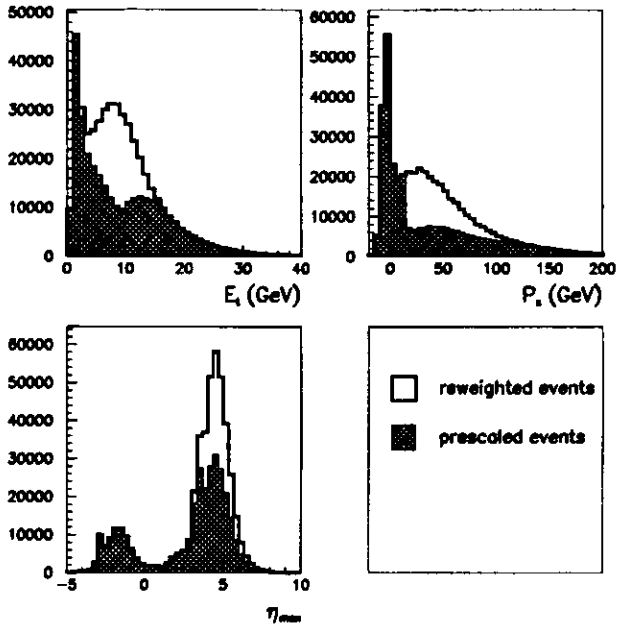

Figure 4-4 Effect of prescales on calorimeter distributions
The effect of the prescale correction weight are shown on the golden tagged distributions, E_t, P_z, and η_{max}. The events are plotted before the prescale correction weight is applied (hashed region) and after the weights have been applied (solid curve).

golden tag	total events	events prescaled	ratio
$\eta_{max}<2$	133261±365	16781±130	7.94±0.07
$P_z<15$ GeV	235060±485	29323±171	8.02±0.05
$E_t>15$ GeV	101885±319	12667±113	8.04±0.08

Table 4-1 Check of event prescale

As a recalibration of the detector is done during offline processing, it is possible that the energy sums calculated in the online environment are not the same as the offline results. Hence the offline energy thresholds are raised to ensure that no events are lost due to miscalibration effects. The offline cuts used are $E_{RCAL} > 1.0$ GeV , and LUMI electron energies in the range of 9.2 GeV

to 18.2 GeV, which can be compared to the online cuts from the previous section. The electron energy range allows for the division of the data into three bins in the photon-proton center of mass energy, $W_{\gamma p}$, as shown in Table 4-2.

$W_{\gamma p}$ (GeV)	LUMI electron energy range (GeV)
181	15.2 - 18.2
206	12.2 - 15.2
229	9.2 - 12.2

Table 4-2 Electron energy ranges for $W_{\gamma p}$ bins

4.2.1 Duplicate events

A search is done for duplicated events in the data sample. Duplicated events may occur in two ways: an entire event may be written out twice with the same run number and event number, or it is also possible that a duplicate has the event number changed. These duplicate events are searched for by comparison of different detector values for events within a range of ±100 events (i.e., LUMI electron energy, RCAL energy, FCAL energy, etc.). It is found that some events have the same run and event numbers, but are not duplicate events by the above criteria; these events are not counted as duplicates. A total of 11 duplicate events were found in the final sample, an effect of less than 0.01% and, therefore, is neglected.

4.3 Background subtraction

The photoproduction data sample is contaminated by various beam related background processes. Each of these processes can be further divided into a *tagged* and an *untagged* contribution to the process. Tagged background events are those that are easily identifiable from the photoproduction physics events (for example, events which occur in pilot bunches). The untagged events are those which are not easily separated from the physics sample as there are no clearly identifiable characteristics for the separation.

Since the tagged background events are identifiable from the physics events, they are quite easy to remove from the sample; however, this would leave the untagged background events in the sample without any handle for their extraction. This would then cause an appreciable uncertainty in the total number of good *ep* events in the final sample. Instead of removing the tagged events from the sample, they are allowed to remain in the sample and are used to remove the untagged events. If w is a known quantity, where w is

$$w = \frac{\#\ \text{untagged}}{\#\ \text{tagged}}, \tag{4-6}$$

then by applying the negative weight, $-w$, to the tagged events, the untagged events are removed statistically from the final sample (see [12] for a further description). Also, when plotting distributions, the tagged events are entered into the distribution with the negative weight, which effectively cancels the untagged events hidden in the *ep* events.

4.3.1 Electron gas background

Electron gas (*egas*) background occurs when one of the beam electrons interacts with a residual gas molecule or a structure inside the beampipe (such as a flange), with the electron continuing and becoming tagged in the LUMI electron calorimeter. Resulting hadrons from the interaction can be detected in the ZEUS main calorimeter, fulfilling the RCAL trigger requirement. The *ep* events can to a large extent be identified from the egas events by the z vertex position of the interaction. The egas events have a flat z vertex distribution, while the *ep* events are centered at the interaction point. Unfortunately, a z vertex cut alone will not eliminate all the egas events as some egas events do occur in proximity to the interaction point, and thus are indistinguishable from the desired *ep* interactions.

The electron pilot bunches (hereafter known as e-pilot bunches), as shown in Figure 4-5, provide a tagged sample of egas events, which are collected in the same manner as the *ep* events. The rate of egas events in any given bunch crossing is assumed to be proportional to the electron current of the bunch. On a run by run basis, the number of egas events hidden in the *ep* sample can be determined by scaling the sum of the e-pilot bunch currents to the sum of the electron *ep* bunch

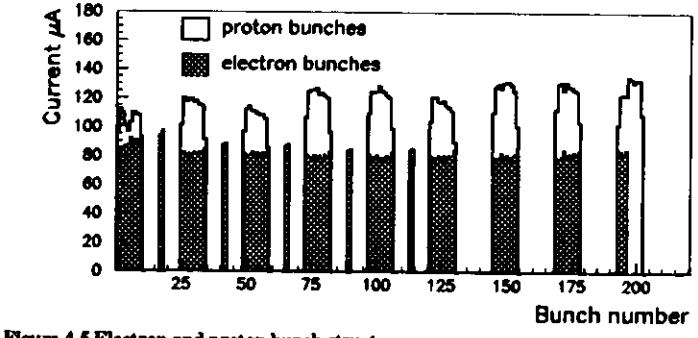

Figure 4-5 Electron and proton bunch structure
The average bunch current as a function of the HERA bunch number is shown for both electron and proton bunches. Certain electron bunches (bunch numbers 17-18, 41-42, 65-66, 89-90, 113-114) are unpaired with a proton bunch and are known as electron pilot bunches. Proton pilot bunches are also evident (bunch numbers 197-202).

currents (see Table 4-3). The egas events can be statistically subtracted by applying a weight

$$w_{egas} = \begin{cases} 1 \text{ for ep candidates} \\ -\dfrac{\sum I_e^{ep}}{\sum I_e^{pilot}} \text{ for e-pilot events} \end{cases} \quad (4\text{-}6)$$

	pilot bunches	colliding bunches	average pilot current (mA)	average colliding current (mA)	average correction weight
electron bunches	10	84	0.90	6.86	7.63
proton bunches	6	84	0.83	9.68	11.66

Table 4-3 Average electron and proton currents

to each event, where I_e^{ep} is the electron *ep* bunch current and I_e^{pilot} is the e-pilot bunch current of any bunch. The w_{egas} weight effectively eliminates all the egas background from the sample as well as corrects any distributions for the effect of the egas events.

The precision of the egas subtraction depends on the accuracy of the current measurement. As detailed in [45], it was found that there was an error of order 0.5% on w_{egas}. Evidence for this error came from studying the current normalized bremsstrahlung rate for each bunch. The first bunch of a consecutive group of bunches (*train* of bunches) had a lower bremsstrahlung rate. The effect seemed to be larger for smaller bunch trains, and significantly lowered the bremsstrahlung rate for pilot bunches, which consisted of a train of only two bunches.

The effect of the egas subtraction on the z vertex distribution of events which deposit less than 1 GeV of energy in the FCAL (these events are known as *diffractive-like*) is shown in Figure 4-6. These diffractive-like events are used since any egas events which deposit more than one GeV of energy in the FCAL are more likely to be vetoed by an FCAL timing cut (see the timing cut description in Section 4.1.3), hence the egas contamination will be much lower. The egas events are shifted towards FCAL as they are Lorentz boosted in the electron direction, and have a very small opening angle. The further from RCAL the events are produced, the more likely part of the hadronic system will enter and trigger in RCAL. As the vertex moves further from the interaction point, closer to the FCAL boundary, there is a higher chance that some remnant will also enter FCAL, and cause an FCAL timing veto, which causes the uncorrected distribution to fall off to-

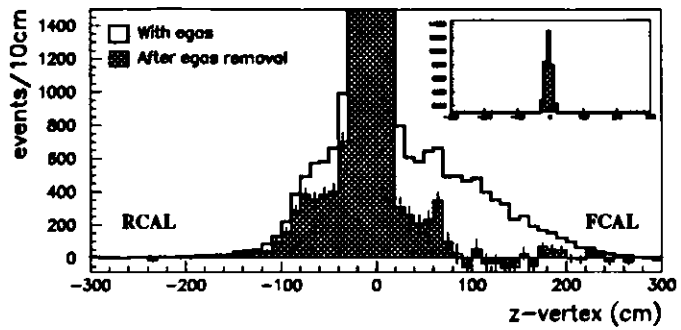

Figure 4-6 Egas background subtraction on z-vertex position of diffractive-like events
The z vertex of the diffractive-like events (E_{FCAL}<1 GeV) shows a large tail in the vertex position on the FCAL side. After egas subtraction, the tail becomes consistent with zero. The inset shows the full peak of the distribution.

wards FCAL. After egas subtraction, the forward tail of Figure 4-6 becomes consistent with zero as expected.

4.3.2 Proton gas background

Proton gas (*pgas*) background occurs when one of the beam protons interacts with a gas molecule or structure inside the beampipe. The remnant from the interaction then enters the main calorimeter causing an RCAL trigger. Since it is impossible for any remnant of the interaction to travel in the electron direction, traverse the complicated series of magnets, and trigger the LUMI electron detector, sufficient coincidental energy has to be deposited in the LUMI electron detector from, for example, a cosmic muon. Similar to egas events, the proton pilot bunches (see Figure 4-5 and Table 4-3) provide a sample of tagged pgas events which can be used for background subtraction. It is found, however, that no events are produced by the proton pilot bunches, which sets an upper limit on the pgas background of 0.01% and is neglected.

4.3.3 Coincidence background

As the name implies, coincidence background is the overlapping of two or more different background events in the same crossing. As was discussed with the pgas subtraction, it is almost impossible for a pgas event to trigger the LUMI electron calorimeter. However, it is possible to trigger the LUMI if the pgas event occurs in coincidence with a bremsstrahlung event. The coincidence background consists of a bremsstrahlung event which triggers the LUMI electron calorimeter and some event which deposits energy in the RCAL such as a cosmic muon or a pgas event.

These events are eliminated as much as possible with other cuts (e.g., timing cuts), but events remain in the final sample.

Similar to the egas background, the coincidence background also has a tagged component. If both the electron and the photon from the bremsstrahlung event are detected by the two LUMI detectors, then the summed energy of the two detectors should add up to the electron beam energy,

$$E_{LUMIE} + E_{LUMIG} \approx E_e \approx 26.67 \text{ GeV}. \tag{4-10}$$

The tagged coincidence events are used to statistically subtract the untagged events. Similar to egas and pgas events, the event weight, w_{coi}, is based upon the ratio of untagged events versus tagged events. The ratio is determined by looking at the LUMI *environmental records*. These records are taken in parallel to regular ZEUS data gathering and contain information for every bunch in the accelerator on the energies deposited in both LUMI calorimeters. Since the bremsstrahlung interaction is by far the most common, the environmental events basically contain an unbiased bremsstrahlung sample. Since the environmental events are taken separately from the regular ZEUS data acquisition chain, there is no requirement on the main calorimeter energy for these bremsstrahlung events. Figure 4-7 shows the spectrum for such events, with the tagged and untagged samples clearly identified. The ratio,

$$w_{coi} = \frac{\text{\# untagged bremsstrahlung events}}{\text{\# tagged bremsstrahlung events}}, \tag{4-11}$$

is obtained on a run by run basis by counting the number of events that are in the untagged region (denoted by the solid line in Figure 4-7) of the bremsstrahlung sample and the number of events in the tagged region (dashed region of Figure 4-7). Since the trigger for data gathering requires that energy be deposited in the LUMI electron calorimeter, the untagged background consists of events in which the photon escapes detection in the LUMI photon calorimeter, and thus cannot be distinguished from photoproduction *ep* events. The bremsstrahlung events in Figure 4-7a, where the electron escapes detection but the photon is detected (the events that lie along the y-axis), do not pass the LUMI electron detector trigger requirement and are not in the photoproduction data sample. The subtraction is applied to the data by identifying the bremsstrahlung events that fall into the tagged region of the photoproduction data sample, as shown in Figure 4-8 for run 7200, and applying the weight, w_{coi}, to these events. The effect of the coincidence subtraction can be seen from the z vertex spectrum of events with a vetowall hit as shown in Figure 4-9. As vetowall hits are the result of halo muons or pgas interactions with particles generated behind the RCAL, all the vetowall tagged events are coincidence events, and should be eliminated from the sample. After applying the coincidence subtraction, the vetowall sample becomes consistent with zero.

One obvious feature of Figure 4-7b is that the tagged and untagged electron energy spectra are not the same. The untagged spectrum peaks at a higher energy than the tagged spectrum, and

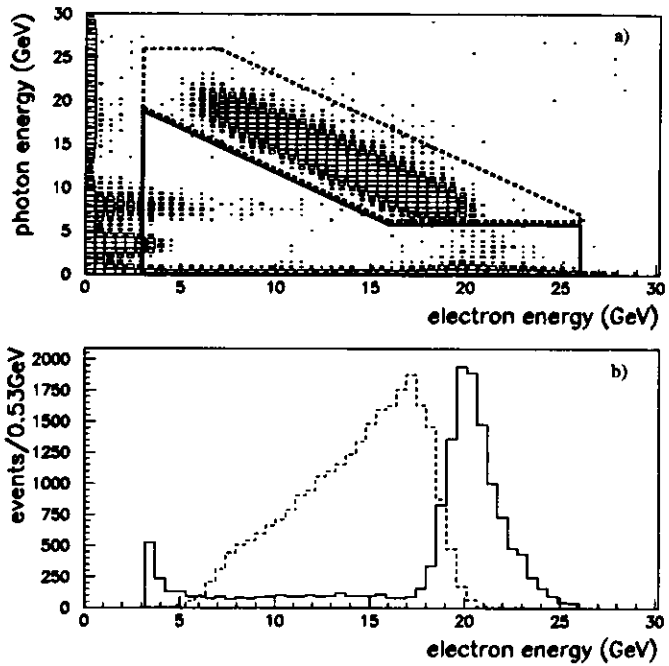

Figure 4-7 LUMI bremsstrahlung spectrum
The bremsstrahlung LUMI energy spectrum for run 7200 is shown in a) for both the electron and photon calorimeters. The regions of tagged events (dashed line) and untagged events (solid line) are also shown. Taking the ratio of the number of events in the untagged region versus the number of events in the tagged region gives the coincidence subtraction ratio. The projections of the tagged region (dashed) and the untagged region (solid) onto the electron energy axis is shown in b). The electron energy spectrum of the tagged region is very different from that of the untagged region.

has a long flat tail to lower energies while the tagged spectrum decreases slowly to lower energies. The coincidence background subtraction cannot be applied directly to the electron energy spectrum of the data as this would result in an unrealistic LUMI energy spectrum. Since the LUMI electron energy spectrum will be needed (see Section 6.3), a method of properly subtracting the coincidence background from the electron spectrum has to be developed. This is done by repositioning the electron energy of the tagged background events in the LUMI electron energy spectrum. To do this,

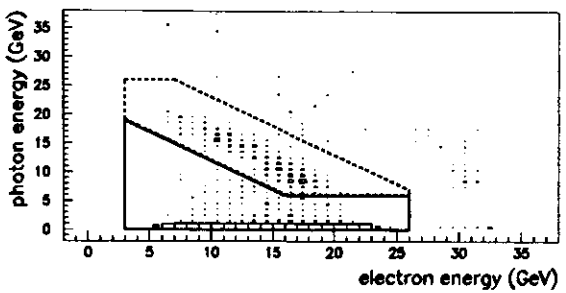

Figure 4-8 LUMI energy spectrum for run 7200
The LUMI energy spectra of data for run 7200 is shown. The tagged bremsstrahlung events are shown (dashed region) as well as the soft photoproduction candidates (solid region). The tagged background was used to statistically subtract the untagged background from the candidates.

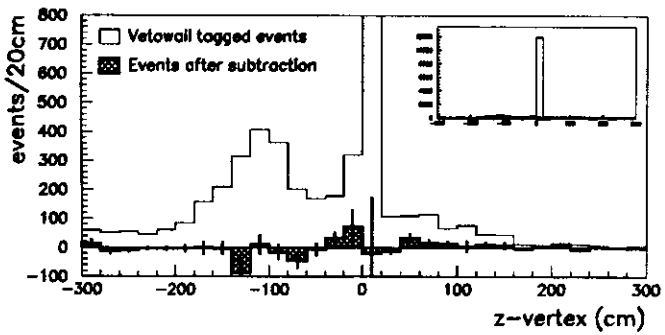

Figure 4-9 Effect of coincidence background subtraction
The spectrum of vetowall events before coincidence subtraction and after coincidence subtraction is shown. Before coincidence subtraction, there were a total of 15204.7 events in the vetowall tagged sample. After coincidence subtraction, the sample contained -8.6 events, consistent with zero within statistical errors. A horizontal fit to the subtracted sample (shown by the line at ≈ 0) resulted in an intercept of -0.13±0.80 with a χ^2 of 1.06, again consistent with zero. The full peak is shown in the inset.

the probability of an untagged bremsstrahlung event to be at any given energy is determined by renormalizing the untagged spectrum from Figure 4-7b to one. This probability spectrum is then integrated over all energies by summing the probability in each energy bin with the probabilities

from all lower energy bins, as shown in Figure 4-10 for run 7200. For each tagged coincidence event from the data spectrum (see Figure 4-8), the LUMI electron energy is randomly reassigned according to the integrated probability spectrum. For example, a tagged bremsstrahlung event from run 7200 with an electron energy of 16 GeV and a photon energy of 10.7 GeV has a random number of 0.65 generated for it. From Figure 4-10b, this places the new electron energy between 20-21 GeV. The event is then placed at a new energy, linearly interpolated between the two bins,

$$E_{LUMIE}^{new} = 20\text{GeV} + \frac{(R - P(20\text{GeV}))}{(P(21\text{GeV}) - P(20\text{GeV}))}, \quad (4\text{-}12)$$

where R is the random number generated, and $P(E)$ is the integrated probability of the energy, E. From Figure 4-10 $P(20\text{ GeV}) = 0.50$, and $P(21\text{ GeV}) = 0.73$, resulting in a new energy of $E_{LUMIE}^{new} = 20.64$ GeV.

Another feature of Figure 4-7a is that events in the untagged region can also have some photon energy. This will become important when a photon energy cut is applied to data to limit the effects of radiative corrections (see Section 6.4). Bremsstrahlung background events in the untagged region will be cut by a photon energy requirement, and this will change the background subtraction. From Figure 4-7 it is obvious that the photon energy spectrum for the tagged and untagged bremsstrahlung events are different. The photon energy for the tagged bremsstrahlung events has to be repositioned in the same fashion as the electron energy for the background subtraction to work with a photon energy cut.

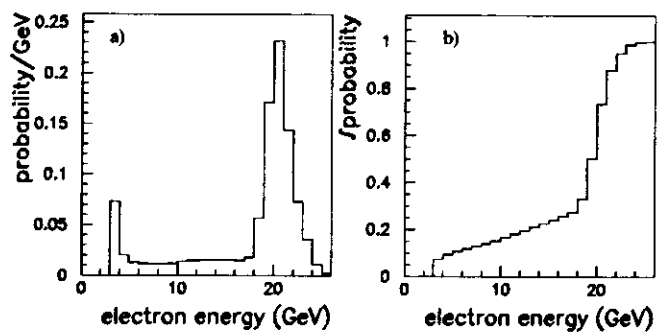

Figure 4-10 Probability spectra of run 7200 for untagged bremsstrahlung events
The probability as a function of the LUMI electron energy to obtain an untagged bremsstrahlung event at a given electron energy is shown in a) for run 7200. The probability spectrum of a) is then integrated and normalized as shown in b). The integrated spectrum of b) is used to assign new energy values to tagged bremsstrahlung background events.

The effects of the background subtraction on the LUMI electron and photon spectra are shown in Figure 4-11. The effect of the new electron energy for the tagged events on the spectrum can be seen from the high energy of the subtracted events. Likewise, the photon subtraction occurs predominantly at low energies.

The large tail of the photon spectrum is due to events that fall into neither the tagged bremsstrahlung region nor the photoproduction candidate region (the events above and to the right of these two areas in Figure 4-7 and Figure 4-8). Since these events do not fall into either class, they are given a coincidence subtraction weight, w_{coi}, of zero. As the energy sum of the electron and photon LUMI calorimeters for these events is far above beam energy, they must be the result of two overlapping bremsstrahlung events in the LUMI detectors. For the LUMI bremsstrahlung sample shown in Figure 4-7, all events with a combined LUMI electron and photon energy above

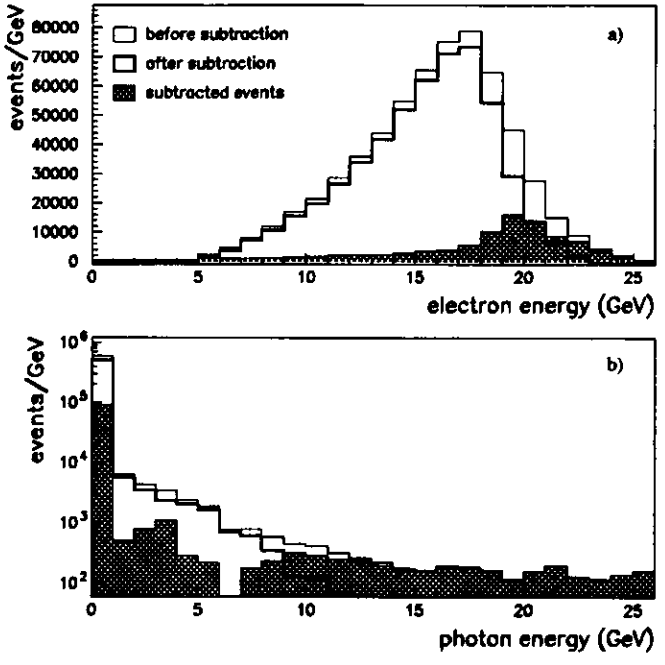

Figure 4-11 LUMI electron and photon spectra after background subtraction
The effects of the statistical background subtraction on a) the LUMI electron energy spectrum and b) the LUMI photon energy spectrum are shown as a function of the respective energy.

33 GeV (the upper boundary for the tagged region) are counted. The number of events above the 33 GeV line is found to be 1.0% of the number in the tagged region. This says that for the bremsstrahlung events, there is one double bremsstrahlung event for every 100 events in the tagged region. Doing a similar test with data reveals that the number of events with combined energy above 33 GeV is approximately 9.3% of the number of events in the tagged region. This excess indicates that most of these events must come from the accidental coincidence of a bremsstrahlung and an *ep* event. These good *ep* events are removed from the data sample ($w_{coi} = 0$), and therefore must be corrected for. After removal of double bremsstrahlung events from the data sample, it is found that the number of events above the 33GeV line is 0.7% of the number of total photoproduction events. The total number of events in each $W_{\gamma p}$ bin from Table 4-2 is corrected by 0.7%.

4.4 Run selection

Not all of the runs collected during the 1993 running period are used for this analysis. Many of the runs are unsuitable due to changes in the beam behavior. The LUMI electron calorimeter is very sensitive to any changes of the interacting electron beam, such as the tilt or horizontal position. Run selection cuts are made on the basis of horizontal vertex shift, total run luminosity and horizontal beam tilt at the interaction point as discussed below.

4.4.1 Vertex shift cut

As can be seen from Figure 4-12, the horizontal position of the interaction point changes at run 6935, and all runs before run 6935 are removed from the sample. The orbit change was caused by the HERA machine group changing the orbit of the two beams to optimize performance. Although only runs after run 6900 are shown in Figure 4-12, the horizontal spectrum for previous runs is similar to that of runs from 6900-6934. It will be shown in Section 6.3.3 that the LUMI electron acceptance depends strongly on the horizontal beam position at the interaction point, thus all runs before 6935 are excluded from the sample.

4.4.2 Run luminosity cut

All runs with a luminosity below 500 μb^{-1} are excluded from this analysis. This cut removes the smaller runs from the sample. For such runs, the error on the calibration of the LUMI detectors would be large. The smaller runs also incur a larger error for background subtraction due to the limited statistics.

4.4.3 Horizontal beam tilt cut

Only runs with a horizontal beam tilt of approximately -0.16 mrad are used in this analysis. When the electron beam passes the interaction point, it has a component of momentum in the hor-

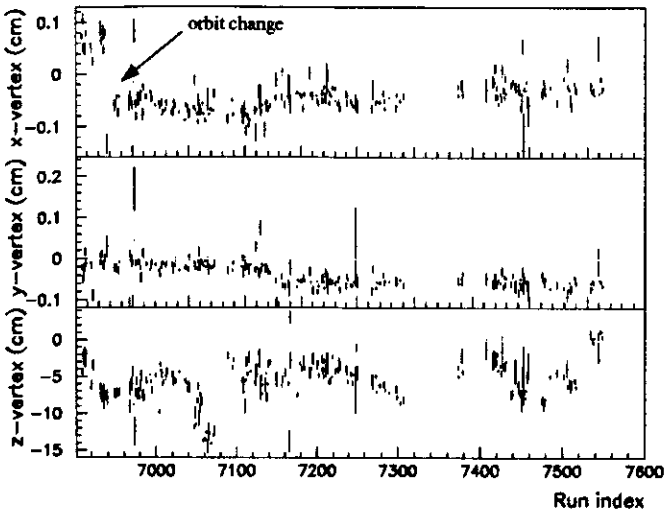

Figure 4-12 Average vertex position as a function of run number
The average x, y, and z-vertex position, as measured using the VC tracking package defined in Section 3.8.4.3, are shown as a function of the ZEUS run number. The change in the horizontal (x) vertex position at run 6935 is labelled. A much smaller shift of the horizontal and vertical (x,y) vertex positions at approximately run 7150 can also be seen.

izontal plane. The HERA machine group kept this tilt to (-0.15 ± 0.05) mrad for all runs. The beam tilt has a large effect on the acceptance of the electrons scattered into the LUMI electron calorimeter due to the series of magnets that must be traversed. Since the beam tilt does influence the electron acceptance, the run to run variation of tilts is kept small. The tilt can be monitored by the photons from bremsstrahlung events. As the photons are not affected by the magnets and travel straight from the interaction, the position obtained from the LUMI photon calorimeter can be used to determine the tilt of the electron beam as shown in Figure 4-13. A tilt of -0.16 mrad results in an x position of -1.712 cm in the photon detector 107 m downstream. The average beam tilt of the data is determined to be -0.16 mrad, thus a cut on the tilt for each run is made at -0.16 ± 0.03 mrad.

4.4.4 Final data sample

After applying the above cuts to the data, Table 4-4 shows the resulting final data sample for a LUMI photon cut of 5 GeV, 2 GeV, and without any photon energy cut (see Section 6.4). The total integrated luminosity of the surviving runs, the total number of remaining events and the total remaining runs are shown as the run selection cuts are sequentially applied. For the event count,

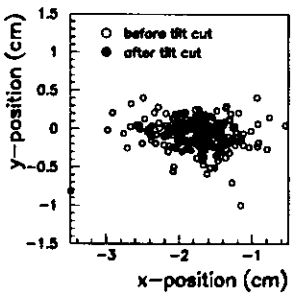

Figure 4-13 Average run position on face of LUMI photon calorimeter
The average x and y position on the face of the LUMI photon detector is shown for each run, as well as the runs accepted by a horizontal (x) beam tilt cut at -0.16 ± 0.03 mrad (1.7 ± 0.3 cm).

	E_{LUMIG} < 5 GeV				E_{LUMIG} < 2 GeV	no E_{LUMIG} cut
	no cuts	run ≥ 6935	Luminosity ≥ 500 μb^{-1}	Tilt ≈ -0.16 mrad	All cuts	All cuts
Luminosity (nb^{-1})	382.667 ±0.014	377.204 ±0.014	361.822 ±0.014	245.573 ±0.011	247.715 ±0.011	248.009 ±0.011
Events ($x10^3$)	513.4 ±1.7	507.8 ±1.7	487.4 ±1.6	332.0 ±1.3	329.6 ±1.3	337.0 ±1.3
Runs	231	219	144	90	88	92

Table 4-4 Effect of run cuts on data sample

background subtraction has been applied. The LUMI photon energy cut is applied to reduce the number of photoproduction events with initial or final state radiation, which also reduces migrations between $W_{\gamma p}$ bins. Table 4-4 shows that the tilt has the largest impact on the data sample. The luminosity cut has a large impact on the number of runs, but a much smaller impact on the total luminosity and the total number of events, as there were a large number of very short runs.

After all the run cuts have been applied, the effect of background subtraction on the final sample can now be assessed. For each $W_{\gamma p}$ bin from Table 4-2, Table 4-5 shows the effect of background subtraction on the total number of events, where BS in the table stands for bremsstrahlung events. The total subtracted background is shown as well as a breakdown of this background into the separate egas and coincidence components. The largest effect to the untagged sample comes from the electron gas subtraction.

$W_{\gamma p}$	181 GeV	206 GeV	229 GeV
Events without subtraction	138877	88051	44617
Events after subtraction	130961	84202	42162
Background events subtracted	7916	3849	2455
Egas pilot events	527	288	137
Egas equivalent in colliding bunches	3894	2128	1016
Tagged BS events in colliding bunches	2183	875	810
Tagged BS events in pilot bunches	9	4	4
Untagged BS events	1303	555	488

Table 4-5 Effect of background subtraction on $W_{\gamma p}$ bins

4.5 Events per Luminosity

The first step in calculating the cross section is to determine the number of photoproduction events produced for a given luminosity. This is done on a run by run basis by counting the total number of candidate events in each $W_{\gamma p}$ bin, and then dividing by the total luminosity of the run. The average value of the number of events divided by the total luminosity (denoted as $N/\mathcal{L}$) for all runs is given in Table 4-6. The effect of each run cut is also shown in the table, as well as the statistical uncertainty (upper error value) and the systematic uncertainties added in quadrature (lower error value) where applicable. The value of $N/\mathcal{L}$ as well as the χ^2 of the fit to all runs as shown graphically in Figure 4-14 is listed for each $W_{\gamma p}$ bin and for the different photon energy cuts. Included in the quantities are background subtraction and correction for double events.

Figure 4-14 shows the events per luminosity on a run by run basis. The x axis, labelled as run index, takes all the selected runs and renumbers them sequentially instead of using the ZEUS run number. Although the ZEUS run number information is lost, it is much easier to visualize the parameter changes. No large deviations from the average value of $N/\mathcal{L}$ for each bin are evident during the entire running period.

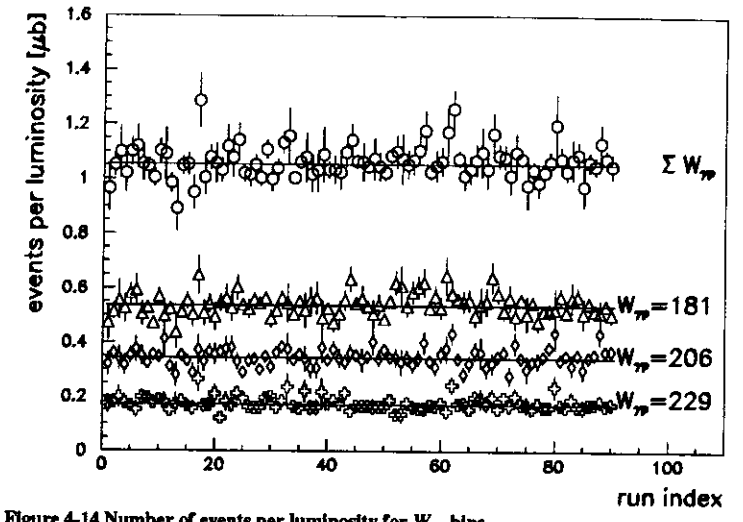

Figure 4-14 Number of events per luminosity for $W_{\gamma p}$ bins

The number of events per μb^{-1} of luminosity ($N/\mathcal{L}$) is shown for each of the $W_{\gamma p}$ bins as well as the sum of the three $W_{\gamma p}$ (denoted by $\Sigma W_{\gamma p}$). No large deviations are evident in any of the three bins. The fitted values for $N/\mathcal{L}$ and the χ^2 of each fit are given in Table 4-6.

Selection cut	$W_{\gamma p}$ = 181 GeV		$W_{\gamma p}$ = 206 GeV		$W_{\gamma p}$ = 229 GeV	
	$N/\mathcal{L}$(μb)	χ^2/ndf	$N/\mathcal{L}$(μb)	χ^2/ndf	$N/\mathcal{L}$(μb)	χ^2/ndf
No cuts	0.5336 ±0.0026	1.27	0.3383 ±0.0020	1.18	0.1622 ±0.0013	1.65
Run ≥ 6935	0.5361 ±0.0026	1.01	0.3392 ±0.0020	1.13	0.1623 ±0.0014	1.71
Luminosity ≥ 500 μb^{-1}	0.5373 ±0.0027	1.00	0.3407 ±0.0021	1.05	0.1645 ±0.0014	1.49
Tilt = -0.16 mrad	0.5352 ±0.0033 ±0.0039	1.04	0.3431 ±0.0025 ±0.0044	1.06	0.1699 ±0.0017 ±0.0065	0.98
systematics						
Luminosity ≥ 250 μb^{-1}	0.5353 ±0.0032	1.03	0.3429 ±0.0025	1.09	0.1699 ±0.0017	1.14
Luminosity ≥ 750 μb^{-1}	0.5352 ±0.0033	1.07	0.3428 ±0.0026	1.13	0.1702 ±0.0018	0.97
Tilt = -0.13 mrad	0.5313 ±0.0039	1.00	0.3427 ±0.0031	1.10	0.1705 ±0.0021	1.06
Tilt = -0.19 mrad	0.5351 ±0.0041	0.81	0.3387 ±0.0031	1.01	0.1634 ±0.0021	1.79
E_{LUMIG} < 2 GeV						
All cuts	0.5261 ±0.0032 ±0.0034	1.03	0.3369 ±0.0025 ±0.0038	1.09	0.1687 ±0.0017 ±0.0080	0.89
no E_{LUMIG} cut						
All cuts	0.5364 ±0.0032 ±0.0026	0.96	0.3461 ±0.0025 ±0.0040	1.09	0.1720 ±0.0017 ±0.0053	1.19

Table 4-6 Events per luminosity for $W_{\gamma p}$ bins

5 Calorimeter Acceptance

The main calorimeter of ZEUS is used to trigger on photoproduction events by requiring that energy be deposited in the RCAL section of the detector. The acceptance of the RCAL requirement of the trigger (A_{RCAL}) is determined by examining the fraction of generated Monte Carlo events which, after being passed through the full detector simulation, are accepted by the trigger simulation package. The relative fractions of the different contributing Monte Carlo subprocesses, as well as the subprocess acceptances, have to be determined before a final acceptance can be calculated. The contributions from the different Monte Carlo subprocesses are varied to achieve the best reproduction of the data.

5.1 Event Generation

Events for each physics subprocess are generated individually with various physics generators (which will be described along with the corresponding subprocess below) and combined into a final hadronic system, the calorimeter distributions of which are then compared to those of the data events. By minimizing the difference between the data and Monte Carlo for the calorimeter distributions, the best Monte Carlo description of the data can be obtained. The aim of the comparison is to determine the relative subprocess contributions, and hence acceptance contribution for each event type.

5.1.1 Diffractive processes

The technical description of diffractive subprocess generation is shown in Table 5-1 (see Section 2.3.1.1 and Section 2.3.1.2 for a description of diffractive processes). The PYTHIA [46] event generator is used to simulate the elastic photoproduction sample, as well as proton and photon inelastic diffractive processes. In all three cases, the photon produces a vector meson which then interacts diffractively with the proton. The Nikolaev-Zakharov (NikZak) [47] event generator is also used to generate photon diffractive events. In this generator, the photon is described by a quark-antiquark pair which couples to the proton through pomeron exchange. The NikZak generator only produces events for $M_X \geq 1.7$ GeV, where M_X is the mass of the diffractive state, so the lower M_X region is simulated with the PYTHIA photon diffractive events, and both Monte Carlos are mixed to give a smooth M_X spectrum down to $M_X = 1.2 - 1.5$ GeV. Double diffractive events

process	generator and description
elastic $\gamma^* p \to Vp$	PYTHIA $V = \rho, \omega, \phi$ with relative fractions 1/2.2 : 1/18.4 : 1/23.6 $d\sigma/dt \propto e^{Bt}$, where the slope of the t distribution is B = 11 GeV^{-2}
inelastic	$d^2\sigma/dtdM_X^2 \propto e^{Bt}/(M_X^2)^{\varepsilon}$, where the nuclear slope parameter is $B \approx 5$ GeV^{-2} $M_X^2 < 0.1 \cdot W_{\gamma p}^2$
proton diffractive $\gamma^* p \to VX_p$	PYTHIA $M_{X_p} > m_p + 0.2$ GeV
photon diffraction $\gamma^* p \to X_V p$	PYTHIA $M_{X_V} > m_V + 0.2$ GeV
	Nikolaev-Zakharov (NikZak) $M_{X_V} \geq 1.7$ GeV

Table 5-1 Diffractive generators

are included in the HERWIG non-diffractive event generator (see the next section) and are not added separately. All the simulated diffractive processes are then reweighted in M_X to produce Monte Carlo events with a cross section proportional to $(M_X^2)^{\varepsilon}$ (the M_X dependence on ε will be examined in Section 5.3) as shown in Table 5-1.

5.1.2 Non-diffractive processes

As shown in Table 5-2 the non-diffractive processes are generated using HERWIG 5.7 [48] in the minimum bias mode, which is based upon the minimum bias $p\bar{p}$ generator of the UA5 collaboration [49]. HERWIG generates an event by creation of clusters of $q\bar{q}$ pairs (or particles), one for each of the beam particles with additional clusters to account for the average charged particle multiplicity. The particle multiplicity is taken from a negative binomial distribution (NBD) tuned to the ZEUS data ([11] contains a detailed description of the tuning procedure and results of the analysis), and the particle p_t distribution is also fit to ZEUS data. The clusters are generated flat in

process	generator and description
minimum bias	HERWIG 5.7 $\langle p_t \rangle \approx 390$ MeV
hard direct and resolved	PYTHIA $p_t^{min} = 5$ GeV proton structure function MRSD- [50] photon structure function GRV [51]

Table 5-2 Non-diffractive generators

rapidity[1] and are allowed to decay, with the decay products striking the detector. Since it is very difficult experimentally to separate non-diffractive and double diffractive events, the UA5 parameterization is actually based on non-single diffractive events (NSD) which are a combination of double and non-diffractive events even though technically the generation process is a non-diffractive one. Therefore, no double diffractive component will be explicitly added to the Monte Carlo mixtures.

Hard direct and resolved events are generated separately using PYTHIA, and combined into a single hard subprocess component which is used in the fits to the data.

5.2 Hadronic System

As discussed in Section 4.1, an RCAL trigger is required to accept any event in the online data acquisition system. In order to determine the probability of events triggering the RCAL, a knowledge of the composition of the events is necessary first. Using Monte Carlo events passed through both the detector and trigger simulations, the acceptances of the generated subprocesses (see Section 5.1) are determined. The acceptance for each of the subprocesses, A_i, is calculated as follows:

$$A_i = \frac{N_i^{meas}}{N_i^{gen}}, \tag{5-1}$$

where, for each subprocess i, N_i^{gen} and N_i^{meas} represent the number of generated Monte Carlo events and the number of Monte Carlo events surviving online trigger and offline selection cuts. The overall calorimeter acceptance is then determined as

$$A_{tot} = \sum_i A_i \sigma_i \tag{5-2}$$

summed over all subprocesses, i, where σ_i is the relative subprocess contribution by cross section (i.e., the relative fraction of each subprocess at the generator level) and $\sum_i \sigma_i = 1$.

If all subprocesses had very similar acceptances, the overall acceptance would not depend on the relative fraction of each subprocess and the composition of the sample would not matter. However, as shown in Table 5-3, the subprocess acceptances vary a great deal, with the elastic and proton diffractive contributions having by far the smallest subprocess acceptances. A detailed knowledge of the composition of the final Monte Carlo event sample (the σ_i for each of the subprocesses) is thus required to determine the calorimeter acceptance, A_{tot}.

1. Rapidity is defined as $y = \frac{1}{2}\ln\left(\frac{E+P_z}{E-P_z}\right) = \tanh^{-1}\left(\frac{P_z}{E}\right)$.

Subprocess	Acceptance (%)		
	$W_{\gamma p}$ = 181 GeV	$W_{\gamma p}$ = 206 GeV	$W_{\gamma p}$ = 229 GeV
PYTHIA elastic	30.1 ± 1.2	21.1 ± 1.2	13.1 ± 1.2
PYTHIA proton diffractive	39.6 ± 1.4	29.2 ± 1.4	21.2 ± 1.3
PYTHIA photon diffractive	75.9 ± 1.6	75.5 ± 1.5	76.0 ± 1.5
PYTHIA double diffractive	79.1 ± 1.6	78.6 ± 1.6	78.1 ± 1.6
NikZak photon diffractive	84.15 ± 0.77	86.43 ± 0.68	88.0 ± 1.5
Photon diffractive mixture	83.76 ± 0.86	85.05 ± 0.78	87.0 ± 1.4
HERWIG minimum bias (minb)	87.1 ± 1.8	89.8 ± 2.4	90.7 ± 2.5
Hard mixture	72.5 ± 1.9	85.6 ± 2.3	91.8 ± 2.5

Table 5-3 Monte Carlo subprocess acceptances

The fractions obtained from fits of the Monte Carlo subprocesses to data are not the relative cross section fractions, σ_i, discussed above, but instead the relative measured fractions,

$$f_i = \sigma_i A_i, \tag{5-3}$$

which are normalized such that

$$\sum_i f_i = 1. \tag{5-4}$$

The measured subprocess fractions, f_i, can then be related to the generated subprocess fractions, σ_i, using Eqn. (5-3) and remembering that $\sum_i \sigma_i = 1$,

$$\sigma_i = \frac{f_i/A_i}{\sum_j f_j/A_j} \tag{5-5}$$

which, by Eqn. (5-2), gives

$$A_{tot} = \frac{\sum_i f_i}{\sum_j f_j/A_j} \tag{5-6}$$

and by using Eqn. (5-4), we find that

$$A_{tot} = \frac{1}{\sum_j f_j/A_j}. \tag{5-7}$$

To determine the measured subprocess fractions, f_i, the Monte Carlo subprocesses are combined and compared to data using different calorimeter distributions (e.g., total calorimeter energy, E_{tot}). The subprocess fractions are varied to minimize the χ^2 between the Monte Carlo mixture and the corresponding data distribution, with the chi squared per degree of freedom, χ^2/ndf, calculated as follows:

$$\frac{\chi^2}{ndf} = \frac{1}{bins - 1} \cdot \sum_{j=1}^{bins} \frac{(N_j^{data} - N_j^{MC})^2}{(\sigma_j^{data})^2 + (\sigma_j^{MC})^2}. \tag{5-8}$$

N_j^{data} and N_j^{MC} are the number of data and mixed Monte Carlo events in bin j of the distribution respectively, σ_j^{data} and σ_j^{MC} are the statistical errors for bin j, and the sum is taken over all bins of the distribution. All the distributions are normalized such that the measured sum is one (i.e., $\sum N_j^{data} = \sum N_j^{MC} = 1$). The χ^2/ndf allows the determination of the best Monte Carlo description that is compatible to each of the data distribution.

In order to resolve the subprocess fractions, the distributions chosen must provide some separation of the different components. Ideally, the RCAL energy distribution would be used, as the trigger only requires that energy be deposited in the RCAL section of the detector. It is found however, that all the subprocesses have similar RCAL energy distributions, thus no separation is possible and it is not used. For this analysis, the following four calorimeter distributions, derived from condensates[1] above 160 MeV except as noted, are used:

- Total calorimeter energy, E_{tot} – the sum of the total energy of all calorimeter condensates.
- Total transverse energy, E_t – the sum of the transverse energy of all calorimeter condensates.
- Condensate multiplicity, n_{cond} – the total number of condensates in each event.
- Largest pseudorapidity[2], η_{max} – the most forward calorimeter condensate with energy above 400 MeV.

While there is some correlation between the distributions (e.g., higher energy events are more likely to have higher E_t as well as a higher condensate multiplicity, and a larger η_{max}), all the distributions are distinctive and an average of the acceptances determined from a fit to each of the four distributions will be used. An example of the fits to these data distributions is shown in Figure 5-1. The fits themselves will be discussed in more detail in later sections.

1. A calorimeter condensate is a group of adjacent calorimeter cells with energy deposit above the noise threshold of 60 MeV for EMC cells and 100 MeV for HAC cells.
2. Pseudorapidity is defined as $-\ln(\tan(\theta/2))$ for each calorimeter condensate.

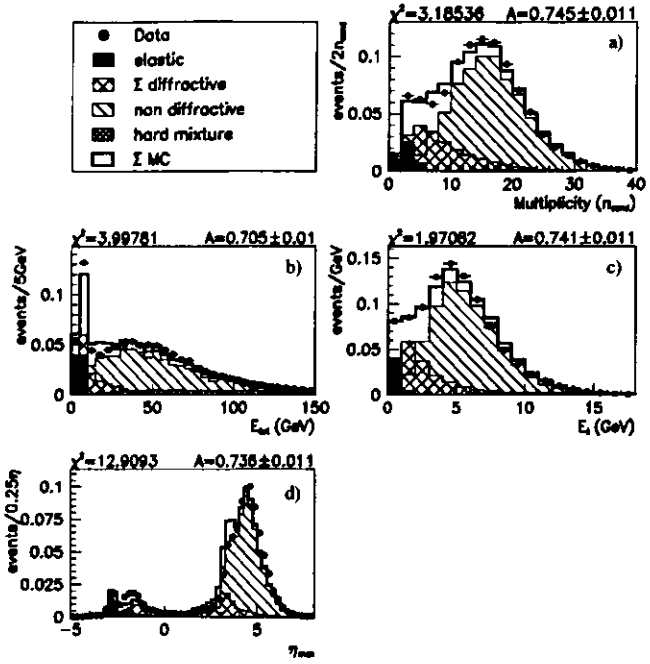

Figure 5-1 Monte Carlo fits to data for four different calorimeter distributions
The best Monte Carlo fits to various data distributions are shown, along with the χ^2/ndf, labelled as χ^2, and acceptance resulting from the fit. The error on the acceptance is statistical only, due to the finite number of events in each Monte Carlo subprocess. The distributions shown are for $W_{\gamma p}$ = 181 GeV, and ε = 1 (see Section 5.3 for a description of ε), assuming that proton diffractive and photon diffractive events are mixed 1:1 by cross section. All distributions are normalized to one event.

5.2.1 Dead material

There is a problem with the Monte Carlo description of the detector since it does not accurately describe all of the *dead material*[1] in the detector. This is most pronounced in the rear direction, affecting the simulation of RCAL energies, allowing more RCAL energy to be deposited in the Monte Carlo than occurs in data. This will have a larger effect on the subprocesses which deposit little energy in the FCAL and BCAL sections of the calorimeter, such as elastic events, shown

1. Inactive material inside the detector (such as support structures) that may cause a particle to lose energy if traversed.

in Figure 2-3a, and photon diffractive events, shown in Figure 2-3b. The effect of the dead material on the four select fit distributions is assumed to be small and should be within the rather larger errors determined for the calorimeter acceptance (see Section 5.6 for a summary of the errors associated with the calorimeter acceptance).

5.2.2 Calorimeter acceptance

Similar to the 1992 analysis [52], the fits are simplified by assuming $\sigma_{YX} = \sigma_{Xp} = 2\sigma_{XX}$ (see Section 2.3.1.2) for the inelastic diffractive cross sections [6]. As was discussed in Section 5.1.2, the double diffractive events (σ_{XX}) are implicitly included with the generated non-diffractive events, so only the proton and photon diffractive processes are mixed with equal cross sections, labelled as "Σ diffractive" in Figure 5-1. Table 5-4 summarizes the acceptances (including the averaged acceptance) for the fitted distributions, assuming the standard diffractive dependence of $d\sigma/dM_X \propto 1/M_X^2$ where M_X is the mass of the diffractive system. The diffractive mass is calculated as the square root of the difference of the energy squared and the momentum squared, $M_X = \sqrt{E^2 - p^2} \sim \sqrt{E^2 - p_z^2} \sim \sqrt{2E_\gamma(E + p_z)}$ where E and p are obtained from the calorimeter and E_γ from LUMIE.

The best fit for each of the four distributions is shown in Table 5-4 for each of the $W_{\gamma p}$ bins defined in the previous chapter. For each distribution, the total acceptance is given as calculated from the fit values of σ_i for each of the subprocesses, which are given under each of the subprocess labels in the table. The label *minb* refers to the HERWIG NSD events described in Section 5.1.2 and the label *hard* refers to the combined direct and resolved events also described in Section 5.1.2. The uncertainties on the individual distribution acceptances in Table 5-4 are only due to the event statistics. The acceptances from the individual distributions are averaged to get the final calorimeter acceptance with the statistical error taken from the spread of the values. The acceptances for each bin are equivalent within statistical errors. Also shown in Table 5-4, the χ^2/ndf for the fits can be quite large (12.9 in the case of η_{max} for $W_{\gamma p}$ = 181 GeV). Excellent agreement between the data and the Monte Carlo is not expected until further study of γp interactions and tuning of the Monte Carlos is done. The rather large χ^2/ndf of the η_{max} distribution will be discussed in more detail in the next section.

From Table 5-4, certain trends can be seen. First, the fraction of the non-diffractive (labelled as minb in the table) and the hard events vary by a large amount from fit to fit, while the sum of the two process (labelled as *minb* + *hard* in the table) has only a small variation. The variation of the non-diffractive and hard events only affects the acceptance of the $W_{\gamma p}$ = 181 GeV bin, where the acceptance of the two components are not approximately the same (see Table 5-3). This accounts for the low acceptance of the E_{tot} distribution in this bin, as the E_{tot} distributions requires a much larger fraction of hard events than any of the other distributions. Also of note in the table is

distribution	Acceptance (%)	$\frac{\chi^2}{ndf}$	Subprocess contribution (σ_i in %)					
			elastic	minb	hard	minb + hard	proton diff.	photon diff.
$W_{\gamma p}$ = 181 GeV								
E_{tot}	70.5 ± 1.0	4.00	18.42	52.79	11.62	64.41	8.59	8.59
E_t	74.2 ± 1.1	1.97	11.35	61.95	2.90	64.86	11.90	11.90
η_{max}	73.6 ± 1.2	12.91	13.10	63.32	0.00	63.32	11.79	11.79
n_{cond}	74.6 ± 1.2	3.19	10.73	63.59	1.25	64.84	12.22	12.22
average	73.2 ± 1.6		13.40	60.41	3.94	64.35	11.12	11.12
$W_{\gamma p}$ = 206 GeV								
E_{tot}	71.7 ± 1.2	3.13	13.47	44.07	17.69	61.76	12.39	12.39
E_t	73.0 ± 1.5	0.95	12.84	59.24	3.87	63.11	12.03	12.03
η_{max}	71.7 ± 1.5	6.49	15.30	61.41	0.00	61.41	11.64	11.64
n_{cond}	73.3 ± 1.4	3.75	11.37	57.40	5.44	62.84	12.90	12.90
average	72.4 ± 0.7		13.24	55.53	6.75	62.28	12.24	12.24
$W_{\gamma p}$ = 229 GeV								
E_{tot}	74.0 ± 1.2	2.13	8.22	42.94	20.04	62.98	14.40	14.40
E_t	71.4 ± 1.4	1.77	12.29	55.82	4.95	60.77	13.47	13.47
η_{max}	68.6 ± 1.6	4.89	19.06	60.82	0.00	60.82	10.06	10.06
n_{cond}	71.1 ± 1.4	2.92	12.56	53.48	6.85	60.33	13.55	13.55
average	71.3 ± 1.9		13.03	53.27	7.96	61.23	12.87	12.87

Table 5-4 Acceptances and fitted cross sections for calorimeter distributions

that the elastic fraction (the column labelled *elastic* in the table) has the largest variation if only the *minb* + *hard* is considered instead of the individual *minb* and *hard* components. The variation is largest in the $W_{\gamma p}$ = 229 GeV bin (this will become even more evident in Section 5.4). This is due to the very low acceptance for elastic events in this bin as seen from Table 5-3. Not many elastic events survive, and the small number of events makes the fit less accurate.

5.3 M_X dependence

While the gross features of the calorimeter distributions can be reproduced by the Monte Carlos, certain discrepancies are evident. Particularly, the data peak at $\eta_{max} = -1.5$ of Figure 5-1d is far larger than the corresponding Monte Carlo peak. This Monte Carlo deficit has the effect of increasing the calculated χ^2 between the data and the Monte Carlo mixture giving values much larger than the other distributions. This peak can be seen to consist mostly of diffractive events (in particular, low mass photon diffractive events). Following the results of CDF [14] and E-710 [53], it is conjectured that the deficiency might be an indication of a diffractive dependence that goes as

$d\sigma/dM_X \propto M_X^{-2\varepsilon}$ where $\varepsilon > 1$. Larger ε values (> 1) have the effect of shifting the generated events towards the low mass region. This has the combined effect of beginning to fill the η_{max} peak of the Monte Carlo with diffractive events, and also decreasing the fraction of elastic events in the Monte Carlo mixture. The second effect is due to low mass diffractive events having a very similar signature to elastic events in the calorimeter. As the number of low mass diffractive events increases, a smaller amount of elastic events is needed to reproduce the data. Since the elastic events have a smaller acceptance, a decrease of the elastic fraction also changes the total acceptance.

Another peak is also evident in Figure 5-1d at $\eta_{max} = 3.5$, this time with the Monte Carlo exceeding the data, again increasing the calculated χ^2 for the distribution. This will be discussed in more detail in Section 5.4.

To determine the value of ε, a comparison of the diffractive events from the data and the Monte Carlo has to be done. Experimentally, the scattered proton should be detected to identify photon diffractive events. Since for the 1993 run period, the Leading Proton Spectrometer (LPS) was not fully integrated with the ZEUS experiment, no tag of the proton was possible. Other methods are needed to select the diffractive events, involving cuts on different calorimeter distributions. Such cuts, however, will not be totally effective in removing all other processes, therefore Monte Carlo events of these other processes are used to simulate their contamination.

The double differential cross section in Table 5-1 is dependent on both M_X^2 and on t. A measurement of the variable t would require a tag of the scattered proton, but as was discussed above, the proton was not tagged during the 1993 run period. Therefore, the results must be implicitly integrated over all possible values of t giving

$$\frac{d\sigma}{dM_X^2} = \frac{C}{(M_X^2)^{2\varepsilon}} \int_{t_1}^{t_0} e^{Bt} dt, \tag{5-9}$$

where the integration limits, $t_0(M_X^2)$ and $t_1(M_X^2)$, define the range of t available for a given mass M_X. The contribution from the lower limit of the integration (t_1) is small and is ignored. The resulting single differential cross section,

$$\frac{d\sigma}{dM_X^2} = \frac{1}{M_X^{2\varepsilon}} \frac{C'}{B} e^{Bt_0(M_X^2)}, \tag{5-10}$$

consists of two pieces, each of which is a function of M_X. For the low mass region ($M_X < 20$ GeV), the exponential varies slowly as a function of M_X as shown in Figure 5-2a. In other words, the generation of events with $M_X < 20$ GeV is not hindered by the t dependence of the cross section as it is for the 18 GeV centre of mass experiments as shown with the dashed curve in Figure 5-2a. The single differential cross section solely depends on $M_X^{-2\varepsilon}$ in the low mass region. Also shown in Figure 5-2b is the acceptance of events as a function of t. The acceptance is quite flat over all values

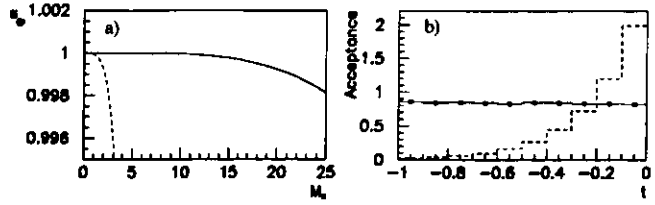

Figure 5-2 Diffractive generation characteristics

The effect on the phase space of the mass generation from the unmeasured t dependence is shown in a) as the solid curve. Also shown by the dashed curve is the phase space for a centre of mass energy of 18 GeV. At HERA energies, the phase space does not restrict the generation of masses below 20 GeV. The acceptance as a function of t is shown as the solid points in b) and is flat over the entire t range. The generated t spectrum is shown as the dashed curve with arbitrary normalization.

of t, hence no t acceptance effects will be present in the M_X distribution, and a fit to $d\sigma/dM_X^2$ directly measures the mass dependence parameter, ε, for $M_X < 20$ GeV.

As mentioned in Section 5.1.1, the diffractive cross section of the generated events can be reweighted to different values of ε and fits can be done to the diffractive mass spectrum to determine the best value of ε. In order to fit for ε, the diffractive events are isolated from the non-diffractive sample by applying a $p_z < 10$ GeV cut to the events. This cut effectively removes most of the non-diffractive events which deposit a large amount of energy in FCAL, increasing the diffractive purity, while having a high efficiency of accepting diffractive events in which the proton deposits little to no energy in the FCAL. A further cut of $\eta_{max} > -2$ is applied to the sample to remove elastic contamination. Following these cuts, a sample with a high purity of diffractive events remains. The M_X distribution of the data events can now be compared to that of a Monte Carlo mixture to determine the ε dependence. To obtain the best value, ε is varied and for each value the Monte Carlo subprocess fractions are varied and fit to the data distribution by minimizing the χ^2 formula of Eqn. (5-8). The resulting χ^2 curves, as a function of ε, for the three $W_{\gamma p}$ bins are shown in Figure 5-3. The final ε dependence is taken as the average of the minima, with an uncertainty that covers the spread of the values. Also shown in Figure 5-3 is the fit to the M_X spectrum for the $W_{\gamma p}$ = 206 GeV bin and $2\varepsilon = 2.6$.

A much more complete analysis is necessary to determine the true M_X dependence of the data (one such attempt was made in [54] with a resulting dependence of $2\varepsilon = 2.6 \pm 0.1$ (stat.) ± 0.4 (sys.)). An $M_X^{-2.6}$ dependence will be used from here on, with errors that cover the range of values for 2ε of 2.3 to 2.9 from the curves of Figure 5-3. The acceptance as a function of the parameter ε is shown in Figure 5-4 for the $W_{\gamma p}$=181 GeV bin, and can be used to adjust the total cross section

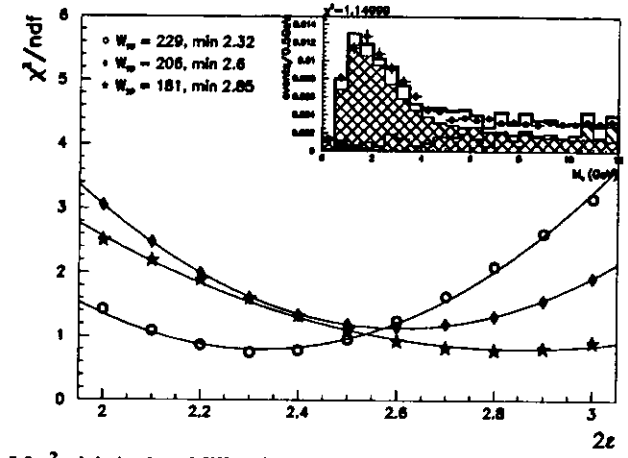

Figure 5-3 χ^2 minimization of diffractive ε dependence

χ^2 curves for the fits to the diffractive mass spectra for various mass dependences, ε, are shown. The average minimum from the curves is used as the dependence when determining the calorimeter acceptance. The inset shows the fit of the M_X spectrum for $2\varepsilon = 2.6$ and $W_{\gamma p} = 206$ GeV. The legend for the inset is the same as for Figure 5-1.

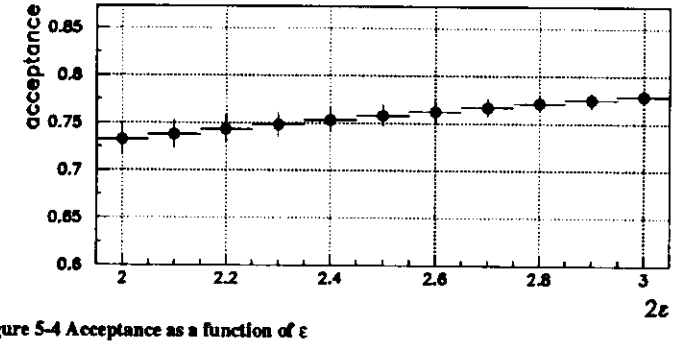

Figure 5-4 Acceptance as a function of ε

The averaged calorimeter acceptance is shown as a function of the mass dependence parameter, ε, for the $W_{\gamma p}$ = 181 GeV energy bin. The acceptance is similar for all three energy bins. The final cross section assumes a dependence of $2\varepsilon = 2.6$ for all energy bins. The final cross section can be adjusted to any desired mass dependence from the graph.

to any other dependence. Since all three $W_{\gamma p}$ bins have the same acceptance within statistical errors, only the 181 GeV bin is shown. Only statistical uncertainties are shown in Figure 5-4.

5.4 Calorimeter acceptance for $2\varepsilon = 2.6$

The recalculated calorimeter acceptances using the fitted value of $2\varepsilon = 2.6$ are shown in Table 5-5. The same trends that were evident in Section 5.2.2 remain. Of particular interest is the total acceptance for the $W_{\gamma p} = 229$ GeV bin, which is higher than the other two bins. This is due to the low fraction of elastic events fit in this bin. The low elastic subprocess acceptance and the increase of the low mass diffractive events due to the $2\varepsilon = 2.6$ dependence combine to reduce the number of elastic events. This makes it very difficult to accurately fit elastic events. As the elastic fraction is not expected to change rapidly with energy (which can be seen from the lower energy bins), the lower energy bins will be used to estimate the elastic contribution in the $W_{\gamma p} = 229$ GeV bin, similar to what was done in [11]. Using the resulting average elastic contribution of 7.0 ± 1.6%

distribution	Acceptance (%)	χ^2	Subprocess contribution (σ_i in %)					
			elastic	minb	hard	minb + hard	proton diff.	photon diff.
$W_{\gamma p} = 181$ GeV								
E_{tot}	74.6 ± 1.1	1.73	8.24	58.42	11.64	70.06	10.85	10.85
E_t	76.6 ± 1.2	2.77	6.67	67.75	3.31	71.06	11.14	11.14
η_{max}	76.3 ± 1.3	5.17	7.61	69.24	0.00	69.24	11.57	11.57
n_{cond}	77.5 ± 1.3	1.25	5.93	71.93	0.00	71.93	11.07	11.07
average	76.2 ± 1.0		7.11	66.83	3.74	70.57	11.16	11.16
$W_{\gamma p} = 206$ GeV								
E_{tot}	76.6 ± 1.4	1.27	4.04	52.33	17.04	69.38	13.29	13.29
E_t	76.6 ± 1.6	1.20	6.90	65.84	4.47	70.31	11.39	11.39
η_{max}	74.9 ± 1.7	2.32	9.95	67.91	0.00	67.91	11.07	11.07
n_{cond}	76.9 ± 1.6	1.63	6.84	66.69	4.43	71.12	11.02	11.02
average	76.2 ± 0.78		6.93	63.20	6.49	69.68	11.69	11.69
$W_{\gamma p} = 229$ GeV								
E_{tot}	79.9 ± 1.5	1.11	0.00	55.44	17.20	72.64	13.68	13.68
E_t	79.0 ± 1.7	2.08	1.65	66.23	6.01	72.24	13.05	13.05
η_{max}	74.9 ± 1.8	2.51	8.75	68.96	0.00	68.96	11.14	11.14
n_{cond}	76.8 ± 1.7	1.86	6.28	65.29	5.81	71.10	11.31	11.31
average	77.6 ± 1.9		4.17	63.98	7.25	71.24	12.30	12.30

Table 5-5 Acceptance and fitted cross sections assuming $2\varepsilon = 2.6$

from the lower energy bins, the new subprocess acceptances for the $W_{\gamma p} = 229$ GeV bin are shown in Table 5-6. The error on the average acceptance is obtained by varying the elastic contribution within its uncertainty limits (5.4% – 8.6% elastic contribution), and taking the range of values as the error on the acceptance. With the fixed elastic contribution, the total calorimeter acceptance for $W_{\gamma p} = 229$ GeV is the same as the other energy bins within statistical errors. It can be seen from the spread of acceptances in Table 5-6 that by fixing the elastic contribution, the final acceptance from the different distributions has only a small variation. This emphasizes the importance of correctly determining the elastic contribution.

distribution	Acceptance (%)	χ^2	Subprocess contribution (σ_i in %)					
			elastic	minb	hard	minb + hard	proton diff.	photon diff.
$W_{\gamma p} = 229$ GeV								
E_{tot}	76.1 ± 1.5	1.99	7.00	54.35	15.37	69.72	11.64	11.64
E_t	76.3 ± 1.7	2.32	7.00	64.81	5.78	70.58	11.21	11.21
η_{max}	75.9 ±1.8	2.54	7.00	69.84	0.00	69.84	11.58	11.58
n_{cond}	76.4 ± 1.7	1.86	7.00	65.14	5.72	70.86	11.07	11.07
average	76.2 ± 0.84		7.00	63.54	6.72	70.25	11.37	11.37

Table 5-6 Acceptances and fitted cross sections assuming 7.0% elastic contribution

The parameter ε is now varied within its limits (see Section 5.3) to determine a systematic uncertainty on the acceptance. The error is very similar for all three $W_{\gamma p}$ bins, with the largest variation slightly under 2%, thus an error of ±2% will be attributed to each bin.

Another parameter that affects the number of elastic events fit to the distributions is the cutoff value used for the diffractive mixture. As explained in Section 5.1.1, PYTHIA events are added to the NikZak events to extend the mass range from 1.7 GeV down to 1.5 GeV. As the diffractive mass generation goes lower, the contribution of the elastic events becomes smaller as the diffractive events replace them. The mass cutoff is varied between 1.2 GeV and 1.7 GeV and the resulting range of acceptances is taken as the systematic uncertainty. The variation for all bins is below 1%, thus a ±1% total error is applied to each bin.

Replacing the photon diffractive mixture with PYTHIA photon diffractive events results in a difference in acceptance below 0.5% for any bin. The diffractive mixture can also be replaced with NikZak events as well, but this has already been accounted for by the change of the diffractive mass cutoff discussed above. A mass cutoff of 1.7 GeV results in a diffractive mixture containing only NikZak events.

To this point, the Monte Carlo fits have all assumed that the ratio of the proton diffractive to photon diffractive cross section is 1:1 as was done in the 1992 analysis [52]. However, fits can also be performed allowing both diffractive types to vary freely. As was mentioned in Section 5.3, the η_{max} spectrum has a Monte Carlo peak at $\eta_{max} \approx 3.5$ (the FCAL beampipe boundary) that is much higher than data (see Figure 5-1d). A main contributor to this peak is diffractive events, in particular proton diffractive events where the remnant of the proton just enters into the FCAL. By forcing the proton diffractive cross section to be the same as the photon diffractive cross section, this peak may be artificially created. The deficit of events at $\eta_{max} \approx -1.5$ discussed previously requires an increased fraction of photon diffractive events, which has the consequence of also increasing the proton diffractive contribution and raising the forward peak away from the data. The best fit will be obtained when a balance between the two peaks is attained. Fits are done allowing the fraction of proton diffractive events to vary freely. The resulting proton diffractive contribution is close to zero for all fits. The effects on the total acceptance vary for each of the $W_{\gamma p}$ bins and are shown in Table 5-7 (labelled as diffractive ratio). Table 5-7 also summarizes all the systematic effects, and the total systematic uncertainty applied to each bin.

$W_{\gamma p}$ (GeV)	mass cutoff	diffractive ratio	ε range	PYTHIA	total
181	±1.0%	+2.0%	±2.0%	±0.5%	$^{+3.0}_{-2.3}$ %
206	±1.0%	+2.0%	±2.0%	±0.5%	$^{+3.0}_{-2.3}$ %
229	±1.0%	+3.5%	±2.0%	±0.5%	$^{+4.2}_{-2.3}$ %

Table 5-7 Summary of systematic errors

The acceptance errors listed are absolute. Thus, the systematic error due to the mass cutoff for the 181 GeV center of mass energy bin results in an acceptance of (76.2 ± 1.0)%.

5.5 Calorimeter acceptance for diffractive and non-diffractive subsamples

In order to try and simplify the fitting procedure even more, the sample can be split into a diffractive and a non-diffractive subsample. For historical reasons, the division of the diffractive and non-diffractive data components is done with a cut on the total energy in FCAL,

$$E_{FCAL} < 1 \text{ GeV for diffractive}$$
$$E_{FCAL} > 1 \text{ GeV for non-diffractive} \quad (5\text{-}11)$$

instead of the cut on the longitudinal momentum, p_z, as was done in Section 5.3. Both the cut on p_z and the cut on E_{FCAL} have similar effects, producing a high purity diffractive sample of events. The effect of the FCAL cut on the data sample is shown in Table 5-8, with most of the data sample falling into the non-diffractive subsample (≈85%). The combined acceptance calculated from the

	$W_{\gamma p}$ = 181 GeV		$W_{\gamma p}$ = 206 GeV		$W_{\gamma p}$ = 229 GeV	
	events	fraction of total	events	fraction of total	events	fraction of total
All events	131877	1.000	84791	1.000	42457	1.000
$E_{FCAL} < 1$ GeV	21910	0.166	12943	0.153	5875	0.138
$E_{FCAL} > 1$ GeV	109967	0.834	71848	0.847	36582	0.862

Table 5-8 Diffractive and non-diffractive data events

two Monte Carlo subsamples should be the same as the total acceptance from the previous section, hence this provides a systematic check of the acceptance calculation.

5.5.1 Calorimeter acceptance for $E_{FCAL} < 1$ GeV

The procedure used to fit the diffractive subsample is the same as was used for the entire sample. Table 5-9 shows the properties of the Monte Carlo subprocesses with the diffractive cut. The acceptance listed for each subprocess is the ratio of the number of measured events in the subsample to the number of generated events in the subsample. The ratio of the generated and measured events inside the subsample versus the entire sample (i.e., $(N^{gen}_{E_{FCAL}<1})/(N^{gen}_{ALL})$, $(N^{meas}_{E_{FCAL}<1})/(N^{meas}_{ALL})$) are also shown for each subprocess and in each energy bin as *gen ratio* and *meas ratio* respectively. All of the elastic events appear in the subsample, and very few of the

Subprocess	$W_{\gamma p}$ = 181 GeV		$W_{\gamma p}$ = 206 GeV		$W_{\gamma p}$ = 229 GeV	
	Acceptance (%)	gen ratio / meas ratio	Acceptance (%)	gen ratio / meas ratio	Acceptance (%)	gen ratio / meas ratio
Elastic	30.1 ± 1.2	1.00 / 1.00	21.1 ± 1.2	1.00 / 1.00	13.1 ± 1.2	1.00 / 1.00
Proton diffractive	36.0 ± 2.9	0.27 / 0.25	25.9 ± 3.0	0.25 / 0.22	18.4 ± 3.0	0.25 / 0.21
Photon diffractive mixture	80.3 ± 1.3	0.55 / 0.53	80.5 ± 1.1	0.57 / 0.54	83.0 ± 1.9	0.58 / 0.56
Minimum bias	88.8 ± 8.5	0.02 / 0.02	88.6 ± 11.7	0.02 / 0.02	90 ± 13	0.02 / 0.02
Hard mixture	61.9 ± 57.9	0.00 / 0.00	100.0 ± 81.9	0.00 / 0.00	0.00 ± 0.00	0.00 / 0.00

Table 5-9 Monte Carlo acceptances and relative fractions for $E_{FCAL} < 1$ GeV

non-diffractive (minimum bias and hard mixture) events make it into the subsample. Since only a small fraction of the hard events make it into the subsample (at most, 5 generated events in any bin), no hard mixture is used when fitting the distributions.

Since a large portion of the E_{tot} in the subsample comes from the RCAL, the dead material effects described in Section 5.2.1 become important. For this reason, the E_{tot} distribution will not be used when fitting for the total acceptance for the diffractive subsample.

The total acceptance calculated for each bin of the subsample is shown in Table 5-10. Only statistical uncertainties are shown in the table, calculated using the same method as in Section 5.2.2. The systematic uncertainties are determined as was done in Section 5.4, and are summarized in Table 5-11.

Acceptance (%)		
$W_{\gamma p}$ = 181 GeV	$W_{\gamma p}$ = 206 GeV	$W_{\gamma p}$ = 229 GeV
56.6 ± 2.3	49.7 ± 2.4	48.6 ± 2.0

Table 5-10 Acceptances for the diffractive subsample

$W_{\gamma p}$ (GeV)	mass cutoff	diffractive ratio	ε range	Pythia	total
181	±3.0%	$^{+0.1}_{-3.7}$ %	±1.5%	±0.1%	$^{+3.4}_{-5.0}$ %
206	±4.0%	$^{+0.5}_{-3.0}$ %	±2.0%	±0.1%	$^{+4.5}_{-5.4}$ %
229	±4.0%	$^{+2.5}_{-5.0}$ %	±1.5%	±0.7%	$^{+5.0}_{-6.6}$ %

Table 5-11 Summary of systematic errors for the diffractive subsample

It should be noted that the diffractive ratio now allows a range of error above and below the acceptance. This is caused by the difficulty in separating the elastic and photon diffractive contributions in the subsample. Both event types have identical signatures in the calorimeter for the subsample, but the subprocess acceptances differ. Nominally, the fraction of proton diffractive events is coupled to the fraction of photon diffractive events by a 1:1 ratio in cross section. Elastic events can then fill in any spaces in the distribution which the proton diffractive events cannot. When all event types are allowed to vary freely, a difficulty arises in selecting elastic or proton diffractive events to fill the distributions. As the proton diffractive events have smaller statistics (fewer generated events), the statistical error associated with these events is larger, which reduces the χ^2 calculated for the distribution. Hence, proton diffractive events are preferentially selected to fill the distributions. To determine a systematic error, the elastic and proton diffractive contributions are in turn forced to zero, and the range of acceptance is taken as the error.

The effect of using only PYTHIA photon diffractive events in place of the diffractive mixture is smaller than expected. This is attributed to the extra freedom of the diffractive events without the influence of the non-diffractive portions of the distributions. This is especially true of the proton diffractive events when the proton remnant deposits energy in the FCAL. These events resemble non-diffractive events and do not pass the subsample cut. When the entire sample is used, these proton diffractive events limit the total proton diffractive contribution (see the discussion on the forward η_{max} peak in Section 5.4), and hence the photon diffractive contribution as well, since the two are coupled by a 1:1 ratio by cross section. In the $E_{FCAL} < 1$ GeV subsample, however, the non-diffractive events have been removed, thus both diffractive types can vary without this constraint. This has a similar effect on the ε range as well.

The diffractive subsample acceptance is not flat over the three energy bins as can be seen from Table 5-10. However, the ratio of the diffractive subsample fraction (from Table 5-8) over the subsample acceptance is approximately constant, thus the subsample contribution to the acceptance for each bin is approximately the same.

5.5.2 Calorimeter acceptance for $E_{FCAL} > 1$ GeV

Table 5-12 shows the properties of the Monte Carlo events for the non-diffractive subsample. As with Table 5-9, the acceptance in each energy bin for each Monte Carlo subprocess is shown, as well as the fraction of generated and measured events in the subsample. The non-diffractive subsample has very few elastic events and almost all the non-diffractive events. A large frac-

Subprocess	$W_{\gamma p}$ = 181 GeV		$W_{\gamma p}$ = 206 GeV		$W_{\gamma p}$ = 229 GeV	
	Acceptance (%)	gen ratio / meas ratio	Acceptance (%)	gen ratio / meas ratio	Acceptance (%)	gen ratio / meas ratio
Elastic	23.94 ± 32.21	0.00 / 0.00	37.55 ± 52.15	0.00 / 0.00	0.00 ± 50.05	0.00 / 0.00
Minimum bias	87.07 ± 1.82	0.98 / 0.98	89.85 ± 2.46	0.98 / 0.98	90.72 ± 2.53	0.98 / 0.98
Proton diffractive	40.89 ± 1.56	0.73 / 0.75	30.26 ± 1.52	0.75 / 0.78	22.12 ± 1.46	0.75 / 0.79
Photon diffractive mixture	87.96 ± 1.13	0.45 / 0.47	91.05 ± 1.03	0.43 / 0.46	92.62 ± 2.22	0.42 / 0.44
Hard mixture	72.55 ± 1.94	1.00 / 1.00	85.60 ± 2.26	1.00 / 1.00	91.81 ± 2.46	1.00 / 1.00

Table 5-12 Monte Carlo acceptances and relative fractions for $E_{FCAL} > 1$ GeV

tion of the proton diffractive events also makes it into the subsample. Similar to Section 5.5.1, the small number of elastic events precludes them from being used in the fitting procedure.

Most of the non-diffractive events leave large amounts of energy in the very forward regions, essentially around the beam pipe. The Monte Carlo description close to the beam pipe is not very accurate. This will have a large effect on the η_{max} distribution, as the energy around the beam pipe defines η_{max}. It is found that there is no resolution for separating the contributions with the η_{max} distribution, and therefore it is not used to determine the acceptance.

Table 5-13 shows the acceptance calculated for each bin in the subsample. Again, the table only contains statistical uncertainties, with the systematic errors being summarized in Table 5-14. The small systematic uncertainties are not surprising, as the systematics mainly affect the diffractive contributions, which make up only a small fraction of the subsample.

Acceptance (%)		
$W_{\gamma p}$ = 181 GeV	$W_{\gamma p}$ = 206 GeV	$W_{\gamma p}$ = 229 GeV
84.62 ± 0.99	87.65 ± 1.29	86.96 ± 0.55

Table 5-13 Acceptances for the non-diffractive subsample

$W_{\gamma p}$ (GeV)	mass cutoff	diffractive ratio	ε range	Pythia	total
181	±0.02%	±0.5%	±0.2%	±0.01%	±0.54%
206	±0.01%	±0.5%	±0.2%	±0.2%	±0.57%
229	±0.01%	±0.5%	±0.5%	±1.0%	±1.2%

Table 5-14 Summary of systematic errors for the non-diffractive subsample

The acceptances in each bin of this subsample are very similar. Again, the ratio of the subsample fraction given in Table 5-8 over the subsample acceptance is almost constant for all bins. Together with the results of the previous section, this results in a flat overall acceptance for the combined subsamples.

5.6 Final acceptance and conclusions

Combining the results from the diffractive and non-diffractive subsamples results in the total acceptances listed in Table 5-15. Both statistical and systematic errors are listed. These values can be compared to the values from Table 5-5 and Table 5-6. The total acceptance calculated from the subsamples is again flat in $W_{\gamma p}$, but the final acceptance is higher. This is again attributed to the ability of the diffractive events to vary more freely in each of the subsamples. A +2% systematic shift will be added to the final error for the calorimeter acceptance, which is shown in Table 5-16.

Acceptance (%)		
$W_{\gamma p}$ = 181 GeV	$W_{\gamma p}$ = 206 GeV	$W_{\gamma p}$ = 229 GeV
78.2 ± 1.2 (*stat*) $^{+1.1}_{-1.6}$ (*sys*)	78.5 ± 1.5 (*stat*) $^{+1.8}_{-2.1}$ (*sys*)	78.4 ± 1.3 (*stat*) $^{+2.0}_{-2.5}$ (*sys*)

Table 5-15 Total acceptance from diffractive and non-diffractive subsamples

Acceptance (%)		
$W_{\gamma p}$ = 181 GeV	$W_{\gamma p}$ = 206 GeV	$W_{\gamma p}$ = 229 GeV
76.2 ± 1.0 (*stat*) $^{+3.6}_{-2.3}$ (*sys*)	76.2 ± 0.78 (*stat*) $^{+3.6}_{-2.3}$ (*sys*)	76.2 ± 0.84 (*stat*) $^{+4.6}_{-2.3}$ (*sys*)

Table 5-16 Final calorimeter acceptance and uncertainty

The error is dominated by systematic effects from the unknown fractions of the elastic and diffractive events. The LPS, which was completed for the 1994 run, will provide a tag of the outgoing proton allowing the separation of the elastic events from the proton diffractive events, as well as providing a measure of the t dependence. This separation will permit the determination of the elastic and diffractive contributions, and should greatly reduce the systematic error. Beginning in the 1994 run period, dedicated runs with a shifted z vertex position were also taken. For these runs, the beams are shifted so that they collide closer to the FCAL. These runs should provide another handle for the separation of the elastic and diffractive contributions as the opening angle, hence acceptance, for particles to enter the RCAL is larger. The increased resolution should allow a much better separation of the proton diffractive events from the elastic contribution [55]. It can be seen from the acceptances in Table 5-6 that the determination of the elastic contribution has a substantial impact on the final acceptance.

No simple method exists for observing the effect of the RCAL energy shift, mentioned in Section 5.2.1, on the calculated acceptance from the Monte Carlos. In Section 5.7, a conservative estimation of the energy shift is included in the error for the trigger correction, thus no further error is assigned to the calculated acceptance. To properly study this effect requires a Monte Carlo simulation with a proper description of all the dead material, as well as the regeneration of all the relevant subprocesses. New versions of the simulation package, MOZART, have a much better description of the detector and should provide more insight into these effects for the 1994 and 1995 running periods.

5.7 Trigger efficiency and event loss

The online trigger acceptance is another factor which affects the calculated cross section. Events that trigger close to threshold may migrate out of the sample due to miscalibration of the trigger towers online (see Section 4.1.1 for a description of the trigger used for this analysis). Like-

wise, events just below the trigger threshold may also migrate into the sample. This is illustrated in Figure 5-5, with the dotted curve showing the trigger behavior of the data, and the step indicating the ideal trigger behavior. Since a large portion of the sample triggers very close to threshold, this may have a large impact on the final cross section. This can of course be corrected for by reproducing this behavior in the Monte Carlo simulation of the trigger system, but for 1993 the Monte Carlo was generated with the trigger tower thresholds at the nominal values (the step behavior).

To study the trigger behavior, the Monte Carlo trigger simulation was run on the data sample. For the Monte Carlo, the trigger values are determined from the energy in each of the calorimeter towers. As one of the offline reconstruction steps, all the calorimeter towers are recalibrated to a much higher precision, so the new trigger values should mimic those of the Monte Carlo. This allows the immediate elimination of events which should not have fired the trigger but migrated into the sample (the tail of the dotted curve on the left hand side of the ideal trigger behavior in Figure 5-5). A cut of the offline trigger values (called *TREMC* and *TREMCTH* hereafter) at the same threshold as the online values (*ONREMC* $\geq$ 464 MeV or *ONREMCTH* $\geq$ 1250 MeV are the online values) is first applied.

To study the events which should have passed the online trigger but did not, the offline trigger threshold can be raised until the losses from the online trigger miscalibration are negligible. In other words, raise the offline trigger threshold values (*TREMC*, *TREMCTH*) until the event loss from the online trigger values (464,1250 MeV) is negligible. An estimate of what the offline thresholds should be is determined using the fact that the online trigger is an "OR" of two different

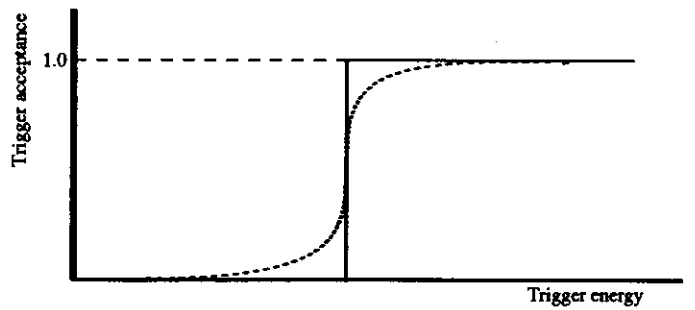

Figure 5-5 Trigger threshold behavior
The acceptance of events for the online RCAL trigger as a function of the trigger threshold is shown. The ideal trigger behavior is shown by the solid step function, with 100% acceptance for event above threshold and 0% acceptance for events below threshold. The behavior of the data is shown with the dotted curve. Events below threshold can migrate into the triggered sample, and likewise event above threshold may fail to pass the trigger requirement.

RCAL triggers. Either of the two triggers can be studied by demanding that the other trigger accepts the event. In this way, the losses from the trigger can be estimated. For example, the *TREMC* trigger can be studied by requiring the events be triggered by the *ONREMCTH* trigger, and examining the fraction of events that should have passed the online trigger but did not for different *TREMC* trigger thresholds, as is shown in Figure 5-6. For different *TREMC* thresholds, the number of events that pass the threshold but did not pass the online trigger cut, *ONREMC*, are counted and compared to the total number that did pass both cuts. This gives the percentage of lost events shown in Figure 5-6. This procedure can also be repeated to look at the *TREMCTH* thresholds by requiring the events be triggered with the *ONREMC* trigger. The event loss fraction from Figure 5-6 cannot be directly used to correct the cross section as the two triggers are not independent. They do however allow the determination of the proper offline trigger thresholds to apply to the data to eliminate the trigger loss effect. By raising the trigger thresholds one step up for each offline trigger, the losses become negligible. Recalculating the cross section at these higher trigger thresholds will eliminate the threshold effects.

A correction factor, δ_{trig}, will be applied to the cross section calculated with the nominal offline trigger thresholds. δ_{trig} is calculated as the ratio of the fractions, $f(TREMC,TREMCTH) = (N/\mathcal{L})(1/A_{RCAL})$, for the new trigger thresholds versus the nominal trigger thresholds, for example

$$\delta_{trig} = \frac{f(660, 1875)}{f(464, 1250)}. \qquad (5\text{-}12)$$

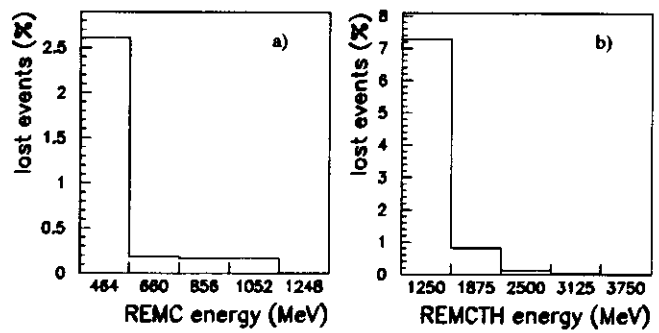

Figure 5-6 Event losses due to online trigger effects
The fraction of events lost online for an offline threshold setting is shown for different TREMC trigger values in a) and for different TREMCTH trigger values in b) for the $W_{\gamma p}$ = 181 GeV energy bin. While the actual lost events change for the different energy bins, the shapes of the two distributions remain the same.

Table 5-17 lists the quantities calculated with the trigger thresholds raised by one unit and raised by two units, along with the calculated correction factor. The correction factor will be taken as the average from all bins for both increased trigger thresholds. This yields a nominal correction factor of $\delta_{trig} = 1.09 \pm 0.01$ where the error on the correction is taken from the spread of values.

$W_{\gamma p}$ (GeV)	new trigger thresholds (660,1875 MeV)			new trigger thresholds (856,2500 MeV)		
	$N/\mathcal{L}$ (μb)	A_{RCAL} (%)	δ_{trig}	$N/\mathcal{L}$ (μb)	A_{RCAL} (%)	δ_{trig}
181	0.4495	59.32	1.08	0.3980	51.70	1.10
206	0.2969	60.72	1.09	0.2697	54.73	1.09
229	0.1522	63.21	1.08	0.1416	57.35	1.11

Table 5-17 Effects of increased trigger thresholds

Another effect is also present in the trigger correction, namely the RCAL energy shift. The effect of the energy shift is not expected to be the same at the different trigger thresholds. However, by changing the trigger thresholds, no change in the underlying physics will occur and the subprocess fractions should remain constant; therefore, by studying the fit calorimeter subprocess fractions at the different trigger levels, an estimation of the energy shift is possible. The calorimeter acceptances for the higher trigger thresholds shown in Table 5-17 were determined by comparing the data to a Monte Carlo mixture of the different subprocesses as explained in Section 5.2. By replacing the subprocess fractions at the higher trigger thresholds with those determined at the nominal thresholds (464 GeV, 1250 GeV) and recalculating δ_{trig}, the result is a new average correction of $\delta_{trig} = 1.05$. The variation in δ_{trig} is assigned to the systematic uncertainty due to the energy shift, and the error is conservatively assumed to be symmetric about the central value, resulting in a final trigger correction of 1.09 ± 0.01 (statistical) ± 0.04 (systematic).

6 Luminosity monitor

The two detectors of the luminosity monitor, described in Section 3.5, play important roles in the determination of the photoproduction cross section. The photon calorimeter is used to measure the total luminosity of the runs used in this analysis, as well as to monitor the beam parameters associated with the electron beam, such as tilt. The electron detector is used to measure the virtual photon, γ^*, exchanged in the interaction by detecting the scattered electron.

6.1 Luminosity measurement

The luminosity measurement is based on the electron–proton bremsstrahlung process ($ep \rightarrow ep\gamma$) [29][56]. This process was selected because of the large cross section and the clean experimental signature. The cross section can be calculated very precisely from QED (Eqn. (2-41)). The luminosity is determined by counting the bremsstrahlung photons above an energy threshold and dividing by the corresponding calculated cross section,

$$\mathcal{L} = \frac{dN_{br}/dt}{\sigma_{br}^{obs}}, \qquad (6\text{-}1)$$

where dN_{br}/dt is the background corrected rate of bremsstrahlung photons above the energy threshold and σ_{br}^{obs} is the bremsstrahlung cross section corrected for experimental effects.

6.1.1 Bremsstrahlung event rate

The event rate, dN_{br}/dt, was counted using various Global First Level Trigger scalers with differing cuts on the electron and/or photon energies. Of interest for the luminosity measurement are the four scalers R_{all}^{5}, R_{all}^{10}, R_{pil}^{5}, R_{pil}^{10} which counted all the events and the electron pilot events for photon energies above 5 and 10 GeV. Online at the FLT, the photon detector has not been calibrated, thus the energy thresholds assume a nominal ADC calibration, and miscalibration effects must be taken into account offline.

Before determining the luminosity, the event rate must first be corrected for multiple events. As the probability of a bremsstrahlung event occurring for each bunch crossing increases, the probability for two bremsstrahlung events to occur simultaneously can become non-negligible.

This has two effects on the count rate. First, when each of the sub-events does not pass the trigger threshold, but the combined event does, the count rate increases. Second, when both of the sub-events are good[1] events, the two events combined count as a single event which decreases the count rate. The correction for the multiple events is calculated using the Monte Carlo sample. The results show that all rates are close to the true rate within small corrections, and for the photon energy threshold of 5 GeV, the rate is almost unaffected by these pileup effects.

A large source of background comes from the interaction $Ae \rightarrow Ae\gamma$ (i.e., bremsstrahlung involving a beam electron and a residual gas molecule inside the beam pipe, also known as egas). Corrections for this background are done statistically using the method of statistical subtraction discussed in Section 4.3. The event rate of the pilot bunches is used to correct the overall rate,

$$R_{br} = R_{all} - R_{pil}\frac{I^e_{all}}{I^e_{pil}}, \tag{6-2}$$

where $R_{br} \equiv dN_{br}/dt$ is the background corrected bremsstrahlung count rate, and I^e's are the electron beam and pilot bunch currents measured by the HERA machine group. The accuracy of the background subtraction depends crucially on the measurement of the bunch currents and the counting of the pilot bunches in the same manner as the colliding bunches. Monitoring of the background subtraction revealed a possible 0.5% underestimation of the egas background contribution which is ascribed to the systematic uncertainty.

Further counting errors of the FLT scalers were cross checked by comparison with similar counters in the LUMI readout system, and it was found that such errors were below 0.3%.

6.1.2 Observed bremsstrahlung cross section

The observed cross section, σ^{obs}_{br}, can be written in the form

$$\sigma^{obs}_{br} = \int_{E_{th}} A_\gamma d\sigma_{BH}, \tag{6-3}$$

where A_γ is the acceptance for bremsstrahlung events in the LUMI photon detector, σ_{BH} is the bremsstrahlung cross section calculated using the Bethe–Heitler equation from Section 2.6, and the integration extends over the full range of available photon energies. The observed cross section must be corrected for various effects like the acceptance for the photon detector. These effects can change in time, and must be monitored carefully.

1. Here, "good" implies that the bremsstrahlung sub-event would have passed the energy threshold requirement.

The calculated luminosity must be corrected for the geometrical acceptance, A_γ, of the photon detector. The acceptance depends upon the position of the interaction point (IP) as well as the electron beam parameters, such as the horizontal beam tilt, at the IP. The position measurement of the photon detector can be used to monitor such beam parameters. The typical scattering angle of a bremsstrahlung photon[1] is much smaller than the typical electron beam tilt (~0.15 mrad) and divergence (0.13 mrad) at the IP. This allows the electron beam parameters to be determined from the photon position measurement. As detailed in [56], the luminosity is corrected for the electron beam tilt with an error of 0.5% from Monte Carlo comparisons with typical tilt values. A further error on the acceptance due to the limited Monte Carlo statistics also contributes a 0.6% error to the calculated luminosity.

The cross section calculated using the Bethe–Heitler equation from Section 2.6 is a Born level approximation, thus is not an exact calculation. Effects such as higher order corrections and the use of different proton structure functions have been estimated to contribute less than 0.5% error [29]. The effect of the finite lateral beam size has not been accurately measured and also contributes to the overall theoretical uncertainty. The total error on the cross section calculation was estimated to be 1.0% [29] at HERA energies.

Errors due to the accuracy of the calibration procedure, uncertainty of the calorimeter energy resolution, non-linearity of the photon calorimeter, and errors on the pedestal values were all checked and are described in detail in [29] and [56]. These effects contribute the largest uncertainty to the luminosity measurement, totalling ~2.2%.

6.1.3 Summary of luminosity measurement

The total systematic effect from the combined errors for σ^{obs}_{br} and dN_{br}/dt result in a 2.6% systematic uncertainty for the 5 GeV photon energy threshold and a 2.5% error for a 10 GeV threshold. A comparison of the luminosity obtained with each threshold provides a test of the photon energy scale, and shows good agreement [29]. Good photon calibration is essential in determining the energy of the photon thresholds used (online, all thresholds are in ADC counts, and a nominal calibration is assumed).

6.1.4 Calibration of photon detector

As mentioned above, good calibration is needed for the luminosity calculation. The calibration of the photon detector is also based on a characteristic of the bremsstrahlung process, namely that the end-point of the photon spectrum should come out to the electron beam energy, E_e.

1. The average photon scattering angle, m_e/E_e, for a 26.67 GeV electron beam is 0.019 mrad as shown in Section 2.6.

Each of the LUMI calorimeters is read out by two redundant channels. To determine the measured energy, a geometric mean is used:

$$E_{meas} = \sqrt{E_l E_r} = \sqrt{c_l (ADC_l - PED_l)\, c_r (ADC_r - PED_r)}, \qquad (6\text{-}4)$$

where the calibration constants, c_l, c_r, relate the photomultiplier tube readout values, ADC_l, ADC_r, to the energies E_l, E_r after subtraction of the pedestals PED_l, PED_r. The geometric mean has the advantage of requiring only one calibration constant, $c = \sqrt{c_l c_r}$ and also eliminating any attenuation effects due to the hit position.

The calibration relies on the fact that the photon energy cannot be greater than the initial electron energy. This shows up as a sudden drop in the photon energy spectrum at the beam energy. The bremsstrahlung photon spectrum is then fit with the Bethe-Heitler cross section convoluted with a gaussian function accounting for the energy resolution of the calorimeter. The fit is done to the high energy end of the spectrum to reduce the effect of energy loss in the carbon filter in front of the photon calorimeter. An example of this fit for a portion of run 7200 is shown in Figure 6-1. The normalization factor, $P1$, and the calibration constant, $P2 \equiv 1/c_\gamma$, are shown. The sudden drop of the photon spectrum at the beam energy is clearly evident. The error on the photon calibration was estimated at ≈1.0% [57].

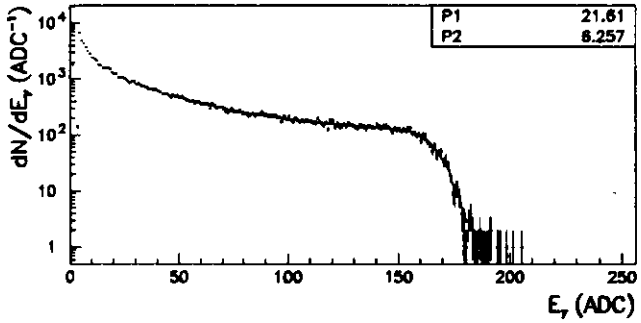

Figure 6-1 Photon detector calibration
The calibration of the photon detector using bremsstrahlung events is shown. The points are fit using a convolution of the bremsstrahlung cross section and a gaussian function for the detector resolution. The normalization for the fitted function is given by P1, and the calibration constant is given by P2.
Figure courtesy of Johannes Mainusch.

6.1.5 Calibration of electron detector

To calibrate the electron detector, another characteristic of the bremsstrahlung events is exploited, namely that the sum of the photon and the scattered electron energies should add up to the beam energy,

$$E_{beam} = E_\gamma + E_e. \qquad (6\text{-}5)$$

Bremsstrahlung events are selected from the tagged coincidence correlation band (see Section 4.3.3) by applying cuts using the photon calibration from the previous section and assuming an approximate calibration constant for the electron detector. The cuts are designed to select events only in the central region of the detector, away from the edges where energy may be lost due to leakage. A fit to the electron and photon energy correlation of the resulting events, results in a new value for the electron calibration constant, c_e (see Section 6.1.4). The entire procedure starting with the event selection is then repeated, with the new value of c_e found in the previous iteration, until the change in c_e falls below the 1% level. As a miscalibration of the photon detector will clearly lead to a miscalibration of the electron detector, the uncertainty of c_e also contains the uncertainty of c_γ, and is estimated to be ≈1.5% [57].

6.2 Monte Carlo Generation

Due to the position of the LUMI electron detector ~35 m in the electron direction (see Section 3.5), an understanding of the electron acceptance requires a detailed description of the electron path between the IP and the detector. A complex system of magnets steers and focuses the proton and electron beams in the region of the IP. As shown in Figure 3-6, to reach the electron calorimeter, the electrons are first deflected by several quadrupole and dipole magnets. The electrons that are below the beam energy are deflected such that they leave the beam pipe at ~27 m and strike the electron detector. Any changes to the electron path (such as changing the interaction point or electron beam characteristics such as the tilt) will result in the scattered electron having a different orbit through the magnet system and change the observed behavior of the electrons in the electron detector. The aim of the Monte Carlo was to describe all elements of HERA (i.e., magnet positions and field strengths, other beam pipe structures, beam parameters, etc.) and the electron detector as accurately as possible. To this end, the detector simulation program, MOZART [58], which uses the CERN package GEANT [59] to describe the detector, was modified to include all relevant structures. Several changes were made from the 1992 version which can be seen in Figure 6-2. The corrections to the Monte Carlo description are discussed in detail in [11], and are summarized here:

- The magnet positions were set to HERA design parameters to within ±1 mm. The field strength for each magnet was also set to design parameters. The positions and field strengths had been adjusted for the 1992 Monte Carlo to describe the conditions present at that time.

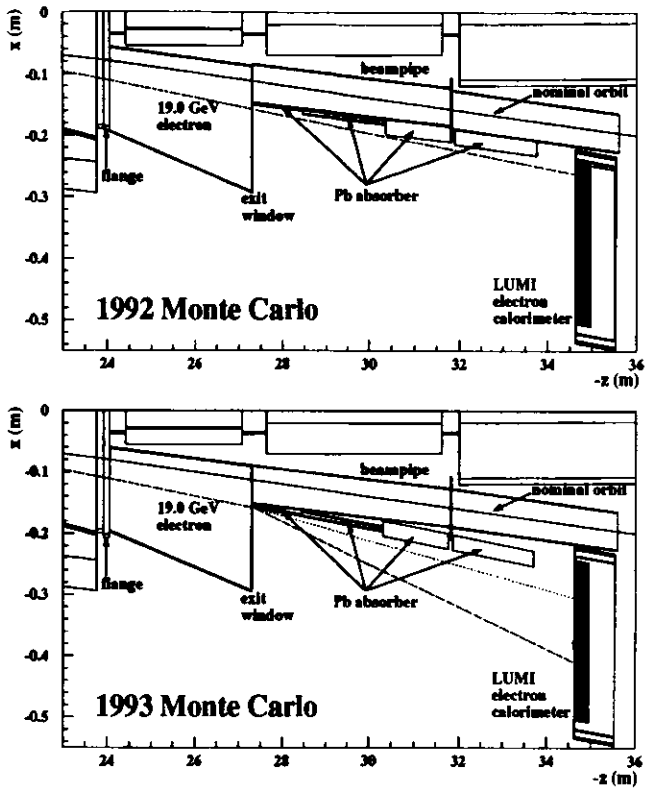

Figure 6-2 Changes to electron simulation

The 1992 detector simulation of the LUMI electron calorimeter and beam pipe is shown in the upper figure. The modified simulation for the 1993 run is shown in the lower figure. The major components that were changed in the new simulation are labelled. Particularly evident is the change in the lead absorber position which affects the ≈19 GeV electrons. The simulation of a 19 GeV electron is shown for each case.

- The beam pipe and flange in the electron detector vicinity were repositioned. The corrected flange position increased the acceptance of ~10 GeV electrons. The position of the beampipe is important for high energy electrons (~23 GeV) which can shower through the beampipe and deposit energy inside the electron detector as illustrated in Figure 6-3.

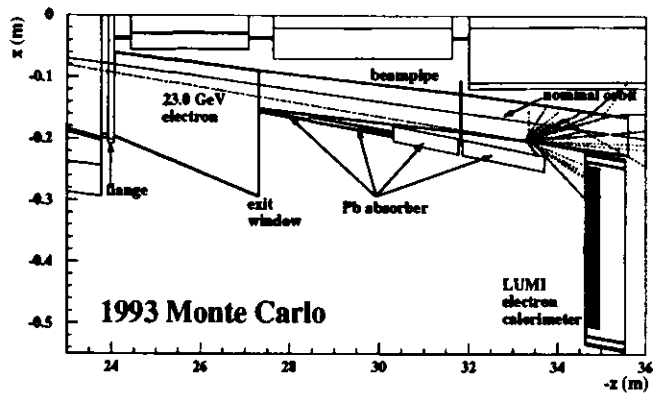

Figure 6-3 Simulation of high energy electrons

The trajectory of very high energy electrons is shown. It is possible for the electron to shower through the beam pipe and deposit energy in the LUMI electron detector.

- The lead shielding absorber was repositioned to match measurements. The shielding position is important for the acceptance of high energy electrons. The change of the absorber position can clearly be seen in Figure 6-2, as well as its effect on 19 GeV electrons.
- The lumi electron calorimeter description of position and housing was adjusted to correspond to measurements.

The objective of the revised Monte Carlo was to describe all elements of the electron beam line to an accuracy of 1 mm. A further uncertainty in the magnet positions close to the IP is compensated by shifting the x position of the IP in the Monte Carlo until agreement with data is obtained. This IP position is then used in all further simulations of the data.

Bremsstrahlung events are first generated using the BREMLU [60] package which is based on the BREMGE [61] event generator, and then passed through the MOZART detector simulation. BREMGE generates events according to the Born level Bethe-Heitler cross section given by Eqn. (2-41). Effects due to the limited transverse beam size are also included. Events were generated at the IP ($x = y = z = 0$) and were redistributed about the IP (i.e., gaussian in y,z and flat or gaussian in x) before being passed through the detector simulation.

The HERACLES4.2 [23] event generator is used to simulate the scattered electron and possible photons from photon-proton interactions. The full differential cross section discussed in Section 2.5.3 is included in the generator. The input description of σ_T and σ_L for the event interaction is provided by the ALLM [21] parameterization. Similar to the bremsstrahlung events, the

physics events are generated at the IP and are then redistributed as required before the detector simulation is applied.

6.2.1 Calibration of Monte Carlo

The calibration of the Monte Carlos used to describe the data involves matching the event characteristics observed in the data. In effect this amounts to recalibrating the electron and photon detectors in the Monte Carlo to give results consistent with that of data. An iterative procedure is used to fine tune the Monte Carlo calibration. As both electron and photon energies are needed to do the calibration, bremsstrahlung events are used, and the calibration constants obtained are applied to all other Monte Carlos.

To do the calibration, Monte Carlo bremsstrahlung events are compared to the tagged bremsstrahlung events from the data (see Figure 4-7 and Section 4.3.3) which must be extracted from the data sample. The tagged data bremsstrahlung events are selected from the data with cuts assuming a beam energy of 26.67 GeV as seen by the LUMI. The energy sum of the electron and photon detectors is then plotted and fit to determine the average LUMI measured beam energy. All cuts are re-adjusted to match the newly determined LUMI beam energy and the procedure is repeated until convergence between the cut energy and the measured beam energy is obtained. The end result is shown in Figure 6-4a, with the average measured beam energy of the data in LUMI being 26.57 GeV.

The summed beam energy from the bremsstrahlung Monte Carlo, BREMLU [60], has to be adjusted to match the data. This can be accomplished by applying a calibration constant to the electron and/or the photon energy. To determine the correct calibration, the plot of average photon energy as a function of electron energy is done for both data and Monte Carlo (see Figure 6-4b and d). The line of constant beam energy at 26.57 GeV is shown in each plot. Both the data and the Monte Carlo follow the line of constant beam energy, except at each end of the spectra where both curves begin to deviate. This will be discussed later. Since the Monte Carlo is supposed to mimic the data, the ratio of this data curve to the Monte Carlo curve is used for the calibration.

The curve of Figure 6-4b for the data is divided by the curve of Figure 6-4d for the Monte Carlo, resulting in a distribution of the ratio of photon energies as a function of the electron energy. If the Monte Carlo calibration matches the data calibration, this distribution should be flat in electron energy with an intercept of 1.0. To match the calibrations, the calibration constant for the electron energy in the Monte Carlo is changed until the distribution becomes flat (slope close to zero) regardless of the intercept. The photon calibration constant is then adjusted until the intercept becomes 1.0. This procedure is repeated iteratively until the distribution is both flat and has an intercept at one as shown in Figure 6-5 (here, *A0* denotes the intercept, and *A1* the slope). A linear fit is made to the distribution to determine the slope and intercept using the points from the region of

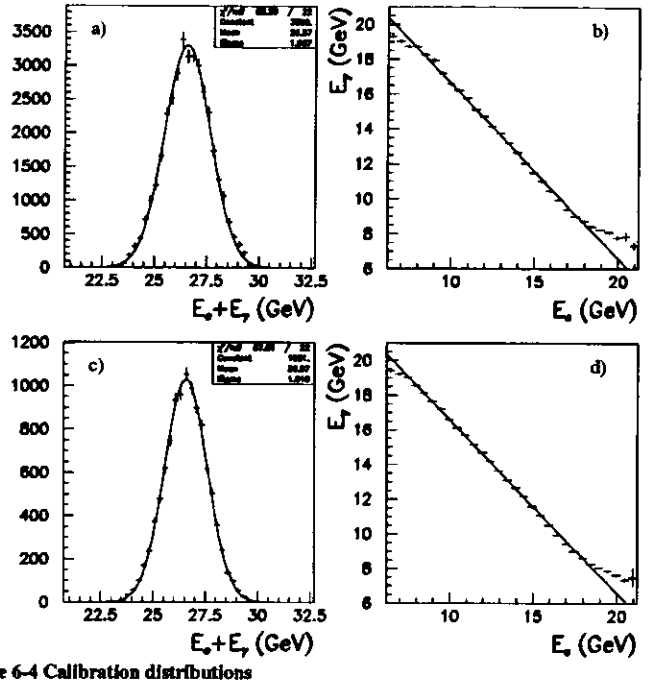

Figure 6-4 Calibration distributions
The calibration to the data (plots a) and b)) of the HERACLES4.2 Monte Carlo (plots c) and d)) is shown. The sum of the electron and photon energies (a) and c)) are adjusted in HERACLES4.2 to match the data. The correlation between the electron and photon energies (b) and d)) is also adjusted in HERACLES4.2 to match that of data. The line in the correlation shows the constant energy sum of 26.57 GeV.

interest (electron energies in the range 9.2-18.2 GeV). Outside this region, large deviations from the beam energy become noticeable as mentioned above. This is caused by energy leakage from the detector due to electrons impacting close to the edge of the detector.

6.3 Comparisons of Monte Carlo and data

The Monte Carlo description of the beam parameters is very important to properly reproduce the data. It will be shown in Section 6.3.3 that the electron acceptance strongly depends on the exact horizontal position of the IP since different positions imply a different path followed by the electron through the focussing and bending magnets. Changes in the vertical direction have

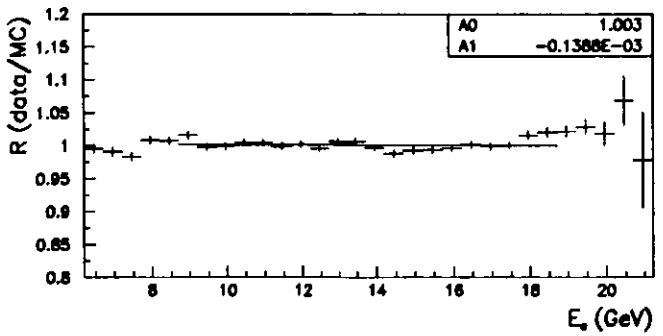

Figure 6-5 Calibration ratio
The ratio of the average photon energy in data versus Monte Carlo as a function of electron energy is shown. A linear fit to the ratio over the region of interest is used to calibrate the Monte Carlo. The calibration procedure requires the fit to be flat (A1 ~ 0.) with an intercept (A0) at 1.0.

very little effect as the quadrupole magnets focus the electrons back towards the center. It was checked that the electron acceptance did not depend on the y tilt or vertex position.

6.3.1 Exchanged photon energy

The Monte Carlo simulation of the physics events contains no simulation for the main calorimeter. The data sample contains events that pass an $E_{RCAL} \geq 1$ GeV trigger requirement (see Section 4.2). By energy and momentum conservation, the trigger requirement ensures that the exchanged photon has at least 1 GeV energy. This trigger is simulated in Monte Carlo by requiring that the exchanged photon energy, E_{γ}, be a minimum of 1 GeV.

6.3.2 Beam tilts

As mentioned in Section 6.1.2, the photon hit position can be used to monitor certain electron beam characteristics at the IP. The optimal horizontal tilt of HERA was -0.15 mrad. The HERA operators attempted to maintain this tilt within ±0.05 mrad variations. The vertical beam tilt was kept at 0 mrad. Offline measurements showed the optimal horizontal tilt to be -0.16 mrad, which was used for simulations. The beam divergences for the simulations were taken from the HERA design values. The beam tilt is measured from the photon hit position using the relation

$$\theta_{\gamma}^{x(y)} = \frac{x(y)}{l_{\gamma}}, \qquad (6\text{-}6)$$

where $\theta_{\gamma}^{x(y)}$ is the horizontal (vertical) tilt angle, x (y) is the horizontal (vertical) hit position, and l_{γ} is the distance to the photon detector (≈107 m). A comparison of the hit position in the photon calorimeter between bremsstrahlung events from data and Monte Carlo is shown in Figure 6-6. The general features of each distribution are sufficiently described by Monte Carlo. It was checked that the electron acceptance did not depend on the vertical (y) tilt at the IP.

6.3.3 Interaction vertex position

Due to the uncertainty of certain magnet positions, discussed in Section 6.2, the position of the IP is uncertain and cannot be measured directly. The acceptance of the electron calorimeter is very sensitive to the actual IP position used as shown in Figure 6-7. A small change in the horizontal position of the IP of only 1 mm can cause a change in the electron acceptance of up to ≈8% for the $W_{\gamma p}$ = 181 GeV bin.

The bremsstrahlung Monte Carlo is used to determine the correct IP position. The bremsstrahlung events are well suited for this task as they are well understood (see Section 6.1.2), and have a smaller average Q^2 (which translates to a smaller average scattering angle of the electron) than the physics events. Both the LUMIE energy and position information is used to determine the IP position. For the physics events, it is not possible to use any x hit position information as the background subtraction does not properly take into account the dependence of the hit position on the electron energy.

The comparison of Monte Carlo and data is done using selected measured distributions. The distributions used in this analysis are:

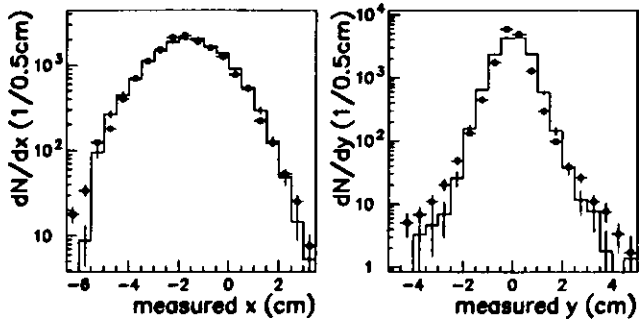

Figure 6-6 Photon impact positions
A comparison of the measured photon x and y impact positions on the LUMI photon calorimeter is shown. Points refer to the data and the solid histogram to the Monte Carlo simulation.

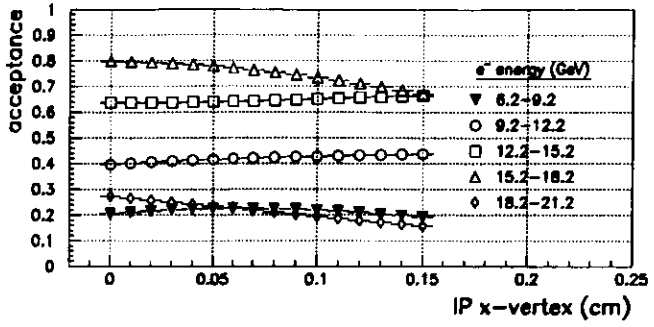

Figure 6-7 Electron acceptance as a function of the vertex position
The acceptance of the scattered electron is shown as a function of the x vertex position at the IP for various scattered electron energies ($W_{e\gamma}$ bins). Events were generated using HERACLES4.2.

- the measured electron energy spectrum, E_e, in the electron detector,
- the measured electron x hit position in the electron detector,
- the correlation of the electron energy and x hit position,
- and the correlation of the electron energy measured using the photon calorimeter, using the relationship from Eqn. (6-5) and the x hit position from the electron detector. Since only the photon energy is used, the energy measurement is free of any miscalibration of the electron detector.

The distributions are limited to the region in which the cross section is measured ($9.2 < E_e < 18.2$). An example fit to these distributions is shown in Figure 6-8. The distributions are compared using the χ^2/ndf defined by Eqn. (5-8), which is displayed in the upper right hand corner for each distribution in Figure 6-8.

The Monte Carlo is generated with a gaussian distribution about different horizontal vertex positions. This is accomplished by generating a flat Monte Carlo sample and reweighting the events to give a gaussian centered on the chosen vertex position as illustrated in Figure 6-9. The χ^2/ndf for each of the selected comparison distributions is then calculated for each of the vertex positions. The width of the gaussian around each chosen position is kept large to account for the run to run variations present in the data.

The optimal vertex position is determined by plotting the calculated χ^2/ndf as a function of the x vertex position for each of the distributions as shown in Figure 6-10. The minimum of each of the curves, labelled for each distribution in Figure 6-10, is interpreted as the optimal vertex position. The average position determined from the four curves, at $x = 0.087$ cm, is taken as the vertex position used in all further analysis. The rather large χ^2 at the minimum of the position

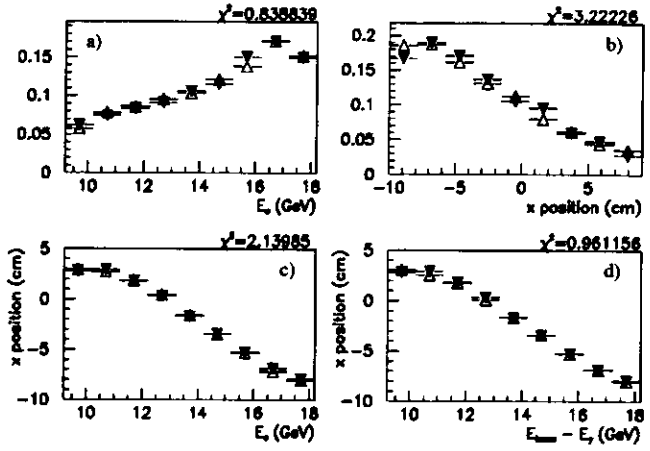

Figure 6-8 LUMI electron comparison distributions
The comparison of bremsstrahlung data and Monte Carlo for four different measured LUMI distributions are shown. a) shows the electron energy spectrum, b) the electron hit position spectrum, c) the average hit position versus the electron energy, and d) the electron hit position versus the electron energy calculated from the photon calorimeter. Empty triangles represent Monte Carlo, and filled triangles represent data. The calculated χ^2/ndf between Monte Carlo and data is also shown at the top right of each distribution.

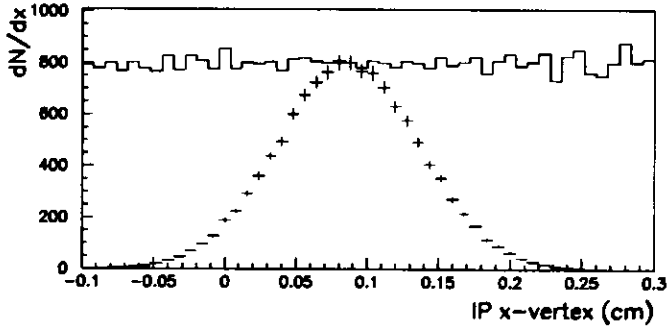

Figure 6-9 Reweighting of Monte Carlo vertex position
Gaussian distributions about various vertex positions (points) are obtained by reweighting a Monte Carlo with a flat vertex distribution (solid line). The vertex position and width are selected and all events are given an appropriate weight.

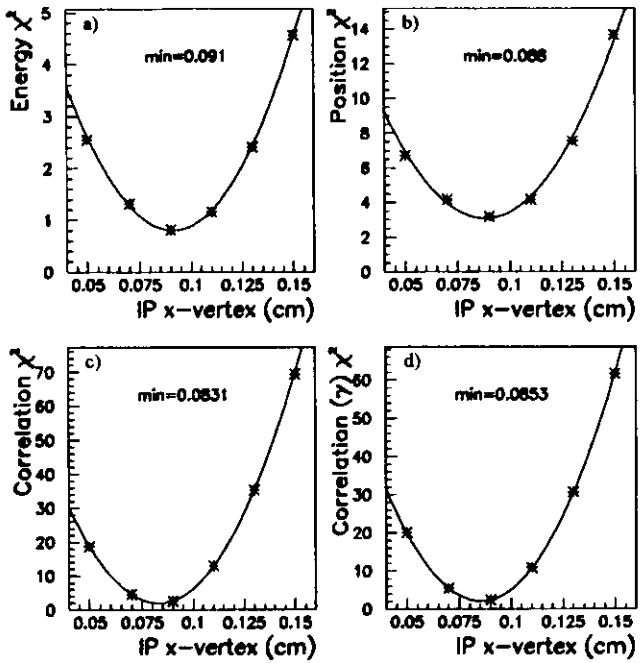

Figure 6-10 χ^2 minimization curves for LUMI distributions
*The calculated χ^2 corresponding to the difference between data and Monte Carlo as a function of the generated Monte Carlo x vertex position of the IP are shown as * for a) the electron energy, b) the electron hit position, c) electron energy versus the average hit position and d) the electron energy from the photon detector versus the average electron hit position (see Figure 6-8). The χ^2 points are fit with a parabolic curve to obtain the minimum, which is taken as the optimal vertex position.*

distribution is expected as all position information, including events with positions near the edge and with multiple position readings, are used, not just events with a well measured position tag. A check using only well measured positions resulted in consistent minima but with a much lower χ^2 at the bottom of the position spectrum. Variation of the width of the vertex gaussian was also checked and found to give consistent results.

The variation in the minima of the four distributions is taken as an error on the vertex determination. The largest variation of the minima is used for this error, which is determined to be ±0.004 cm. Systematic shifts from the miscalibration of the energy were also checked by shifting

the energy in the Monte Carlo by ±1.5% and refitting for the minima. The total error on the vertex from energy miscalibration is ±0.012 cm. Similarly, a shift of ±2 mm was applied to the electron hit positions resulting in an error of ±0.007 cm to the vertex position. From Figure 6-8c and d, it is obvious that the error from the energy and position are correlated, thus cannot be added in quadrature. All errors are added linearly, resulting in a final error of ±0.023 cm on the vertex position.

The newly determined horizontal position of the IP compensates for the systematic uncertainty of the magnet positions. The electron tagging efficiency does not depend crucially on the *y* vertex position as the quadrupole magnets tend to refocus the beam back onto the centre of the electron detector. A shift of the *z* position also has limited effect on the tracking of the electron to the detector.

A comparison of the electron energy and *y* hit position for physics events is shown in Figure 6-11. There is very good agreement between Monte Carlo and data for the energy spectrum, and the *y* position spectrum also agrees very well after an ≈2mm correction to the Monte Carlo y position. The Monte Carlo appears to be a good simulation of the data. As mentioned previously in Section 6.3.3, it is not possible to compare the electron x position due to uncertainty in the background subtraction.

6.3.4 Acceptance of electrons

Although not explicitly required for this analysis, the electron acceptance can now be determined for comparison with previous analysis. The acceptance of electron in the LUMI electron

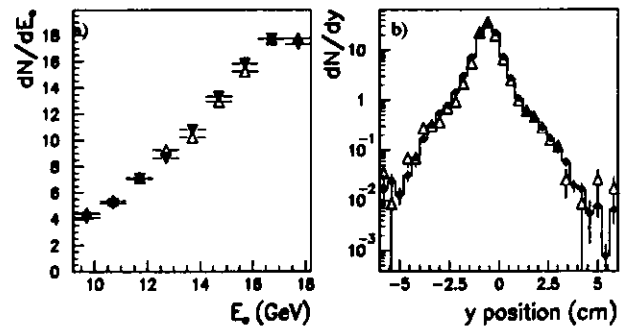

Figure 6-11 Spectra comparison in the LUMI electron calorimeter
The scattered electron energy spectrum a) and y position spectrum b) are compared between Monte Carlo, shown as the empty triangles and data, shown as the filled triangles and circles in a) and b) respectively. The y position of the Monte Carlo events is shifted by ≈2mm in b) to obtain agreement.

calorimeter, already shown in Figure 6-7 as a function of the interaction vertex position, is calculated using the HERACLES4.2 Monte Carlo as follows:

$$A_e = \frac{N_e^{meas}}{N_e^{gen}}, \qquad (6\text{-}7)$$

where N_e^{meas} is the number of events detected within a given measured energy range ($W_{\gamma p}$ bin) and N_e^{gen} is the number of events generated with HERACLES4.2 within a given scattered electron energy range. Figure 6-7 shows the strong dependence of the acceptance of certain bins in $W_{\gamma p}$ on the interaction vertex position. Figure 6-12 shows the acceptance of electrons as a function of y ($\approx 1 - E_e/E_{beam}$) and Q^2, as well as the generated spectrum for a horizontal vertex position of 0.087 cm. The minimum value of Q^2, Q^2_{min}, as a function of y is clearly evident on the left side of the generated spectrum (see Section 2.2). The measured electron energy bins are labelled on the acceptance plot, as well as the $Q^2 = 0.02\ \mathrm{GeV}^2$ line. The acceptance drops rapidly with increasing Q^2, as larger Q^2 events have a greater scattering angle and the electron does not reach the detector. There is no acceptance for events above $Q^2 = 0.02\ \mathrm{GeV}^2$ in the region of interest.

The final electron acceptance at the determined horizontal vertex position is shown in Table 6-1 for the three $W_{\gamma p}$ bins of interest, as well as an extra bin on each side, and for each cut

electron energy (GeV)	$W_{\gamma p}$ (GeV)	y	acceptance for $E_\gamma < 2$ GeV (%)	acceptance for $E_\gamma < 5$ GeV (%)	acceptance for no E_γ cut (%)
6.2 – 9.2	250	0.66 – 0.77	20.4 ±0.8 ±2.1	20.6 ±0.8 ±2.1	20.8 ±0.9 ±2.1
9.2 – 12.2	229	0.54 – 0.66	43.5 ±1.2 ±2.7	43.8 ±1.2 ±2.7	44.5 ±1.2 ±2.7
12.2 – 15.2	206	0.43 – 0.54	65.2 ±1.4 ±3.4	65.8 ±1.4 ±3.4	66.8 ±1.4 ±3.6
15.2 – 18.2	181	0.32 – 0.43	72.7 ±1.3 ±3.4	73.3 ±1.3 ±3.7	74.1 ±1.3 ±3.5
18.2 – 21.2	152	0.21 – 0.32	20.1 ±0.4 ±3.9	20.3 ±0.4 ±4.1	20.5 ±0.4 ±4.1

Table 6-1 Electron acceptance for $W_{\gamma p}$ bins

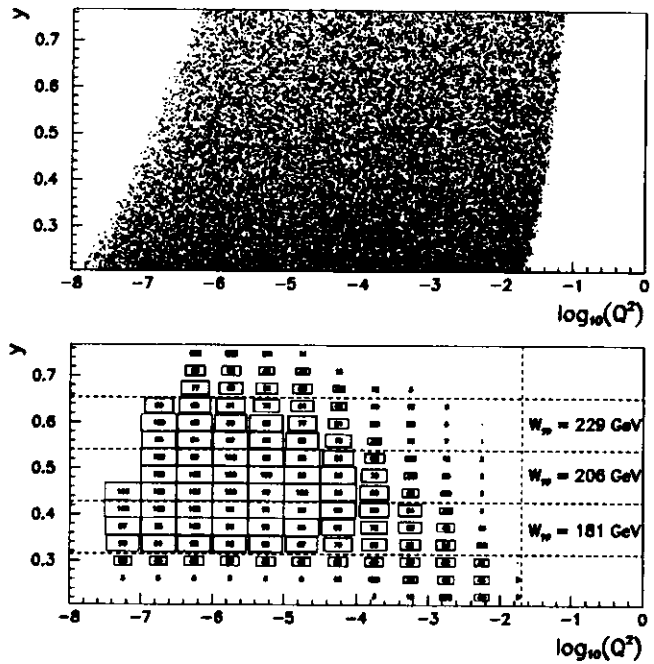

Figure 6-12 Scattered electron dependence on y and Q^2
The generated Monte Carlo distribution as a function of y and Q^2 is shown in the upper plot. The lower plot shows the acceptance (in %) of measuring the electron in the LUMI detector. The acceptance is divided into bins in y, which correspond to $W_{\gamma p}$ bins. Also shown is the $Q^2 = 0.02\ GeV^2$ line, showing that there is no acceptance for events above this Q^2 for the three bins of interest.

on the measured photon energy (see Section 4.5 and Section 6.4). The acceptance of the outer bins drops dramatically and does not allow a good measurement. Also shown is the relationship between the measured electron energy, the invariant mass ($W_{\gamma p}$) and y. The statistical error is the first error (upper) listed for each acceptance, and the systematic error is the second error (lower) listed. The systematic uncertainty is determined from a ±1.5% miscalibration of the electron energy as well as a ±0.023 cm shift of the horizontal vertex position. The systematic error clearly dominates over the statistical error for all bins.

As the acceptance is calculated from the measured energy in the electron detector, there is no compensation for any bin to bin migrations due to initial or final state radiation or from mis-measurement of the electron energy, although a cut on the photon energy does limit the radiative effects discussed in Section 2.5.3. These effects are present in both the Monte Carlo and the data sample and are discussed in more detail in the next section.

6.4 Radiative events

In addition to the Born level cross section, HERACLES4.2 generates higher order events (see Section 2.5.3) as well. For comparison to theory and to other experiments, the final quoted cross section should be at the Born level. Higher order terms involve the radiation of virtual and real photons. As explained in Section 2.5.3, these terms can affect the measured properties of the final electron and must be accounted for in the data. Previous studies [62][12] have shown that such corrections are small for the experimental conditions at ZEUS, nevertheless, systematic checks are made.

In order to look at the Born level cross section, in previous analyses a cut was made on the LUMI photon energy in data to reduce the effect of radiative corrections. Although a full higher order Monte Carlo is used in this analysis, and thus all terms should be properly simulated, different photon threshold cuts will be used for comparison with other studies. For each different threshold condition, the cross section will be determined. The reason for making a cut on the photon energy is twofold – to reduce the effect of higher order terms involving a real radiated photon and to obtain a sample clearly distinguishable from bremsstrahlung events. The photon thresholds, which were already encountered in Section 4, are set at 2 GeV and 5 GeV and with no threshold applied.

The radiative photon energy causes a shift in the scattered electron energy,

$$E_{e'} = E_e - E_{\gamma^*} - E_{\gamma'} \tag{6-6}$$

which no longer accurately tags the exchanged photon. The exchanged photon energy, calculated as $E_{\gamma^*} = E_e - E_{e'}$ is in reality lower by the energy of the radiated photon, hence the $W_{\gamma p}$ calculated for the event is higher than it should be. This allows low $W_{\gamma p}$ events to migrate upward into higher $W_{\gamma p}$ bins. By the same analogy, the energy of the scattered electron is decreased causing a migration from higher energy bins to the lower energy bins which, in effect, changes the measured energy spectrum. This migration should be accurately simulated in the HERACLES4.2 generator.

One other effect of a photon energy cut is the loss of physics events that are in coincidence with a bremsstrahlung photon. The acceptance for bremsstrahlung photons is very high, resulting in most of the coincidence events having an energy deposit in the photon calorimeter. A photon energy cut will cause the loss of some of these events which must be corrected for in the final cross section.

6.4.1 Bremsstrahlung overlay events

As already discussed in the previous section, bremsstrahlung overlay events, or *BSO* events, are caused by the coincidence of a physics event and the observation of a photon from a bremsstrahlung event. A cut on the LUMI photon energy results in the loss of these physics events from the data sample, and must be corrected for.

In order to correct for these lost events, the integrated probability of a bremsstrahlung event with a measured photon above a threshold energy occurring for any bunch crossing must be determined. This probability is determined by counting the number of bremsstrahlung events that deposit energy above the threshold value in the photon calorimeter and comparing this with the number of beam crossings,

$$P(E_\gamma^{th}) = \frac{R_{th}}{R_{all}}. \tag{6-7}$$

The rate above threshold is determined from the FLT counters (see Section 6.1.1) and the total crossing rate is calculated from HERA design parameters[1]. The value for R_{th} used is the luminosity weighted average value taken from all runs used in the analysis. The calculated probability, δ_{BSO}, is equivalent to the fraction of events cut due to BSO. The results for the three thresholds used are shown in Table 6-2.

	$E_\gamma < 2$ GeV	$E_\gamma < 5$ GeV	no E_γ cut
δ_{BSO}	1.36%	0.76%	0.0%

Table 6-2 Correction for bremsstrahlung overlays

The second category of events that are cut by the photon energy threshold is radiative events as discussed in the previous section. The combined losses from BSO events and radiative events are compared at different thresholds to determine an uncertainty for the BSO losses.

The fraction of radiative events that are removed from the event sample is estimated using the Monte Carlo. The measured photon energy spectrum from the HERACLES4.2 Monte Carlo is integrated to give the probability, δ_{rad}, of a measured radiated photon above the threshold value, as shown in Figure 6-13. From Figure 6-13, the δ_{rad} from an applied threshold of 2 GeV and 5 GeV are 1.25% and 0.45% respectively. The combined event loss from δ_{BSO} and from δ_{rad} should account for the change in the $N/\mathcal{L}$ of the data sample from Table 4-6 for different photon thresholds.

1. $R_{all} = N_{coll} \cdot f_{HERA}$ where N_{coll} is the number of colliding bunches and f_{HERA} is the rotational frequency of HERA (see Section 3.1).

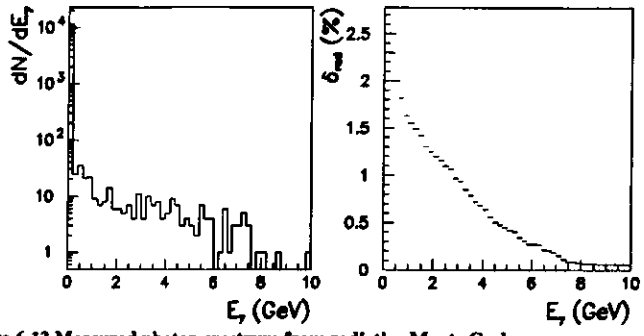

Figure 6-13 Measured photon spectrum from radiative Monte Carlo
The photon energy spectrum for the HERACLES4.2 events after regular data selection cuts and with a measured electron between 9.2 Gev and 18.2 Gev is shown on the left. The integrated fraction of lost events for a given photon energy threshold is shown on the right.

To compare the number of removed events by the photon energy cut in data and in the calculations above, a ratio between the data events at the different thresholds is compared to the ratio between the calculated losses at the different thresholds. Since the true total number of events is not known for the data sample, but the values obtained for δ_{BSO} and δ_{rad} are with respect to the true total number of events, a ratio is necessary to eliminate this from the comparison,

$$\frac{(1-(\delta_{BSO}(th1)+\delta_{rad}(th1)))N_{true}}{(1-(\delta_{BSO}(th2)+\delta_{rad}(th2)))N_{true}} = \frac{N/\mathcal{L}(th1)}{N/\mathcal{L}(th2)} = 1-R, \qquad (6\text{-}10)$$

where *th1* and *th2* are any two photon thresholds. The results of the comparison between the different thresholds is shown in Table 6-3. The dependence of the number of lost radiative events on the $W_{\gamma p}$ of the event is assumed to be small and is neglected. The average bin by bin variation is used to estimate an error for δ_{BSO}.

		$E_\gamma < 2$ GeV vs. $E_\gamma < 5$ GeV	$E_\gamma < 5$ GeV vs. no E_γ cut	$E_\gamma < 2$ GeV vs. no E_γ cut
R_{data}	$W_{\gamma p} = 181$ GeV	1.70%	0.22%	1.92%
	$W_{\gamma p} = 206$ GeV	1.79%	0.87%	2.66%
	$W_{\gamma p} = 229$ GeV	0.71%	1.22%	1.92%
$R_{(BSO,rad)}$		1.42%	1.21%	2.61%

Table 6-3 Event loss due to photon energy cuts

7 Total photoproduction cross section

All the pieces necessary to determine the total photoproduction cross section have been discussed in Chapter 4, 5 and 6. The measured electron-proton (*ep*) cross section, $\sigma_{ep}^{measured}$, can be calculated from the data and compared to the Monte Carlo. By an iterative procedure, the Monte Carlo is modified until it agrees with data. The total photon-proton (γp) cross section, $\sigma_{\gamma p}^{tot}$, is then given by the Monte Carlo as explained below.

7.1 $\sigma_{\gamma p}$ from the Monte Carlo

Although briefly described in Section 6.2, a further description of the HERACLES event generator is necessary. The effect of higher order corrections to the *ep* cross section is detailed in Section 2.5.3. The Born level *ep* cross section is calculated from a description of the γp interaction, $\sigma_T(y,Q^2)$ and $\sigma_L(y,Q^2)$, and a photon flux term which describes the electron-photon vertex. Different parameterizations of σ_T, σ_L are possible, resulting in the curves of Figure 7-1. HERACLES utilizes the input description of the γp vertex, and adds a full description of the electron-photon vertex, including higher order corrections such as vertex corrections, photon vacuum polarization, and emission of a real photon from the initial or scattered electron (see Figure 2-6). The resulting expression cannot be written in a neat analytical form like the Born term, and can only be evaluated numerically with a Monte Carlo such as HERACLES, but the expression remains dependent on only the two input functions, σ_T and σ_L [64]. With no analytically calculable form for σ_{ep} using higher orders, as exists for the Born term, the extraction of σ_T and σ_L must be done iteratively using the Monte Carlo. A value of σ_{ep} is calculated using HERACLES with an assumed dependence for σ_T and σ_L (i.e., the Abramowicz–Levin–Levy–Maor (ALLM) parameterization[21]). In effect, measuring the Monte Carlo *ep* cross section amounts to counting the events in a given kinematic region output by the Monte Carlo as will be discussed in the next section. A correction factor can then be deduced from the comparison of the measured Monte Carlo and data *ep* cross sections and applied to the input functions. σ_T and σ_L are then adjusted until the cross section from HERACLES agrees with the experimentally measured cross section.

7.1.1 Monte Carlo input

As discussed in the previous section, comparison between Monte Carlo and data is done at the level of the *ep* cross section. The $\sigma_{ep}^{measured}$ of the data is calculated using the results of the preceding chapters,

$$\sigma_{ep}^{measured} = \frac{N}{\mathcal{L}} \cdot \frac{(1+\delta_{BSO})\,\delta_{trig}}{A_{CAL}}. \tag{7-1}$$

This value is compared to the Monte Carlo,

$$R_\sigma = \frac{\sigma_{ep}^{HERACLES}}{\sigma_{ep}^{measured}}, \tag{7-2}$$

where $\sigma_{ep}^{HERACLES}$ is the calculated cross section obtained from the Monte Carlo. The value for $\sigma_{ep}^{HERACLES}$ is obtained from the ratio of events surviving all cuts vs. all generated events multiplied by the total *ep* cross section calculated and returned by HERACLES. The value of R_σ is the correction that is applied to the input into HERACLES to determine the final $\sigma_{\gamma p}^{tot}$.

Using the measurements of the total photoproduction cross section from ZEUS [65] and H1 [66] from the 1992 run, the obvious first choice for the input to HERACLES is the ALLM [21] parameterization. The results of the first comparison between HERACLES and the data using the ALLM parameterization are shown in Table 7-1. A rather large correction factor is obtained for

	$W_{\gamma p}$ = 181 GeV	$W_{\gamma p}$ = 206 GeV	$W_{\gamma p}$ = 229 GeV
σ_T input (μb)	140.35	141.97	143.31
$E_\gamma < 5$ GeV			
R_σ	0.794	0.735	0.723
(statistical error)	±0.020	±0.020	±0.025
(systematic error)	+0.062 −0.055	+0.062 −0.056	+0.083 −0.074
$E_\gamma < 2$ GeV			
R_σ	0.796	0.738	0.719
(statistical error)	±0.019	±0.019	±0.024
(systematic error)	+0.063 −0.056	+0.063 −0.057	+0.085 −0.076
no E_γ cut			
R_σ	0.802	0.739	0.729
(statistical error)	±0.019	±0.019	±0.024
(systematic error)	+0.063 −0.056	+0.062 −0.056	+0.081 −0.072

Table 7-1 Corrections to cross section using ALLM parameterization

each bin. These large corrections[1] imply that the true cross section is larger than predicted by ALLM. The correction factors can be used to obtain $\sigma_{\gamma p}^{tot}$ in a given bin by

$$\sigma_{\gamma p}^{tot} = \frac{\sigma_T\big|_{Q^2=0}}{R_\sigma}. \tag{7-3}$$

The systematic error for R_σ is obtained from the propagation of the errors from all components of the calculation, including a ±0.023 cm shift of the horizontal interaction vertex and a ±1.5% miscalibration of the LUMI electron calorimeter.

7.1.2 Reweighting Monte Carlo input to determine $\sigma_{\gamma p}$

The $\sigma_{\gamma p}^{tot}$ calculated from the corrections in Table 7-1 have an inherent error from using an input parameterization for σ_T at $Q^2 = 0$ to determine a much different final value for σ_T. A second iteration with an input parameterization close to the newly calculated value should be made to reduce such effects. For this, a different γp parameterization can be used with values close to those from Table 7-1, or the ALLM parameterization can be linearly scaled in $W_{\gamma p}^2$,

$$f(W^2) = a + bW^2, \tag{7-4}$$

where $f(W^2)$ is the correction applied to the input σ_T. The scale factor is designed to give the same results for the low energy data ($f(W^2)=1$ at W=15 GeV), but have an increased value for σ_T in the region of interest ($f(W^2)=z$ at W=206 GeV), such that $z\sigma_T$ gives the cross section from the previous iteration.

Since each of the bins has a different correction, as a first attempt, the reweighting factor will be the average of the $W_{\gamma p}$ = 206 GeV bin, which is R_σ = 0.74. This correction results in a scale factor, $f(W^2)=0.74^{-1}$ at W=206 GeV. Since $f(W^2)$ is linear in W^2 each bin has a different resulting scale factor, $f(W^2)=0.80^{-1}$ at W=181 GeV, and $f(W^2)=0.68^{-1}$ at W=229 GeV, very similar to the results for R_σ from Table 7-1.

The results of the second iteration are shown in Table 7-2. The correction for all bins is small. The systematic error is again determined from the propagation of all component errors. A similar measurement of the cross section in [11] uses only a single iteration. The error associated with using only one iteration is estimated by comparing the cross section obtained from the results of Table 7-2 and Table 7-1. The single iteration error is of the order 3% for the lower $W_{\gamma p}$ bin, 1% for the middle bin, and 0.5% for the upper bin. In each case, the single iteration cross section is lower than the final cross section (see Table 7-4).

1. Large corrections here implies values differing from 1. Values less than 1 indicate that the γp cross section of data is larger than the input to HERACLES.

	$W_{\gamma p}$ = 181 GeV	$W_{\gamma p}$ = 206 GeV	$W_{\gamma p}$ = 229 GeV
σ_T input (μb)	178.74	192.34	206.21
$E_\gamma < 5$ GeV			
R_σ	0.984	0.983	1.037
(statistical error)	±0.023	±0.024	±0.031
(systematic error)	+0.076 −0.067	+0.085 −0.077	+0.102 −0.086
$E_\gamma < 2$ GeV			
R_σ	0.987	0.987	1.031
(statistical error)	±0.023	±0.024	±0.031
(systematic error)	+0.077 −0.068	+0.085 −0.077	+0.105 −0.090
no E_γ cut			
R_σ	0.992	0.989	1.039
(statistical error)	±0.022	±0.023	±0.030
(systematic error)	+0.077 −0.068	+0.085 −0.077	+0.099 −0.082

Table 7-2 Corrections to cross section using ALLM reweighted by 0.74

Since only ALLM has been used, the conclusions from Table 7-2 implicitly contain the y,Q^2 dependence assumed by ALLM. For comparison purposes, another sample of Monte Carlo should be generated using, for example the Donnachie–Landshoff (DL) [63] parameterization to determine model dependent systematics. The DL sample is generated with R_σ = 0.84 which gives a cross section of ~192 μb at $W_{\gamma p}$ = 206 GeV. This approximately corresponds to the cross section determined for the ALLM parameterization reweighted by 0.74 in this bin from Table 7-2. A VMD-like dependence for σ_T and σ_L as a function of Q^2 is assumed when generating the sample (see Section 2.3.1). The results for this sample are given in Table 7-3.

7.2 Final values for $\sigma_{\gamma p}$

The final cross section, given in Table 7-4, is taken from the average of the different photon energy cuts in each bin from Table 7-2 using Eqn. (7-3). The range of values from the photon cuts is shown in Table 7-5 along with the change in the cross section from using the DL parameterization. In both cases, the systematic error is much smaller than the total systematic error from Table 7-4, and fall within the statistical error, again from Table 7-4. These effects are ignored in the final error.

The final cross section is shown graphically in Figure 7-1, along with the corrected ZEUS 1992 measurement and the H1 1994 measurement [67]. The new measured value for the $W_{\gamma p}$ = 181 GeV center of mass energy bin is larger than the published value for the 1992 cross sec-

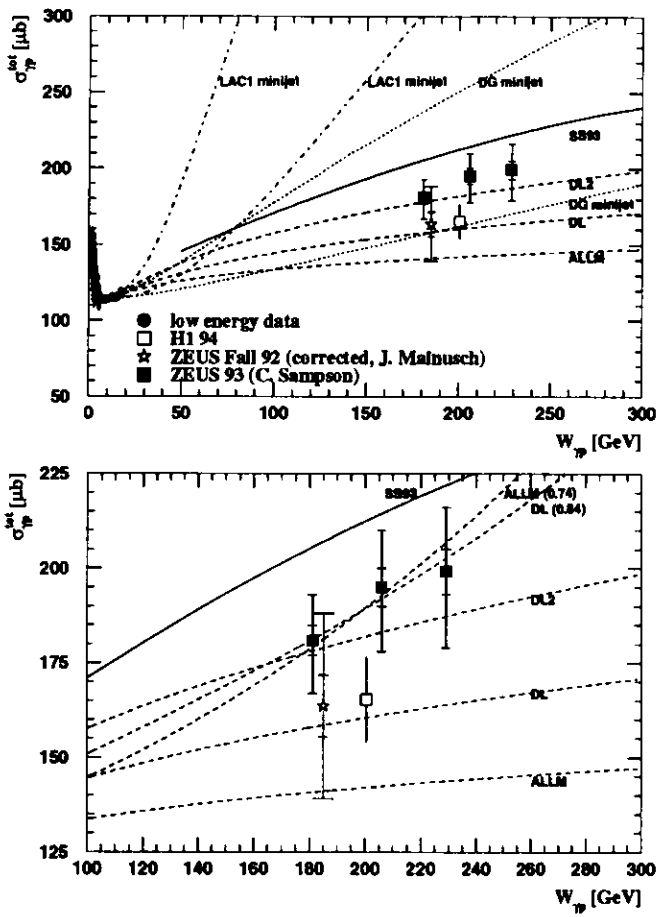

Figure 7-1 Total photon-proton cross section as a function of center of mass energy
The upper figure shows the calculated total γp cross section using the 1993 data with systematic errors added linearly to statistical errors, as well as the 1992 corrected measurement displaced in $W_{\gamma p}$ to allow easy viewing and the H1 1994 measurement. Also shown are various theoretical parameterizations for the cross section. The lower figure shows a zoom of the region of interest, along with the reweighted parameterization curves used to obtain the cross section (see text for discussion).

	$W_{\gamma p}$ = 181 GeV	$W_{\gamma p}$ = 206 GeV	$W_{\gamma p}$ = 229 GeV
σ_T input (μb)	181.59	192.40	203.11
$E_\gamma < 5$ GeV			
R_σ	1.010	0.980	1.034
(statistical error)	±0.024	±0.024	±0.031
(systematic error)	+0.082 −0.073	+0.084 −0.077	+0.117 −0.103
$E_\gamma < 2$ GeV			
R_σ	1.012	0.983	1.027
(statistical error)	±0.023	±0.024	±0.031
(systematic error)	+0.083 −0.074	+0.085 −0.077	+0.120 −0.107
no E_γ cut			
R_σ	1.019	0.986	1.040
(statistical error)	±0.022	±0.023	±0.030
(systematic error)	+0.082 −0.074	+0.085 −0.077	+0.114 −0.101

Table 7-3 Corrections to cross section using DL reweighted by 0.84

	$W_{\gamma p}$ = 181 GeV	$W_{\gamma p}$ = 206 GeV	$W_{\gamma p}$ = 229 GeV
$\sigma^{tot}_{\gamma p}$ (μb)	181	195	199
(statistical error)	±4	±5	±6
(systematic error)	+12 −14	+15 −17	+17 −20

Table 7-4 Final γp cross section

	$W_{\gamma p}$ = 181 GeV	$W_{\gamma p}$ = 206 GeV	$W_{\gamma p}$ = 229 GeV
higher order corrections (μb)	±0.79	±0.66	±0.90
model dependence (μb)	±1.83	±0.72	±2.61

Table 7-5 Corrections to γp cross section

tion of 143 ± 4(stat.) ± 17(syst.) μb [65] for this bin. A correction to the published value was made in [11] by correcting a 4% miscalibration of the LUMI electron detector resulting in a new 1992 cross section of 164 ± 5(stat.) ± 22(syst.) μb which is shown in Figure 7-1.

Also shown in the illustrations are various parameterizations, discussed in Section 2.4, as well as the reweighted ALLM (labelled ALLM(0.74)) and DL (labelled DL(0.84)) curves used to obtain the final cross section. The prediction with the inclusion of the new CDF measurements (see Section 2.4.1) is labelled DL2. The Schuler and Sjöstrand parameterization (SS93) shown assumes p_0 = 0.5 GeV and $p_{\perp min}$ = 1.3 GeV for the two p_t cutoffs (see Section 2.4.3). Four minijet parameterizations are shown (see Section 2.4.2). All four predictions use the KMRS [68] parameterization for the proton structure function. The dotted curves use the Drees–Grassie (DG) [69] parton distribution for the photon with a p_T^{min} of 2.0 GeV and 1.4 GeV for the lower and higher predictions respectively. The dashed-dotted curves are based on the Levy–Abramowicz–Charchula set I (LAC1) [70] parton distribution for the photon, again with p_T^{min} of 2.0 GeV and 1.4 GeV for the lower and higher predictions respectively.

7.3 Physics conclusions

This thesis presents one of the classic measurements in particle physics, the interaction strength between two of the constituents that dominate the known universe, at a previously unexplored energy. Unlike the previous 1992 published [65] measurement of the γp cross section at 181 GeV center of mass energy, this analysis includes full radiative effects at the electron-photon vertex as well as a full description of the virtual photon using both the σ_T and σ_L components. The resulting photon-proton total cross section for each of the three energy bins analyzed is given in Table 7-4.

The Regge theory parameterizations are based on hadron-hadron interactions. The dependence of the cross section on the center of mass energy is given by two separate terms, one attributed to reggeon exchange and the other to pomeron exchange (see Section 2.4.1). The fitted exponentials, $\varepsilon = \alpha_{\mathcal{P}} - 1$ and $\eta = \alpha_{\mathcal{R}} - 1$ are universal (i.e., they are the same for all processes) and are determined from fits to low energy data. The older Regge theory parameterizations, ALLM which is based on γp data and DL which is based on pp and $\bar{p}p$ data, fall below the measured data points. These older parameterizations suffered from a small lever arm from the low energy data with which to make predictions for higher energy interactions. The newer DL2 parameterization, based on the DL parameterization with the inclusion of the new CDF cross section measurements, is consistent with the cross section points measured in this analysis and thus also consistent with the CDF cross section measurements. This suggests that the photon interacts almost exclusively through its hadronic component at high center of mass energies; however, a contribution to the cross section from direct and resolved processes does exist and has been observed at ZEUS [16].

The Schuler and Sjöstrand parameterization employs a mixture of a VMD-like photon (see Section 2.3.1), and a partonic photon which can couple directly to a parton from the proton as well as coupling to a quark-antiquark pair which can subsequently interact with a parton from the proton

(see Section 2.3.2). The behavior of the cross section is governed by two p_t cutoff scales, p_0 the relative p_t between the $q\bar{q}$ pair and $p_{\perp min}$ the minimum event p_t in which perturbative calculations become applicable. In Figure 7-1, the Schuler and Sjöstrand prediction lies above the data points. This suggests that the perturbative cutoff used, $p_{\perp min}$ = 1.3 GeV is too low, and perturbative calculations only become valid at a higher event p_t.

The minijet parameterizations shown in Figure 7-1 are based upon an assumed structure function for the photon and the proton. Two photon structure functions are shown, calculated using two different p_t cutoffs at which perturbative calculations become applicable. The Levy–Abramowicz–Charchula set I (LAC1) structure function differs from the Drees–Grassie (DG) structure function in the low x gluon content of the photon. LAC1 predicts a much steeper rise for the gluon content in the photon as x decreases than the DG structure function. The excess of glue in the low x region results in a much higher predicted cross section at high center of mass energies for the LAC1 structure function versus the DG structure function. In general, the minijet curves predict a cross section rising far more rapidly than the current measurement allows. Both LAC1 predictions result in a cross section far above the measured values at the center of mass energy examined implying that the photon does not possess the large gluon content predicted by LAC1 at low x values. The prediction using DG with p_T^{min} = 1.4 GeV (the upper curve in Figure 7-1) also gives a cross section that is above the measured points. Similar to the Schuler and Sjöstrand prediction above, this suggests that the p_t cutoff at which perturbative calculations become applicable is larger than the value of 1.4 GeV used. The second DG prediction (the lower DG curve in Figure 7-1) uses p_T^{min} = 2.0 GeV and falls below the measured cross section points. This implies a perturbative p_t cutoff that is lower than 2.0 GeV. Combining the two DG prediction yields a p_t range of 1.4 GeV – 2.0 GeV in which perturbative calculations become valid.

7.4 Summary

The various components needed to determine the final cross section were discussed in Chapter 4, Chapter 5 and Chapter 6. In Chapter 4, the various run cuts were described as well as the effect of these cuts on the measured number of events per unit luminosity, $N/\mathcal{L}$. Early runs were removed from the data sample due to a shift of the interaction vertex position. Low luminosity runs were also rejected due to the limited statistics available for correction of background processes and lower calibration statistics. A limited range of beam tilts was accepted so that the characteristics of the scattered electron could be reproduced. Tagged background events were identified and used to estimate the number of untagged background events present in the data sample. The final results of this Chapter are shown in Table 4-6.

In Chapter 5, the acceptance of the final hadronic system from the interaction in the ZEUS main calorimeter was discussed. The diffractive data was shown to be proportional to $M_X^{-2.6}$. Monte Carlo fits to the data using this M_X dependence resulted in a flat calorimeter acceptance over the three center of mass energy bins of A_{CAL} = 76.2% as shown in Table 5-16. Calorimeter acceptance was also divided into a diffractive (see Table 5-10) and non-diffractive (see Table 5-13) subsample for comparison to the 1992 values. These combined subsample acceptances result in a total acceptance which is slightly larger than the full sample acceptance (see Table 5-15), and is included in the systematic error. Running with a shifted vertex position would greatly help to reduce the systematic error from the uncertainty of the diffractive and elastic subprocess fractions. Further analysis is also needed to resolve the true M_X dependence of the data.

Most disturbing from Chapter 5 are the large corrections to the trigger efficiency observed for the 1993 analysis, shown in Table 5-17. The correction for the 1992 analysis amounted to ~2% for the $W_{\gamma p}$ = 181 GeV bin, whereas a 9% correction is applied in 1993. The large 1993 correction works directly into the R_σ factor used to determine $\sigma_{\gamma p}^{tot}$. The two competing effects in RCAL, the trigger turn-on rate (see Chapter 5.7) and the energy uncertainty in the RCAL (see Chapter 5.2.1), combine to make the determination of the trigger correction very difficult. An independent trigger is needed to better study the effect in the 1993 run and in future runs. Also, a much better understanding of the dead material in the RCAL section of the detector is needed for a better description in the Monte Carlo and a further understanding of the trigger corrections.

In Chapter 6, the luminosity measurement was discussed, as well as the calibration of the LUMI electron and photon calorimeters. Monte Carlo was generated with a modified description of the HERA beamline leading to the electron detector. Bremsstrahlung events were used to fix the location of the interaction vertex position, and HERACLES4.2 was used to determine the electron acceptance in the electron detector, which is shown graphically in Figure 6-7 as a function of the horizontal interaction position, and summarized in Table 6-1. The effect of an added photon energy cut to reduce the effect of higher order corrections was also examined and found to have a very small effect on the final cross section. A correction for good events lost from a photon energy cut must be applied to the data as shown in Table 6-2.

The final results for the photon–proton cross section are given in Chapter 7. The total cross section is found to be compatible with the latest Regge theory prediction, hence compatible with the recent CDF total cross section measurements. The measured cross section also rules out the large gluon content of the photon at low x predicted by the LAC1 structure function of the photon. The measured cross section is consistent with the DG photon structure function using a p_t cutoff at which perturbative calculations become valid between 1.4 GeV and 2.0 GeV. The SS93 prediction also suggests that the p_t cutoff for perturbative calculations is above 1.3 GeV.

A Example run summary

```
                          ZEUS  RUN  SUMMARY

                        Run Number :       7430

Run Type :   PHYSICS
Trigger Type :   STANDARD_19OCT93
Readout Component :   BAC FCAL BCAL RCAL VETO RMUO CTD FMUO VXD RHES LUMI LPs BEAM
Readout Component (total) :        3625703

                     Run Begin Time :   23-OCT-1993 07:33:49
                        End   Time :   23-OCT-1993 08:10:42

                     Mean Event Size :      23024  bytes

                     Event Sink :      50 100   0

            Event No (GFLT GSLT TLT) :  295576 101232  12345
            Event No (IBM VAX)       :   12345      0

         Curr of Magnet & Compensator :   3950.65 ,     704.72 amps
         Curr of Yoke   & Toroid      :   2999.30 ,     560.00 amps

           Mean Trigger Rate of GFLT :    156.95  Hz
                                GSLT :      -     Hz
                                TLT  :      -     Hz
           Mean Transfer Rate to IBM :      5.43  Hz
                                VAX  :      -     Hz

                   Reduction by GSLT :      66. %   ( (gflt-gslt)/gflt )
                   Reduction by  TLT :      88. %   ( (gslt-tlt)/gslt )


  Shift :    R.STROILI      GRACIANI       H.KIM          A.LEICH

  Reason of  END Run :  Normal END

  Comment :   [ ZMS005$SCH     ] ERROR 0D91807
```



```
Exp.No. 0                                                    Run.No.  7430

HERA :   Fill_no.   Energy(GeV)   I_At_Run_Begin(uA) At_End Max_In_Active

   P :      239       819.901            11100      11200      11300
   e-:      239        26.695            12600      12100      12600
  Time of last update : 1993-10-23-08:07:51


LUMINOSITY (Instantaneous) :  At_Run_Begin  At_End  Max_In_Active  Average
                                  0.70E+30   0.69E+30   0.71E+30   0.69E+30

     ACTIVE LUM (HERA INTEG.)0.11E+34  cm-2  (  1.2867 nb-1 )
     ON-TAPE LUM (ZEUS GATED)0.11E+34  cm-2  (  1.1161 nb-1 )
     MODE for LUM calculation   :  VME147 Based
     DEC based ON-TAPE LUM:  0.00E+00  cm-2  (  0.0000 nb-1 )


COMPONENT SPECIFIC :

    CALORIMETER  :  CLOSED COMPLETELY
    CTD_HV       :  ON
    VXD_HV       :  ON
    BAC_HV       :  ON
    LUMI_HV      :  ON

TLT Trigger Mode  :   11009
TLT Branch Online :    1 2 3 4 5 6

CAL Thresholds Type :   NO_RCAL_EMISS
          **************************************************
                    CALORIMETER FLT ENERGY SCALE
          **************************************************

          Total Energy     Transverse Energy     Missing Energy
        <------------>   <----------------->   <-------------->
Full Scale      50.0             75.0                 75.0        (GeV)

Sums Exclude:
bp Rings  Fcal: 3  Rcal: 1   Fcal: 1  Rcal: 0   Fcal: 0  Rcal: 7   trgtowers
Fcal Thr  EMC=  2  HAC=  2   EMC=  2  NAC=  2   EMC=  2  HAC=  2   ADC counts
Rcal Thr     =  2     =  2      =  2     =  2      =255     =255   ADC counts
Bcal Thr     =  2     =  2      =  2     =  2      =  2     =  2   ADC counts

==============================
GFLT Run Summary ---- Run 7430
==============================
          Run Type  :  PHYSICS
       Trigger Type :  STANDARD_19OCT93

           Status   :  Normally ended
       Start Time   :  23-OCT-1993  7:36:40
         End Time   :  23-OCT-1993  8:08:05
        Total Time  :       1884.86 [sec]  (incl. time not in ACTIVE state)
    Total Run Time  :       1881.21 [sec]  (time only in ACTIVE state)
  Total Active Time :       1632.21 [sec]

     Total Triggers :        295412          (without Init, Test)
Total Test Triggers :           165          (incl. End of Run Trigger)
   Last GFLT Number :        295576

Average Rates
Output trigger rate :        156.95 [Hz]
 Input trigger rate :        189.38 [Hz]

Deadtimes
     Total Deadtime :        252.65 [sec] ( 13.40 [%])
 Total Run Deadtime :        250.00 [sec] ( 13.28 [%])
    From Component  :         26.13 [sec] (  1.39 [%])
    From Ext. VETO  :          0.00 [sec] (  0.00 [%])
         From GFLT  :          0.00 [sec] (  0.00 [%])

Bunch Crossings
       e-p Bunches  :  84 bunches - 0-9 24-33 48-57 72-81 96-105 120-129
                                    144-153 168-177 192-195
    e-pilot Bunches :  10 bunches - 16-17 40-41 64-65 88-89 112-113
    p-pilot Bunches :   6 bunches - 196-201
  Triggered Bunches : 128 bunches - 0-10 15-18 23-34 39-42 47-58 63-66 71-82
                                    87-90 95-106 111-114 119-130 143-154
                                    167-178 191-202 219
```

```
==============================
GFLT Components/Test Triggers
==============================
Components
  name___readout_______status
  DOM    normal          OK
  BMTO   normal          OK
  FMUO   ignore errors   OK
  CTD    normal          OK
  VXD    ignore errors   OK
  CAL    normal          OK
  MES    normal          OK
  BAC    normal          OK
  VETO   normal          OK
  LOMI   ignore errors   OK
  LPS    normal          OK
  BEAM   normal          OK
  C5     normal          OK
  SRTD   no handshake    OK

Test Triggers
  type_name___________ECN___count____scheduling_taken__components
   254 ENV            210       1    1  0  1  0   115  All
   178 CAL_UNO        215       1   10  0  1  0    29  CAL,MES
   177 CAL_ENP        213       1    3  1  1  0     9  CAL
   179 CAL_QINJ       211       1    2  1  1  0    11  CAL

==========================================
GFLT Sub-trigger information ---- Run 7430
==========================================
From slot 0 to 31 id = vvvvssss, vvv:version, sss:slot, ttt:trigger type
id       sub-trigger                pre-scale   taken  rate+-error  |**0**1**2**3**4*
908000350 FMU*CALmx*aTRK*CVv(1250,46 1          5690  3.40+-0.04e+0|####
908001053 FMU_vs_agl                 128        40958  1.63+-0.00e+2|#########
908002054 FMU_s_agl                  128        14983  4.09+-0.01e+1|#######
908003055 FMU_l_agl                  128         4505  5.69+-0.02e+1|########
908004347 FMU_vs*CALmx*CVv(1250,464) 1         36756  2.38+-0.01e+1|#######
908005348 FMU_s*CALmx*CVv(1250,464)  1         13841  8.97+-0.07e+0|#####
908006449 FMU_l*CALmx*gTRK*CVv(1250, 1          3326  1.95+-0.03e+0|###
908007446 FMU_n*RMOI*VMor*IFRbpv     256        4211  5.16+-0.02e+1|########
908008002 RMU                        -         10348  4.33+-0.00e+2|##########
908009003 RMU                        -         31165  1.37+-0.00e+3|#############
908010434 CAL_E*RMU*vgTRK(464)       8           810  7.36+-0.20e-1|##
908011410 RCAL_E*RMUI*gTRK*CVv(464)  1         11510  7.44+-0.06e+0|#####
908012441 CAL_E*RMUI*gTRK*CVv(464)   1         19503  1.32+-0.01e+1|######
908013174 RMMU                       -         89643  7.76+-0.00e+3|################
908014294 CAL_E*RMU*aTRK(464)        1          8798  8.38+-0.07e+0|#####
908015364 RCAL_E*RMU*aTRK*CVv(464)   1         19819  1.25+-0.01e+1|######
908016901 RANDOM                  4096           309  1.17+-0.00e+3|############
908017368 FMC_CALIB_neutron          -          1304  2.24+-0.00e+2|##########
908018043 VETOWALL_OR                -         59968  9.01+-0.00e+2|################
908019065 C5                         -          4712  3.82+-0.00e+3|##############
908020454 FMCn*LEe(4999)             -           832  1.94+-0.03e+0|###
908021442 BPC_hit                    -         24532  3.79+-0.00e+2|##########
908022179 VETOWALL_IN                -         54720  6.96+-0.00e+3|################
908023202 C5VETO                     -           113  3.38+-0.00e+3|#############
908024282 TRK_any                    -        169066  1.16+-0.00e+4|##################
908025366 SRTDbit                    -          2977  1.70+-0.01e+1|######
908026225 TREverygood                -         28612  5.62+-0.01e+2|############
908027224 TREgood                    -        117500  1.94+-0.00e+3|#############
908028379 xREMCregi(464,464,464,464) -         71279  6.47+-0.01e+2|############
908029378 xFEMCregi(464,464,464,464) -         98285  1.34+-0.00e+3|#############
908030384 BCALregic*VWout(696,696, 256          3200  7.54+-0.02e+1|########
908031383 BCALregi*VWout(696,696,696 -          3856  3.14+-0.00e+2|##########

From slot 32 to 63
id       sub-trigger                pre-scale   taken  rate+-error  |**0**1**2**3**4*
908032444 BPC*CAL_E*CViv(464)        1         23238  1.51+-0.01e+1|######
908033019 LOMI_Eg(3490)           32768        11811  6.37+-0.00e+4|####################
908034212 LOMI_Eg*Ee(3490,4999)      -          7399  2.51+-0.00e+4|###################
908035020 LOMI_Ee(4999)              -         14526  3.79+-0.00e+4|####################
908036102 LEe*REMC_E(4999,464)       1          5722  3.66+-0.04e+0|####
908037455 FBCn*LEe*CViLgv(4999,3490) 1           823  5.99+-0.10e-1|##
908038103 LEe*REMCth(4999,1250)      1          4408  2.77+-0.04e+0|####
908039448 LEe*aTRK*CAL_E*CViLgv(4999 1          6188  2.56+-0.04e+0|####
908040201 EMC_E(10068)               1          7993  8.43+-0.07e+0|#####
908041207 BEMC_E(3404)               1         36661  3.58+-0.01e+1|#######
908042191 Et(11574)                  1         20198  1.59+-0.01e+1|#######
908043400 FBCAL_Emiss(12162)         -          8843  1.37+-0.01e+1|#######
908044200 CAL_E(14968)               1         14474  1.25+-0.01e+1|#######
908045198 REMC_E(2032)               1         18156  1.27+-0.01e+1|#######
908046308 xCAL_E(464)                -        264512  1.61+-0.00e+4|##################
908047438 FBCAL_Emiss*Et(10104,3930) 1         11127  1.01+-0.01e+1|#######
908048286 CAL_E*aTRK(10068)          -          7277  6.17+-0.06e+0|#####
908049277 xREMCth(3750)              -         71204  2.11+-0.00e+2|##########
908050263 REMCth(3750)               1         71198  4.53+-0.02e+1|########
908051263 REMCth(1250)             256        113723  2.39+-0.00e+2|###########
908052644 BPC*CAL_E*CViv(464)        -          23238  1.51+-0.01e+1|######
908053424 REMC_E*aTRK*CViv(464)      4          39032  3.67+-0.01e+1|#######
908054423 REMC_E*aTRK*FbpCViv(464,37 1          15376  9.49+-0.07e+0|#####
908055205 FCAL_E_bp(2500)            -         139491  3.67+-0.00e+3|###############
908056275 xBEMC_E(3404)              -          36661  4.07+-0.01e+1|#######
908057283 BEMC_E*aTRK(2032)          4          12089  1.38+-0.01e+1|#######
908058425 el_jpsi_ee3(2032,2500.660, 1           4899  3.46+-0.04e+0|####
908059295 EMC_E*aTRK(7520)           -          3958  3.75+-0.04e+0|####
908060453 LEe*gTRK*CViv(4999)        -          4938  9.46+-0.07e+0|#####
908061450 LEe*aTRK*CAL_E*CViv(4999,4 8          6199  6.41+-0.06e+0|#####
908062192 Iso_e                      -         66351  1.25+-0.00e+2|##########
908063361 Iso_mu_mult(2)             -        163837  9.12+-0.00e+3|################
```



```
==========================================
      GSLT EndofRun Summary
==========================================
Ending Run Number 7430 by NORMAL END!!!
Run Number: 7430   Run Type: PHYSICS  Trigger Type: STANDARD_190CT93
                Current State: END_IDLE          ONLINE
GSLT Event No: 101209   GFLT Event No: 295500  Total Events: 101210
Evts accepted (last 10 secs): 585  Trigger Rate (last 10 secs): 0.926758
                    LIST of Subtriggers:
Subtrigger    Events in Run      Trigger Rate       Description
  0         163     (0      )  0.425000 (0.425000)  Test Triggers

  1         1042    (0      )  0.525000 (0.525000)  downs

  2         100599 (0       )  0.926367 (0.926367)  Cal-CTD (Trk Cluste
  3         101047 (194291)    0.926563 (1.035449)  ector

  4         30093  (98020 )    0.818750 (0.943359)
  5         0      (0      )    0.000000 (0.000000)
 ---------------------------------------------------------
                    LIST of ACTIVE VETOs:
 Events Processed   Rejected   Percent Rejected    Description
   295412           191310          0.93           GeV

   295412           7540            0.64
   295412           21609           0.74
VETO Summary: Total Evts   295412 Rejected    210459 (  0.94 percent)
```

********** TLT Run Summary *************** Run Number = 7430

Run_Start_Time: Oct 23 08:43:43 Run_Stop_Time: Oct 23 09:15:30

Crates online	6	Run_Config	physics
cpu time (in ms)	23791880	TLT_Trig_Config	TRIGGERIMG
Run Status	618	Run Number	7430
No_Of_Waiting_Msgs	13776	No_Of_IO_Errors	32
Valid_Level_3_Event	101235	Invalid_Level_3_Event	0
No_of_Events_Accepted	12345	No_of_Events_Rejected	88890
No_of_Test_Triggers	49	No_of_Env_Records	115
No_of_TLT_Thru_Events	136	No_of_GSLT_Thru_Events	1042
No_of_Spark_Events	2247	BG_Events (Time,old)	593
No_of_VTX_Filter_Events	239	BG_Events (Time,Straub)	26016
No_of_Cosmic_Muons	7557	No_of_Halo_Muons	4076
Sampling_Filter_Events	516	No_of_SPP_Filter_Events	5835
No_of_DIS_Filter_Events	2174	No_of_BGF_Filter_Events	3240
No_of_EXO_Filter_Events	1494	No_of_MUO_Filter_Events	1319
No_of_Filter_Accepts	10908	No_of_Other_Events	49672
No_of_Events_to_IBM	12345	No_of_Events_to_VAX	6142

C5 TIMES (ns): Proton = 50.8 Electron = 30.3

SPP % VERTEX DISTRIBUTION (GAUSSIAN FIT)
Closest to z=0 : AVG = -4.5 SIGMA = 9.3 CHI2 = 4.604 Count = 2073
Highest Eplicity: AVG = -5.7 SIGMA = 10.2 CHI2 = 4.974 Count = 2063

Physics filters		Satisfies algorithm	Prescl fact	Events saved	Unique Events
Sampling filter		60809	120	516	417
SPP01: Nominal soft photo	1	2367	1	2367	915
SPP02: Untagged soft photo	1	15833	100	173	89
SPP03: Elastic rho	1	2575	1	2575	1677
SPP04: Beampipe Cal * RCAL	1	1096	1	1096	681
DIS01: Nominal DIS NC	1	1643	1	1643	523
DIS02: Hi-Q**2 DIS	1	60	1	60	24
DIS03: CC DIS	1	127	1	127	114
DIS04: DIS Beampipe Cal	1	378	1	378	0
BGF01: Hi Et	1	703	1	703	159
BGF02: Lumi tag	1	1085	1	1085	28
BGF03: Charm	1	2314	1	2314	463
BGF04: J/psi elastic	1	53	1	53	13
BGF05: J/psi inelastic	1	687	1	687	74
EXO01: NC	0	0	0	0	0
EXO02: CC	0	0	0	0	0
EXO03: Hi_Et	1	46	1	46	19
EXO04: NC_Mi_Et	1	865	1	865	24
EXO05: Lone Pair EMC	1	31	1	31	19
EXO06: Lone Pair VTX	1	65	1	65	17
EXO07: Jets	0	0	0	0	0
EXO08: Pmu VSA	1	43	1	43	0
EXO09: Pmu SA	1	16	1	16	0
EXO10: PMu LA	1	1	1	1	0
EXO11: BMu	1	37	1	37	22
EXO12: RMu	1	322	1	322	249
EXO13: CalMu	1	85	1	85	37
EXO15: Island Et	1	109	1	109	28
MUO1: Fmuon Low Mom	1	415	1	415	402
MUO1: Fmuon High Mom	1	638	1	638	578
MUO2: Fmuon Large Angle	1	192	1	192	189
GLOMU: BMUON Reconstructio	1	74	1	74	45
VTX01: Vertex filter	1	26977	120	239	169
SAP01: FMC Calorimeter	1	308	1	308	290
Logical OR: Physics filters				10019	
Logical OR: VTX/Sampling				738	
Logical OR of all filters				10908	

Unique_SPP_Events	3602	Unique_DIS_Events	681
Unique_BGF_Events	947	Unique_EXO_Events	441
Unique_MUO_Events	1235	Unique_VTX_Events	181
Unique_SAP_Events	291		

Beampipe Cal FLT after veto cuts:	1096
Beampipe Cal FLT with Ebp=0. :	28
Beampipe Cal with FLT=0, Ebp<>0 :	4
Beampipe Cal Status with FLT :	26

B Glossary

ALLM	Abramowicz-Levin-Levy-Maor, a Regge theory parameterization of the energy dependence of the total cross section.
BAC	The Backing Calorimeter, used to measure energy which escapes out the back of the high resolution calorimeter.
BCAL	The Barrel Calorimeter, one of the main units of the CAL.
BMUI/BMUO	The barrel muon detection system.
BREMGE	Event generator for bremsstrahlung events.
BREMLU	Bremsstrahlung event generator based upon BREMGE.
C5	A scintillation counter assembly positioned at the rear of RCAL near the C5 magnet.
CAL	The high resolution, compensating, depleted uranium-scintillator calorimeter.
CTD	Central Tracking Detector, a cylindrical drift chamber used to track charged particles from an interaction.
DESY	Deutsches Elektronen SYnchrotron, a large particle physics experimental facility located in Hamburg, Germany.
DG	Drees-Grassie, a parton distribution function parameterization for the photon.
DL	Donnachie-Landshoff, a Regge theory parameterization of the energy dependence of the total cross section.
DL2	A refit of the DL parameterization with the inclusion of the CDF cross section measurements.
EMC	Electromagnetic section of CAL for measuring electrons and photons from the interaction.
EPA	The Equivalent Photon Approximation, an approximation based upon the assumption that the photon mass and longitudinal polarization can be ignored.
FCAL	The Forward Calorimeter, one of the main units of the CAL.
FDET	The forward tracking system, consisting of the FTD and the TRD.
FLT	First Level Trigger, the first of a series of three triggers used to reduce the event rate coming from the detector.
FMUON	The forward muon detection system.

FTD	Forward Tracking Detector, used to track particles emerging from the CTD at low angles.
GRV	Glück-Reya-Vogt, a parton distribution function parameterization for the photon.
HAC	Hadronic section of CAL for measuring high energy hadrons from the interaction.
HERA	Hadron-Electron Ring Anlage, the world's first electron-proton colliding beam accelerator.
HERACLES	Events generator incorporating full radiative corrections at the electron vertex.
HERWIG	Event generator.
IP	The Interaction Point, where the electron beam and the proton beam collide.
KMRS	Kwiecinski-Martin-Roberts-Stirling, a parton distribution function parameterization for the proton.
LAC1	Levy-Abramowicz-Charchula, a parton distribution function parameterization for the photon.
LPS	The Leading Proton Spectrometer, a series of detectors for identifying low angle, high energy protons from the interaction.
LUMI	The luminosity monitor system consisting of an electron detector and a photon detector.
LUMIE	The electron detector of the LUMI system.
LUMIG	The photon detector of the LUMI system.
MOZART	Monte Carlo for ZEUS Analysis, Reconstruction and Trigger, the set of routines which simulates the passage of events through the different detector components.
MRSD-	Martin-Roberts-Stirling, a parton distribution function parameterization for the proton based upon next to leading order perturbative QCD calculations.
NikZak	Nikolaev-Zakharov event generator for photon diffractive events.
ONREMC	The online RCAL EMC trigger, which included all EMC trigger towers except those immediately surrounding the beam pipe.
ONREMCTH	The online RCAL EMC threshold trigger, which included all trigger towers including those immediately surrounding the beam pipe.
PYTHIA	Event generator.
QCD	Quantum Chromodynamics.
QED	Quantum Electrodynamics.
RCAL	Rear Calorimeter, one of the main units of the CAL.
RMUI/RMUO	The rear muon detection system.
RTD	Rear Tracking Detector, used to track particles emerging from the CTD at high angles.

SLT	Second Level Trigger, the second of three stages of trigger used to reduce the event rate coming from the detector.
SS93	Schuler-Sjöstrand, a parameterization for the energy dependence of the total cross section.
TLT	Third Level Trigger, the third and last stage of the online trigger used to reduce the event rate coming from the detector.
TRD	Transition Radiation Detector, a set of chambers located between the FTD chambers used to aid in electron identification.
TREMC	The recalibrated, offline RCAL EMC trigger, similar to the ONREMC trigger.
TREMCTH	The recalibrated, offline RCAL EMC threshold trigger, similar to the ONREMCTH trigger.
VCTRAK	One of two track reconstruction programs used by the ZEUS collaboration.
VMD	Vector Meson Dominance, the interaction of the photon through a fluctuation into a vector meson state.
VW	The Veto Wall, used to detect and veto proton background events occurring outside the detector.
VXD	Vertex Detector, a small drift chamber immediately surrounding the interaction point used to measure short lived particles produced in the interaction.

References

[1] F. Halzen, A. D. Martin, *Quarks & Leptons: An Introductory Course in Modern Particle Physics*, John Wiley & Sons Inc., Toronto (1984).

[2] K. Grotz, H. V. Klapdor, *The Weak Interaction in Nuclear, Particle and Astrophysics*, IOP Publishing Ltd., New York (1990).

[3] Review of Particle Properties, *Phys. Rev.* **D50** (1994) 1191.

[4] T. H. Bauer, R. D. Spital, D. R. Yennie, F. M. Pipkin, *Rev. Mod. Phys.* **50** (1978) 261.

[5] A. Levy, *J. Phys. G: Nucl. Part. Phys.* **19** (1993) 1489.

[6] G. A. Schuler, T. Sjöstrand, CERN-TH.6796/93 (1993);
G. A. Schuler, T. Sjöstrand, *Nucl. Phys.* **B407** (1993) 539.

[7] G. A. Schuler, T. Sjöstrand, *Phys. Lett.* **B300** (1993) 169.

[8] J. J. Sakurai, *Phys. Rev. Lett.* **22** (1969) 981.

[9] G. Levman, *Q^2 corrections to γp cross section measurements at HERA*, ZEUS Note 95-088 (1995).

[10] K. Goulianos, *Phys. Rep.* **101** (1983) 170.

[11] J. Mainusch, *Measurement of the Total Photon–Proton Cross–Section at HERA Energies*, Ph.D. Thesis, II. Institut für Experimentalphysik der Universität Hamburg (1995).

[12] B. Burow, *A Measurement of the Total Photon–Proton Cross Section in the Center of Mass Energy Range 167 to 194 GeV*, Ph.D. Thesis, University of Toronto, Toronto, Canada (1993) available as Internal Report DESY F35D-94-01 February 1994.

[13] T. J. Chapin et al., *Phys. Rev.* **D31** (1985) 17.

[14] CDF Collaboration, F. Abe et al., *Phys. Rev.* **D50** (1994) 5535;
CDF Collaboration, F. Abe et al., FERMILAB Pub-93/233-E/CDF.

[15] OMEGA Photon Collaboration, R. J. Apsimon et al., *Z. Phys.* **C43** (1989) 63;
OMEGA Photon Collaboration, R. J. Apsimon et al., *Z. Phys.* **C46** (1989) 35;
OMEGA Photon Collaboration, R. J. Apsimon et al., *Z. Phys.* **C53** (1989) 581.

[16] ZEUS Collaboration, M. Derrick et al., *Phys. Lett.* **B322** (1994) 287;
ZEUS Collaboration, M. Derrick et al., *Phys. Lett.* **B348** (1994) 665.

[17] H1 Collaboration, T. Ahmed et al., DESY 95-062 (1995).

[18] P. D. B. Collins, *An Introduction to Regge Theory and High Energy Physics*, Cambridge University Press, Cambridge (1977).

[19] A. Donnachie, P. V. Landshoff, *Phys. Lett.* **B296** (1992) 227.

[20] CDF Collaboration, F. Abe et al., *Phys. Rev.* **D50** (1994) 5550.

[21] H. Abramowicz, E. Levin, A. Levy, U. Maor, *Phys. Lett.* **B269** (1991) 465.

[22] G. A. Schuler, T. Sjöstrand, CERN-TH.7193/94 (1994).

[23] A. Kwiatkowski et al., *Comp. Phys. Commun.* **69** (1992) 155.

[24] H. Bethe, W. Heitler, *Proc. Roy. Soc.*, **A146** (1934) 83.

[25] V. B. Berestetskii, E. M. Lifshitz, L. P. Pitaevskii, *Quantum Electrodynamics*, Pergamon Press, 2nd ed., Oxford (1982).

[26] ZEUS Collaboration, *The ZEUS Detector, Status Report 1993*, ed. U. Holm, DESY, Hamburg (1993).

[27] R. Fernow, *Introduction to Experimental Particle Physics*, Cambridge University Press, New York (1986).

[28] ZEUS Calorimeter Group, A. Andersseen et al., *Nucl. Instr. and Meth.* **A309** (1991) 101;
ZEUS Barrel Calorimeter Group, M. Derrick et al., *Nucl. Instr. and Meth.* **A309** (1991) 77.

[29] K. Piotrzkowski, *Experimental Aspects of the Luminosity Measurement in the ZEUS Experiment*, Ph.D. Thesis, Institute of Nuclear Physics, Krakow, Poland (1993) available as Internal Report DESY F35D-93-06 October 1993.

[30] F. Chlebana, *First Measurement of the Proton Structure Function F_2 with the ZEUS Detector*, Ph.D. Thesis, University of Toronto, Toronto, Canada (1993) available as Internal Report DESY F35D-94-02 March 1994.

[31] F. Bénard, *Search for Leptoquarks in Electron–Proton Collisions*, Ph.D. Thesis, University of Toronto, Toronto, Canada (1995).

[32] S. M. Fisher, P. Palazzi, *The ADAMO Data System*, Programmer's manual Version 3.2, CERN, Geneva, 1992.

[33] H. Boterenbrood et al., *Nucl. Instrum. Meth.* **A332** (1993) 263.

[34] ACP Group, *Branch Bus Specification*, Fermilab (1987).

[35] ACP Group, *BVI Manual*, Fermilab (1987).

[36] ACP Group, *VBBC Manual*, Fermilab (1987).

[37] ACP Group, *Bus Switch Manual*, Fermilab (1988).

[38] D. Bailey et al., *A high speed DMA extender for the ZEUS third level trigger Silicon Graphics 4D/35S processors*, Proc. of the Int. Conf. on Comp. in High Energy Phys., Annecy (1992).

[39] ACP Group, *Cooperative Processes User's Manual*, Fermilab (1989).

[40] D. Bandyopadhyay, *MUTRIG: A Third Level Trigger Muon Finder*, ZEUS Note 93-013 (1993).

[41] G. F. Hartner et al., *VCTRAK (3.06/20): Offline Output Information*, ZEUS Note 96-013 (1996).

[42] W. Smith et al., *ZEUS Calorimeter First Level Trigger Operation*, ZEUS Note 92-103 (1992).

[43] W. Smith, K. Tokushuku, L. Wiggers, *First Level Trigger for 1993 Running*, ZEUS Note 93-010 (1993).

[44] ZEUS Data Acquisition Group, *ZEUS Contributions to the Real-Time 93 Conference, Vancouver, Canada*, DESY 93-091 (1993).

[45] K. Piotrzkowski, M. Zachara, *Determination of the ZEUS Luminosity in '93*, ZEUS Note 94-167 (1994).

[46] T. Sjöstrand, Z. *Phys.* **C42** (1989) 301;
H.-U. Bengtsson, T. Sjöstrand, *Comp. Phys. Commun.* **46** (1987) 43;
T. Sjöstrand, CERN-TH.7112/93.

[47] N. N. Nikolaev, B. G. Zakharov, *Z. Phys.* **C53** (1992) 331;
P. Bruni et al., *Proceedings of the Workshop "Physics at HERA"*, DESY (1992) 363;
A. Solano, *Studio di Processi Diffrattivi ad HERA*, Ph.D. Thesis, University of Torino (1993).

[48] B. R. Webber, *Ann. Rev. Nucl. Sciences* **36** (1986) 253;
G. Marchesini et al., *Comp. Phys. Commun.* **67** (1992) 465.

[49] UA5 Collaboration, G. J. Alner et al., *Nucl. Phys.* **B291** (1987) 445.

[50] A. D. Martin, W. J. Stirling, R. G. Roberts, *Phys Rev.* **D47** (1993) 867.

[51] M. Glück, E. Reya, A. Vogt, *Phys. Rev.* **D46** (1992) 1973.

[52] ZEUS Collaboration, M. Derrick et al., Z. *Phys.* **C63** (1994) 391.

[53] E-710 Collaboration, N. A. Amos et al., *Phys. Lett.* **B301** (1993) 313.

[54] M. Krzyzanowski, Institute of Experimental Physics, Warsaw University, Unpublished study.

[55] H1 Collaboration, S. Aid et al., DESY 95-162 (1995).

[56] K. Piotrzkowski, M. Zachara, *Determination of the ZEUS Luminosity in '93*, ZEUS note 94-167 (1994).

[57] J. Andruszkow et al., *Calibration Procedure of the Calorimeters of the ZEUS Luminosity Monitor*, ZEUS Note 94-071 (1994).

[58] Y. Iga et al., *Simulation of the ZEUS Calorimeter*, DESY 95-005 (1995).

[59] R. Brun et al., *GEANT: Simulation Program for Particle Physics Experiments*, CERN–DD/78/2 Rev. (1978).

[60] M. Przybycień, *BREMLU 1.0 – Generator for LUMI*, ZEUS Note 93-079.

[61] K. Piotrzkowski, L. Suszycki, *Proceedings of the Workshop "Physics at HERA"*, DESY (1992) 1463.

[62] K. Chatchula, J. Gajewski, *Numerical Study of Radiative Corrections in the Low Q^2 Region at HERA*, DESY 92-173 (1992).

[63] A. Donnachie, P. V. Landshoff, Z. *Phys.* **C61** (1994) 139.

[64] G. Levman, University of Toronto, private communication.

[65] ZEUS Collaboration, M. Derrick et al., Z. *Phys.* **C63** (1994) 391.

[66] H1 Collaboration, T. Ahmed et al., *Phys. Lett.* **B299** (1993) 469.

[67] H1 Collaboration, T. Ahmed et al., *Measurement of the Total Photon Proton Cross Section and its Decomposition at 200 GeV Center of Mass Energy*, Contribution to the International Europhysics Conference on High Energy Physics (HEP 95), Brussels 1995, to be published.

[68] J. Kwiecinski, A. D. Martin, W. J. Stirling, R. G. Roberts, *Phys. Rev.* **D42** (1990) 3645.

[69] M. Drees, K. Grassie, Z. *Phys.* **C28** (1985) 451.

[70] H. Abramowicz, K. Charchula, A. Levy, *Phys. Lett.* **B269** (1991) 458.